

# Simulating Turbulence Measurements in High Flow Ocean Regions with an Acoustic Backscatter Model

by

© *Emma Shouldice*

A thesis submitted to the  
School of Graduate Studies  
in partial fulfilment of the  
requirements for the degree of  
Master of *Science*, Physical Oceanography

Department of *Physics & Physical Oceanography*  
Memorial University of Newfoundland

*July 2019*

St. John's

Newfoundland

Page left intentionally blank.

# Abstract

Measurements of ocean turbulence are essential in understanding ocean mixing and bottom stress. These measurements of turbulence are also needed when establishing loading forces on marine structures especially where they are deployed in regions of high turbulence. In particular, there is a need for accurate measurements of turbulence in regions where in-stream tidal turbines are being deployed. This study reports on two broadband Doppler sonar systems, the 1 MHz Signature Nortek AD2CP and the Workhorse 600 kHz ADCP. The ability of these devices to collect accurate velocity measurements in tidal regions has been tested in the field (McMillan et al., 2016; Shcherbina et al., 2018); however we lack a way to directly validate the accuracy of these field measurements. This difficulty is addressed through the use of a three-dimensional numerical model of acoustic backscatter (Zedel, 2008, 2015). Developments to the model were completed for the present turbulence study, including the integration of data from a computational fluid dynamics simulation and an upgrade to the signal processing technique. The model can be used to simulate Doppler Sonar measurements in flows similar to those observed in regions where in-stream tidal turbines are deployed. The resulting model simulations show that turbulent structure can be resolved by both broadband Doppler systems, but that the 1 MHz Nortek AD2CP, which has a faster sampling rate, yields higher resolution results. This thesis discusses the uncertainty of the simulated results using quantitative tools and draws comparisons to an experimental study published by McMillan et al. (2016).

Page left intentionally blank.

## Acknowledgements

The biggest thanks goes to my supervisor Dr. Len Zedel for being supportive, approachable, and knowledgeable! I think all of your students would agree that you have a talent for lightening the stress of graduate school with humour. I couldn't imagine having a different advisor.

I'd also like to thank the members of the Zedel research team (Alex McTamney, Muriel Dunn, Kanachi Angadi and Stephen Snook) for filling our group meetings with home-made baked goods and laughter. From classes to conferences to field work, we've learned a great deal together and I hope that we continue to collaborate in the future. Thanks to my officemate Dr. Heather Andres for always having time to discuss research and for co-parenting an office jungle of plants. Thank you to Dr. Kelly Shorlin for being my mentor as I completed the Teaching Skills Enhancement Program (TSEP) and to the other departmental faculty members who have contributed to my success at Memorial University. I am very thankful to have worked with you all.

I would also like to thank my parents (Margo & Paul), siblings (Bradley & Mike) and sister-in-law (Pam) for their continued support, encouragement and love. Thank you for always being there, for listening to my science rants, and for keeping me motivated. An extra thanks to my younger brother Bradley for being my biggest inspiration. A special thanks to my inquisitive niece (Victoria) and energetic nephew (Owen), your requests for science demonstrations keep me on my toes. Thank you for everything you do, especially my loving parents – you rock.

Lastly, thanks to my best friends (Ryan Greene, Carmen Lee, Jocelyn Sinclair, Gillian Davies and Sarah Ellis) who are currently completing graduate programs or

other university degrees across the country. Thank you for always making the stress of graduate school a laughable and relatable experience. This thesis is in memory of my late Great Aunt Margo, Sister Marguerite Keenan, a woman who was as kind as she was passionate about learning. Thank you everyone for keeping me sane and for not judging the crazy amounts of ice cream I ate while writing this thesis!

# Contents

<b>Abstract</b>	<b>i</b>
<b>Acknowledgements</b>	<b>iii</b>
<b>List of Figures</b>	<b>ix</b>
<b>List of Tables</b>	<b>xiii</b>
<b>Nomenclature</b>	<b>xv</b>
<b>1 Introduction</b>	<b>1</b>
<b>2 A Fundamental Description of Ocean Turbulence</b>	<b>5</b>
2.1 Ocean Dynamics . . . . .	5
2.1.1 Energy Cascade . . . . .	10
2.2 Modelling Turbulence . . . . .	13
2.2.1 Synthetic Turbulence . . . . .	13
2.2.2 Direct Numerical Simulations . . . . .	15
<b>3 Principles of Sonar</b>	<b>17</b>
3.1 Basic Sonar Operation & Sound Propagation . . . . .	17
3.1.1 Signal Conditioning for a Generalized Sonar . . . . .	22

3.2	Classifications of Doppler Sonar . . . . .	23
<b>4</b>	<b>Measuring Ocean Turbulence</b>	<b>30</b>
4.1	Shear Probes . . . . .	31
4.2	Acoustic Doppler Velocimeters . . . . .	32
4.3	Doppler Sonar . . . . .	34
<b>5</b>	<b>Model of Acoustic Backscatter</b>	<b>38</b>
5.1	Introduction to Sonar Models . . . . .	38
5.2	Model of Acoustic Backscatter: Description . . . . .	40
<b>6</b>	<b>Model Developments</b>	<b>45</b>
6.1	Time Dilation & Doppler Shift . . . . .	45
6.1.1	Validating the Time Dilation Algorithm . . . . .	47
6.2	Signal Processing . . . . .	51
6.3	Integration of Turbulence Database . . . . .	55
6.3.1	Johns Hopkins Turbulence Database . . . . .	56
6.3.2	Scaling the Reference Turbulence . . . . .	57
6.3.3	Evolving Turbulence Domain with Time . . . . .	60
<b>7</b>	<b>Nortek AD2CP Simulations</b>	<b>64</b>
7.1	Device Configuration . . . . .	64
7.2	Simulation Results . . . . .	67
7.2.1	Spectral Analysis . . . . .	71
7.3	Investigating Data Quality . . . . .	75
7.3.1	Beam Width Significance . . . . .	75
7.3.2	Sample Rate Significance . . . . .	79

<b>8</b>	<b>Workhorse ADCP Simulation</b>	<b>82</b>
8.1	Device Configuration . . . . .	82
8.2	Simulation Results . . . . .	84
8.2.1	Spectral Analysis . . . . .	89
<b>9</b>	<b>Summary of Results</b>	<b>92</b>
9.1	Doppler Sonar Performance . . . . .	93
9.2	Current & Future Research . . . . .	97
	<b>Appendix</b>	<b>99</b>
A.1:	Turbulent Energy Spectrum . . . . .	99
	<b>Bibliography</b>	<b>101</b>

Page left intentionally blank.

# List of Figures

2.1	Schematic for the Kolmogorov energy spectrum highlighting the energy dissipation, inertial and the integral subrange. . . . .	11
3.1	Diagram of active sonar operation in its simplest conceptual form. . .	18
3.2	Basic sonar signal conditioning block diagram. . . . .	23
5.1	Acoustic backscatter model domain, colours represent the speed of the targets at a fixed time, warm (cool) colours represent fast (slow) movement (a). A beam pattern generated by the model, warm (cool) colours represent regions with high (low) scatter contributions (b). . . . .	42
6.1	Schematic of the acoustic model domain for the time dilation experiment, including a transducer (orange cylinder), target (green circle), 3 dB width (black dotted lines) and beam pattern (solid black line). . .	48
6.2	Histogram of normalized error ( $E_n$ ) for five thousand occurrences of the time dilation experiment (a) and a QQ-plot of the distribution (b). . . . .	50
6.3	A block diagram of analog demodulation circuit, showing the separation of an acoustic backscatter signal into an in-phase signal and a quadrature signal. . . . .	51
6.4	Diagram of sampling sinusoidal waves, showing that multiple functions can be fitted to the data. . . . .	53

6.5	Comparison of analog and digital signal processing techniques. The lower panel shows the difference between the results . . . . .	54
6.6	Two dimensional unscaled slice of U from the Reference Turbulence (a) and the turbulent energy spectrum (b). . . . .	57
6.7	Scaled Reference Turbulence (a) and time evolving velocities (b) at a fixed y and z position at an initial time. Figure (c) shows The difference between the velocity profiles $U(t_o)$ and $U(t_5)$ . . . . .	58
6.8	Locations of the acoustic targets (red dots) are updated with prescribed references turbulence (shades of blue / green). Particles (yellow dot) that move outside the model boundaries are wrapped back into the opposite side of the domain . . . . .	61
6.9	Schematic the mesh box placed in the model domain for the Eulerian fluid experiment (a). Experiment results including the tracked velocity compared the expected result, the Reference Turbulence (b). . . . .	62
7.1	A schematic of the Nortek AD2CP transducer locations (a) and the simulated transmit pulse (b) are presented. The simulated instrument was parameterized to match a broadband configuration in McMillan et al. (2016). . . . .	65
7.2	AD2CP simulated beam pattern. The warm (cool) colors represent the regions of high (low) scattering. The x's show the midpoints and the black dots show the 3 dB beam width. . . . .	67
7.3	The simulated acoustic backscatter amplitude of the AD2CP is shown in (a) warm (cool) colors represent regions with high (low) backscatter contributions. The simulated Doppler phase shift is shown in (b). . . . .	68

7.4	The Reference Turbulence (a) and the simulated AD2CP turbulence measurement (b) compared with the difference between true and measured velocity (c). The occurrence where the finer turbulence structures are unresolved by the simulation are highlighted in (c) by shades of dark green and bright yellow. . . . .	70
7.5	Correlation from the simulate AD2CP data . . . . .	71
7.6	Turbulent energy spectrum for the Nortek AD2CP simulations, the turbulent spectrum for each range bin of measured velocity is shown by the light blue stars. . . . .	72
7.7	Significance of nominal beam width on AD2CP performance. Asterisks represent the energy spectrum for each range bin while solid lines represent the spectrum over range of 6 m. . . . .	76
7.8	Measured velocity for AD2CP simulations for various beam patterns, (a) wide, (b) base and (c) narrow beam . . . . .	77
7.9	Difference between the measured velocity from AD2CP simulations and the Reference Turbulence for various beam patterns, (a) wide, (b) base and (c) narrow beam . . . . .	78
7.10	The significance of the sample rate is considered by comparing four simulations with different sample rates. The grey dashed line is the $-5/3$ Kolmogorov slope. . . . .	80
8.1	Schematic of Workhorse ADCP transducer geometry (a) and the simulated transmit pulse (b). . . . .	83
8.2	ADCP Workhorse simulated beam pattern, warmer (cool) colors show the regions of high (low) scattered concentration. Black x's represent the location of the midpoints and the black dots represent the 3 dB beam width. . . . .	85

8.3	The simulated ADCP signal amplitude (a) and the measured Doppler phase shift (b). . . . .	86
8.4	Comparison between the Reference Turbulent velocity field (a) and the simulated ADCP vertical velocities observations (b). Figure (c) shows the anomalies between Reference Turbulence and measured velocity. .	87
8.5	ADCP Correlation over time is presented in (a), shades of pink (blue) represent strong (weak) correlation, (b) shows the correlation for each range averaged over time. . . . .	88
8.6	ADCP turbulent energy spectrum . . . . .	90
9.1	Time evolving turbulent velocity data (a) and the corresponding energy spectrum (b). . . . .	100

# List of Tables

4.1	McMillan et al. (2016) field experiment configuration . . . . .	36
7.1	Simulated AD2CP acoustic model configuration . . . . .	66
7.2	Table of spectral noise floors and Nyquist frequencies for sample rate simulations. . . . .	81
8.1	Simulated ADCP acoustic model configuration. . . . .	82

Page left intentionally blank.

# Nomenclature

## Abbreviations

The page numbers listed below indicate the place first reference within the thesis.

A/D	Analog to Digital Converter , .....	22
ADCP	Acoustic Doppler Current Profiler, .....	1
AD2CP	A type of ADCP developed by Nortek, .....	3
ADV	Acoustic Doppler Velocimeter, .....	33
ADVP	Acoustic Doppler Velocity Profiler, .....	34
CFD	Computational Fluid Dynamics, .....	15
CTD	Conductivity, Temperature and Depth sensor, .....	31
dB	Decibels, .....	20
DNS	Direct Numerical Simulation, .....	3
EVR	Extended Velocity Range , .....	35
FFT	Fast Fourier Transforms , .....	48
JHTDB	Johns Hopkins Turbulence Database, .....	16
LES	Large Eddy Simulation, .....	14
LiDAR	Light Detection and Ranging, .....	30
LPF	Low Pass Filter, .....	51
MATS	Moored Autonomous Turbulent System , .....	32

MCPC	Multi-correlation Pulse Coherent , .....35
NS	Naiver-Stokes equation, ..... 6
RANS	Reynolds Averaged Naiver Stokes equation , .....8
SNR	Signal to Noise Ratio , ..... 22
TAMI	Tethered Autonomous Micro-structure Instrument, ..... 31
TKE	Turbulent Kinetic Energy Budget, .....34
VDCP	Virtual Doppler Current Profiler , .....40

## Symbols

The page numbers listed indicate the first place where these symbols are used.

*	Complex conjugate , .....27
$A$	Amplitude of expected backscatter signal , .....49
$a_i$	Acoustic backscattered amplitude for $i^{th}$ targets. , .....43
$C$	Assumed speed of sounds in the ocean, ..... 25
$C(t)$	Complex time series, ..... 22
$c$	Constant in Kolmogorov energy equation , .....12
$D$	Diameter of a transducer, ..... 75

$DT$	Acoustic transducer detection threshold ,.....	19
$E$	Turbulent energy ,.....	12
$E_n$	Normalized error , .....	49
$f_{bw}$	Bandwidth frequency of the sonar system , .....	66
$f_c$	Carrier frequency of the sonar system , .....	25
$f_{co}$	Coriolis force , .....	7
$f_d$	Expected Doppler shifted frequency , .....	49
$f_s$	Quadrature re-sampling frequency , .....	52
$f_T$	Frequency emitted by transducer , .....	47
$f_R$	Frequency received by transducer , .....	47
$F * G$	Cross correlation between two adjacent time series , .....	74
$F(t)$	A time series that is adjacent to $G(t + T)$ , .....	74
$g$	Earth's Gravity, .....	6
$G(t + \Delta t)$	A time series that is adjacent to $F(t)$ , .....	74
$I_k$	Segment modified periodograms, .....	99
$I_R$	Signal intensity at a distance R from the source .....	20
$I_{ref}$	Signal intensity of a plane wave, .....	19
$I_o$	Signal intensity at projector, .....	19
$I_1$	Signal intensity at 1 m from the source, .....	20
$I(t)$	In phase signal .....	22

$K$	Number of segments , ..... 99
$\mathcal{K}_d$	Sub-sampling parameter used in digital demodulation ..... 52
$L$	Length of segment , ..... 99
$\mathcal{L}$	Length scaled used to determine the Reynolds number , ..... 9
$M$	Number of elements in a finite series, ..... 27
$n$	Number of acoustic targets , ..... 43
$P$	Pressure level in the ocean, ..... 6
$\hat{P}$	spectral density estimate, ..... 99
$p$	Constant in the Kolmogorov energy spectrum , ..... 12
$q$	Constant in the Kolmogorov energy spectrum , ..... 12
$Q(t)$	Quadrature signal ..... 22
$\hat{R}(\tau)$	Backscatter autocorrelation (real and imaginary component), .. 27
$R(\tau)$	Backscatter autocorrelation (real component), ..... 27
$R(0)$	Backscatter correlation evaluated at zero, ..... 27
$R(o)$	Center of the acoustic source , ..... 21
$R(1)$	Distance R from the acoustic source ..... 21
$R^2$	Correlation coefficient , ..... 22
$R_e$	Reynolds Number , ..... 9
$RL$	Reverberation level of sound in the ocean , ..... 19
$R_{\max}$	Maximum range value ..... 26

$r_{ri}$	Distance between target and receiver , .....43
$r_{si}$	Distance between target and Source , .....43
$S(t)$	Acoustic backscatter calculated by the model , ..... 43
$S^2$	Noise floor in spectral space , .....73
$SL$	Source level of acoustic transducer , ..... 19
$t$	Time , ..... 47
$t'$	Dilated time , ..... 47
$TS$	Acoustic target strength , ..... 20
$TL$	Transmission loss in the signal , ..... 20
$TL(R)$	Transmission loss in the signal in terms of range , ..... 22
$\mathcal{U}$	Velocity Scale , .....9
$\bar{u}_i, \bar{u}_j, \bar{u}_k$	Mean velocity flow, ..... 8
$u_i, u_j, u_k$	Component velocity , .....6
$u'_i, u'_j, u'_k$	Turbulent velocity flow , ..... 8
$U_{max}$	Maximum velocity value , ..... 26
$U, V, W,$	Johns Hopkins Turbulence data velocity components , ..... 60
$V_{amb}$	Ambiguity velocity , .....25
$v_k$	Kolmogorov velocity scale , ..... 10
$V_r$	Radial velocity measured relative to a transducer , .....46
$X_{ith}, Y_{ith}, Z_{ith},$	Coordinate system of the location of acoustic targets , .....60

$z_n$	Series of backscatter returns , .....	27
$\theta_{3\text{dB}}$	3 dB nominal beam width , .....	75
$\epsilon$	Rate of Energy Dissipation , .....	10
$\delta$	Overall offset from zero , .....	49
$\Delta f$	Change in signal frequency , .....	47
$\delta x_i, \delta x_j, \delta x_k$	Acoustic target displacement , .....	61
$\rho$	Density , .....	6
$\rho(\tau)$	Magnitude of the backscatter autocorrelation , .....	27
$\lambda$	Wavelength for emitted pulse , .....	26
$\nu$	Kinematic Viscosity , .....	6
$\mu$	Dynamic Viscosity , .....	59
$\eta_k$	Kolmogorov length scale , .....	10
$\Omega$	Rational Rate of the Earth , .....	6
$\omega$	,Angular frequency .....	49
$\kappa$	Wave Number , .....	12
$\varphi$	Earth Latitude , .....	6
$\phi$	Phase shift , .....	25
$\phi_s$	Signal phase estimate , .....	49

$\sigma$	Frequency fitting parameter ,.....	49
$\sigma_v$	Velocity variance ,.....	27
$\tau_p$	time interval between emitted pulses ,.....	25
$\tau_k$	Kolmogorov Time Scale ,.....	10

Page left intentionally blank.

# Chapter 1

## Introduction

Global climate change is causing the world's temperature to increase. This global increase in temperature and the related increase in greenhouse gas concentration has motivated the discovery of new ways to reduce our ecological footprint. One way to decrease our ecological footprint and thereby reduce the atmospheric concentration of greenhouse gas is by generating renewable or sustainable energy instead of using conventional fossil fuels. An example of a viable and sustainable energy source is the use of tidal turbines. Oceans tides exhibit a periodic behaviour on a fixed time-scale and therefore, ocean tides are predictable (Knauss, 1987). This periodicity of ocean tides make the amount of energy produced by a tidal region a reliable source for renewable energy, as the tides will produce energy at a known location and a known time each day (Knauss, 1987; Charlier and Finkl, 2009). The energy captured for power generation at a given site depends on many factors including; the basin geometry and the tidal range (Charlier and Finkl, 2009). Some tools for estimating tidal energy include developing numerical models that are used to understand turbine influence on tidal flows (Karsten, 2011; McMillan et al., 2018), completing vessel-based surveys to map tidal sites (Palodichuk et al., 2013) and using satellite altimetry to estimate tidal energy dissipation (Egbert and Ray, 2003; Tahuchi et al., 2014).

Tidal turbines are currently being used as a source of renewable energy generation in several locations including, Shiwa Lake, South Korea (Cho et al., 2012); La Rance, France (Merlin et al., 1982) and Orkney, Scotland (Probert, 2011). In the Bay of Fundy, Canada efforts are ongoing to implement these systems. The continued development and success of implementing tidal energy in the Bay of Fundy depends on continued research (NS, 2012). The province of Nova Scotia highlights the following research topics as essential for the success of energy generation in the Bay of Fundy; (1) what is the full energy potential in the tidal channel, (2) what are the environmental impacts and (3) what is the market for in-stream tidal in Nova Scotia, Canada (NS, 2012).

As the renewable energy industry grows, research related to tidal turbines and site characterization has also continued to grow. For instance, research topics such as the potential power generation of given tidal sites (Karsten, 2011; Walters et al., 2013) and the effects of hydro-dynamical flows such as turbulence on turbines (Blackmore et al., 2016) have been investigated. It has been observed that turbulent flows can affect the longevity of tidal turbines, specifically, it has been found that an increase in the turbulent intensities results in a decrease in turbine thrust and performance (Blackmore et al., 2016). Turbulent loading and fatigue caused by dynamic ocean flows are one of the main causes of turbine rotor blade failure (Liu and Veitch, 2012). The recurrence of system failure has led to continued research that attempts to optimize the design of the turbine systems and thereby, reduce the frequency of system failures (Liu and Veitch, 2012).

Research into the accurate measurement of turbulent velocities in tidal regions

(Hay et al., 2015) is another initiative required by the tidal industry. Higher accuracy measurements of turbulence are beneficial for industry as they (1) improve the estimation of potential energy generated at a specific site and (2) allow for better estimates of the turbine fatigue as a result of loading (Hay et al., 2015). Understanding and accurately measuring turbulence in regions of high current speed is challenging. In-situ instruments used for measuring turbulence are difficult to position in regions of the ocean with large current speeds such as tidal channels. Acoustic Doppler Current Profilers (ADCPs) can be used to measure fluid flows in highly dynamics regions of the ocean using the principles of Doppler shifted frequency (Lorke and Wuest, 2005; Thomson et al., 2012; Kioroglou et al., 2013; McMillan and Hay, 2017; Shcherbina et al., 2018). ADCPs offer an attractive alternative as they can be deployed in tidal channels with more ease than in-situ instruments used to measure turbulence and they can collect unsupervised measurements of turbulence remotely.

Measurements of turbulence in tidal regions using ADCPs have been conducted in the field, (Thomson et al., 2012; McMillan and Hay, 2017; Shcherbina et al., 2018); however, we lack a way to directly validate the accuracy of these experimental field measurements. A numerical model of acoustic backscatter (Zedel, 2015) will be used to consider the uncertainties or limits of measuring turbulence with ADCPs in regions with high current speeds. The model of acoustic backscatter has been developed for simulations of velocity measurements, model modifications required for the present study include; the algorithm used to distort signals subject to Doppler shifts, an upgrade to the demodulation signal processing method and integration of data from a direct numerical simulation (DNS) of turbulence. The model has been used to simulate a Nortek 1 MHz AD2CP configuration and a Workhorse 600 kHz ADCP. The simulation results were used to consider the accuracies and limitations associated

with the application of ADCPs in high Reynold's number flows and the results are compared against an experimental application of the acoustic devices. The significance of beam pattern and sample rate on AD2CPs ability to resolve turbulence were also considered.

Background knowledge relevant to this thesis includes a fundamental understanding of ocean turbulence and Doppler sonar operation. A description of turbulent motion and methods of modelling turbulence are presented in Chapter 2. A detailed overview of the principals of sonar operation, the related sound propagation in the ocean and classification of Doppler sonar systems is given in Chapter 3. Building on these fundamental concepts, a summary of measuring turbulence in the ocean is presented in Chapter 4.

A theoretical and mathematical description of the model applied in this thesis is presented in Chapter 5 as well as a brief history of other sonar models developed sequentially. Developments to the model of acoustic backscatter including validations and modifications that will be discussed in Chapter 6 and Chapter 6.3. Simulations for the Nortek AD2CP 1 MHz system and the Workhorse 600 kHz ADCP system which operates with a sample rate approximately 4.5 smaller than the Nortek AD2CP has been completed, described in Chapter 7 and Chapter 8, respectively. The two simulations are compared to field results and the accuracy of the velocities measurements are discussed in Chapter 9.

# Chapter 2

## A Fundamental Description of Ocean Turbulence

Turbulent flows which are caused buoyancy force instabilities are often characterized by describing non-linearities, values of diffusivity, vorticity, or rates of energy dissipation (Kundu, 1990; Tennekes and Lumley, 1972; Thorpe, 2005). Common equations used to characterize or conceptualize oceanic dynamics, in particular, turbulence are described in Section 2.1 including the Reynolds decomposition, the energy cascade, and the rate of energy dissipation (Section 2.1). An overview of modelling turbulent motion is provided in Section 2.2.

### 2.1 Ocean Dynamics

Ocean circulation accounts for both large and small scale movements in the ocean. The circulation is influenced by external forces such as gravity as well as, the Coriolis effect and internal forces such as friction. The governing equation for these geophysical flows is the Navier-Stokes (NS) Equation, which is also known as

the momentum equation (Kundu, 1990). It accounts for external forcing and can be expressed for x, y, z components as:

$$x : \quad \frac{D u_i}{Dt} = -\frac{1}{\rho} \frac{\partial P}{\partial x} + 2\Omega u_j \sin\varphi + -\nu \nabla^2 u_i , \quad (2.1a)$$

$$y : \quad \frac{D u_j}{Dt} = -\frac{1}{\rho} \frac{\partial P}{\partial y} - 2\Omega u_i \sin\varphi + -\nu \nabla^2 u_j , \quad (2.1b)$$

$$z : \quad \frac{D u_k}{Dt} = -\frac{1}{\rho} \frac{\partial P}{\partial z} + \nu \nabla^2 u_k - g , \quad (2.1c)$$

where,  $\rho$  is the fluid density,  $P$  is the pressure,  $\Omega$  is the rotation rate of the Earth,  $\varphi$  is the latitude,  $g$  is the gravity,  $\nu$  is the viscosity and  $u_i$ ,  $u_j$ ,  $u_k$  are the directional velocity components. Dynamically, the terms of the horizontal NS equation (Equation 2.1a, 2.1b) from (the left to right hand side) represent, acceleration, pressure gradient, Coriolis forcing, and viscosity or frictional forces. For the vertical NS equation (Equation 2.1c) the terms represent acceleration, pressure gradient, frictional forces and gravity (from left to right). The acceleration term can be expanded, for instance for the x component;

$$\frac{D u_i}{Dt} = \frac{\partial u_i}{\partial t} + u_i \frac{\partial u_i}{\partial x} + u_j \frac{\partial u_i}{\partial y} + u_k \frac{\partial u_i}{\partial z} \quad (2.2)$$

and shows that it contains non-linear terms. The non-linear section of the acceleration term in Equation 2.1 represent the advection or transfer of momentum in the

fluid (Pope, 2000).

The NS equation as presented in Equation 2.1a - 2.1c are specific to oceanic flows, as they include a Coriolis forcing term ( $f_{co}$ ):

$$f_{co} = 2 \Omega \sin(\varphi) \quad \text{where,} \quad \Omega = 7.2 \times 10^{-5} \text{ rads/s} \quad (2.3)$$

which arises due to the influence of Earth's rotation on ocean circulation. The Coriolis effect is a pseudo-force that arises from motion in the rotating coordinate frame (Stewart, 2004), and causes the deflection of large scale moving objects, such as masses of water. In the northern (southern) hemisphere moving ocean water is deflected to the right (left) (Pedlosky, 1979).

Turbulent processes, such as mixing, are an important component in ocean stratification as it works against the tendency to separate into density defined layers. These turbulent mixing processes are also important for biological productivity in the ocean due to the effect of stratification on nutrient distribution in ocean layers. In this study, the simulated measurements of turbulence are based on forced isotropic turbulence data. The turbulent data doesn't account for ocean stratification. Due to the prevalence of turbulence in tidal channels that counter the oceans tendency to develop stratified layers.

Turbulence can be visualized as dynamic velocity fluctuations from the mean flow (Reynolds, 1895). The total velocity of a fluid flow can be represented as a mean velocity plus a turbulent velocity fluctuation, this representation of turbulence is known as the Reynolds decomposition (Reynolds, 1895) :

$$u_i = \overline{u_i} + u'_i \quad , \quad (2.4)$$

where  $u_i$  is the velocity,  $\overline{u_i}$  is the mean velocity, and  $u'_i$  is the turbulent component. The total velocity is a continuous function of  $x, y, z$  which implies that  $\overline{u_i}$  and  $u'_i$  must also be continuous functions of  $x, y, z, t$  (Reynolds, 1895). The Reynolds decomposition incorporates turbulence into the equations of steady fluid flows. The model used in this study applies Reynolds decomposition by using a turbulence dataset ( $u'_i$ ) and a fixed current speed ( $\overline{u_i}$ ) to inform the time evolving movement of acoustic targets (see Chapter 6.3).

By substituting the Reynolds decomposition (Equation 2.4) into NS (Equations 2.1a - 2.1c) and taking the time average, the Reynolds Averaged Navier Stokes (RANS) Equation is derived. RANS can separate the fluctuating turbulence and mean velocities contributors, making it a useful tool. The x-component of RANS is:

$$\frac{D u_i}{Dt} = -\frac{1}{\rho} \frac{\partial P}{\partial x} + 2\Omega u_j \sin\varphi + \nu \nabla^2 u_i + \langle u'_i u'_j \rangle \quad , \quad (2.5)$$

A comparison between the NS equation (Equation 2.1a), and RANS equation (Equation 2.5) for the x-direction highlights the difference between the two equations, which is the Reynolds stress,  $\langle u'_i u'_j \rangle$  (Pope, 2000). If the Reynolds stress term equals zero then NS would be equivalent to RANS. The Reynolds stress is a nine component symmetric tensor, where the diagonal components represent normal stress, and the off-diagonal terms are related to shear stress (Kundu, 1990). In this study, the turbulent dataset (Chapter 6.3) applied to advect acoustic targets in the model is a forced isotropic dataset. Isotropic turbulence was selected as it has uniform velocity

fluctuations in all directions. Water stratification is not important for this study as the regions of interests are mid-depth and well mixed tidal channels. In the case of isotropic turbulence, the off-diagonal shear stress terms in the Reynolds tensor will have no directional preference and will equal zero (Kundu, 1990).

Performing a scale analysis on the non-linear term and viscosity term of NS results in an expression known as the Reynolds Number (Tennekes and Lumley, 1972). The Reynolds number ( $R_e$ ) is the ratio between the inertial forces and the viscous forces in NS (Kundu, 1990; Tennekes and Lumley, 1972):

$$R_e = \frac{\mathcal{U}\mathcal{L}}{\nu} \quad , \quad (2.6)$$

where  $\mathcal{U}$  is the velocity scale,  $\mathcal{L}$  is the length scale and  $\nu$  is the kinematic viscosity. A large Reynolds number indicates that the non-linear terms dominates over the viscous term and a turbulent flow exists in the fluid system (Pope, 2000). A small Reynolds number indicates that the viscous term dominates over the non-linear terms and implies a laminar flow.

The Reynolds number is often used to determine the critical velocity at which a flow becomes turbulent and/or to quantify the region of transition between a laminar flow and turbulence. By definition, the point of transition between fluid flows is called the critical Reynolds number. Turbulent flows can be found in many oceanic processes but they are also easily created in a laboratory environment or observed in daily life. This transition occurs as the length scale ( $\mathcal{L}$ ) or the velocity scale ( $\mathcal{U}$ ) increase (decrease) causing a proportional increase (decrease) in the Reynolds number ( $R_e$ ) and correspondingly a flow transition

### 2.1.1 Energy Cascade

Large scale turbulent motions transfer energy to gradually smaller and smaller scales of motion by a three-dimensional process known as the energy cascade (Kolmogorov, 1941; Tennekes and Lumley, 1972; Jarrin, 2008). This cascade of energy from large scale motions to small scales motions is driven by the non-linear terms of NS equation (Equation 2.1) which are included in the acceleration term (Kundu, 1990). The transfer of energy between eddies is limited by viscosity (Tennekes and Lumley, 1972) at very small scales, and where the energy is then dissipated as heat. The region where viscous dissipation dominates (ie. energy is dissipated as heat) is referred to as the dissipation subrange and occurs at higher frequencies (Jarrin, 2008; Kolmogorov, 1941; Tennekes and Lumley, 1972). The Kolmogorov microscales are the parameters that govern the location in wave number space where the transition to viscous dissipation occurs (Tennekes and Lumley, 1972):

$$\eta_k = \left(\frac{\nu^3}{\epsilon}\right)^{1/4}, \quad \tau_k = \left(\frac{\nu}{\epsilon}\right)^{1/2}, \quad v_k = \left(\nu \epsilon\right)^{1/4}, \quad (2.7)$$

where  $\eta_k$ ,  $\tau_k$  and  $v_k$  are the Kolmogorov length, time and velocity microscales, respectively and  $\epsilon$  is the energy dissipation rate (Tennekes and Lumley, 1972). The energy dissipation rate is a characteristic used to describe properties of turbulent flows (Thorpe, 2005), specifically, it describes the amount of energy lost in the system due to the viscous forces that act on the fluid. The energy dissipation rate can also be used to describe and compare the turbulent characteristics of a measured velocity field. This thesis will use the rate of energy dissipation as a metric to compare simulation results to expectations and field measurements.

The Kolmogorov energy spectrum (Figure 2.1) highlights the regions of energy transfer via the energy cascade and the regions of energy dissipation into heat (Kundu, 1990). The Kolmogorov spectrum is divided into three wave number dependent sections, (1) the integral range, (2) the inertial subrange, and (3) the dissipation subrange, these wave number dependent sections are labelled on Figure 2.1. The integral range

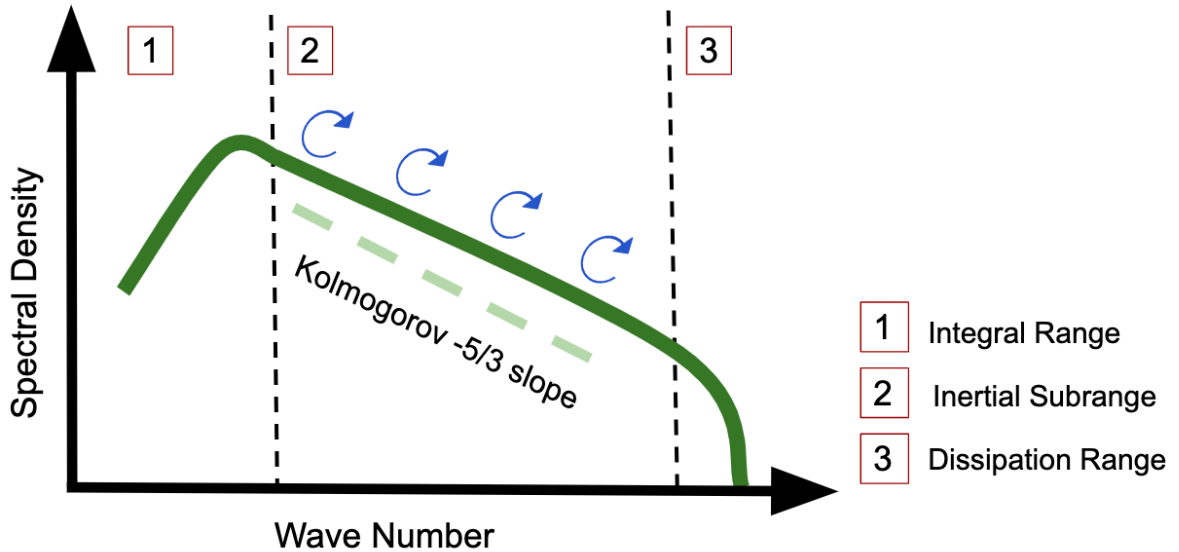


Figure 2.1: Schematic for the Kolmogorov energy spectrum highlighting the energy dissipation, inertial and the integral subrange.

is the region where eddies contain energy, specifically where energy goes into turbulence. The inertial subrange is where the transfer of energy from larger to smaller and smaller eddies occurs, known as the energy cascade. Within the inertial subrange energy is neither introduced nor removed from the turbulence. The quantity of total

energy in this region is constant, it is the distribution of energy across eddies that is shifting as the wave number increases. The rate of energy dissipation ( $\epsilon$ ) of the fluid influences the cascade of energy from large to smaller eddies (see Equation 2.8).

Within the finite frequency band that defines the inertial subrange the spectrum has the characteristic  $-5/3$  slope referred to as the  $\kappa^{-5/3}$  law (Kundu, 1990). This characteristic slope is expected to be observable from experimental observations of turbulence. The Kolmogorov energy spectrum is:

$$E = c \epsilon^q \kappa^{-p} , \tag{2.8}$$

where  $c$  is a constant defined by experiment,  $\kappa$  is the wave number,  $q = 2/3$  and  $p = 5/3$ . The  $\kappa^{-5/3}$  law is a convenient characteristic used when describing turbulence, and is used while discussing simulation results present in this study (Section 7.2.1 and 8.2.1). It is predicted that the acoustic simulations should be able to resolve turbulence in the inertial subrange, and observe the  $\kappa^{-5/3}$  law. At higher frequencies near the Kolmogorov microscales (Equation 2.7), energy is dissipated as heat in the energy dissipation range.

A useful tool when considering turbulent data in spectral space is Taylor's hypothesis also known as the frozen-turbulence approximation (Tennekes and Lumley, 1972; Kundu, 1990). Taylor's hypothesis assumes that the turbulent field is frozen in time allowing for time-dependent turbulent data ( $u(t)$ ) to be considered spatially as  $u(x/\bar{U})$  (Tennekes and Lumley, 1972; Kundu, 1990). This approximation can only be applied if the magnitude of the turbulent velocity is small when compared to the mean flow velocity (Tennekes and Lumley, 1972). Taylor's hypothesis will be applied

when analyzing the simulation results.

## 2.2 Modelling Turbulence

Accurate modelling of turbulence is a non-trivial task that has been approached by many researchers (Baran and Infield, 1995; Wilson, 1998; Huang et al., 2010; Kanov et al., 2015). These computational descriptions of turbulence vary in complexity and assumptions; some models describe the statistical properties of turbulent flows while others apply more mathematically involved approaches with fewer simplifying assumptions. Section 2.2.1 will describe an approach used to generate statistical characteristics of turbulence called synthetic turbulence, and will discuss its applications. Synthetic turbulence is relevant to this study as it is method applied in the original model of acoustic backscatter presented by Zedel (2008, 2015). Section 2.2.2 provides a description of higher order turbulence models, including the Direct Numerical Simulation (DNS) of turbulence utilized in this study.

### 2.2.1 Synthetic Turbulence

Synthetic turbulence is the concept that given some spectral characteristics of turbulence, a Fourier decomposition can be used to generate turbulent time series data (Tabor and Baba-Ahmadi, 2009; Castro et al., 2017). The generated time series data from this approach “looks” like turbulence, however, it is not fully characteristic of the spatial or temporal properties of turbulence. In other words, the method of synthetic turbulence provides a second order statistical representation of turbulence (Wilson, 1998; Tabor and Baba-Ahmadi, 2009) but, it does not capture the higher

order statistics observed or expected in real/observable turbulence (Wilson, 1998).

There are three spectra that are commonly used to generate synthetic turbulence: the isotropic Gaussian, the von Karman and the Kolmogorov model spectra (Wilson, 1998). One disadvantage to the isotropic Gaussian and the von Karman is that they are unrealistic in the inertial subrange. Turbulence that possesses the Kolmogorov energy spectrum is discussed in Section 2.1.1 and selected for its ability to represent the inertial subrange. The properties of this spectrum will be applied when analyzing the results of the acoustic model simulations. The original version of the acoustic backscatter model developed by Zedel (2008, 2015) used one-dimensional synthetic turbulence.

A common application of synthetic turbulence is in the field of Large Eddy Simulations (LES) (Tabor and Baba-Ahmadi, 2009; Huang et al., 2010), which are a computational method of modelling turbulent flows that only directly simulate the large scale motions of turbulence (Jarrin, 2008). The smaller scale motions are represented through a process called LES numerical scale separation (Jarrin, 2008). In the scale separation technique, a low pass filter operation is used to simplify NS, consequently, reducing the computational expense of the simulation. A requirement for accurate LES models is an initial inflow that exhibits turbulent fluctuations (Huang et al., 2010). The initial inflow into a LES must contain a statistical representation of turbulence and ideally, this initial condition is computationally inexpensive to generate (Tabor and Baba-Ahmadi, 2009). Synthetic turbulence meets both of these criteria and is a method of used generating LES initial conditions (Tabor and Baba-Ahmadi, 2009).

## 2.2.2 Direct Numerical Simulations

Direct Numerical Simulations (DNS) are computational fluid dynamic (CFD) models that describe fluid flow by solving the governing equations of fluid dynamics (Perlman et al., 2007). The NS equations (Equations 2.1a - 2.1c) are the primary governing mathematics of these simulations and are solved for all ranges and scales of turbulence with minimal simplifying assumptions (ex. no simplify assumptions about mixing are made). DNS are computationally more expensive than LES, as they make fewer assumptions about flow and directly simulate all the scales of turbulence (Jarriin, 2008), where LES makes assumptions to simply the computation and only model large scale motions. DNS can be used to simulate a range of fluid properties/flows including turbulent behaviour.

The spatial resolution of DNS depend on the physics of the situation being considered, parameters such as channel width and/or fluid depth will influence the model scales (Moin and Mahesh, 1998). Often the smallest scale of turbulence resolved by the model is on the order of magnitude of the Kolmogorov microscales (Equation 2.7) (Moin and Mahesh, 1998). A consequence of allowing a wide range of spatial scales while maintaining accurate simulation results is that model time steps are often small (Moin and Mahesh, 1998).

DNS are the most complete method used to compute turbulence as they are based on directly solving the NS equations, however, they are also the most computationally expensive approach (Verstappen and Veldman, 1997). To obtain high accuracy results, all CFD models employ small time steps, a large number of grid points and many model iterations which contribute to the computational expense of the simulation (Verstappen and Veldman, 1997). A difficulty with DNS is storing and organizing

the large volume of data that is generated (Wang et al., 2010). Cluster databases achieve a high level of parallelism which aides in the effectiveness of model performances however, bottlenecks can occur when parallel queries simultaneously submit (Wang et al., 2010). Improvements to cluster schedulers is a proposed solution to reduce the difficulty (Wang et al., 2010).

The Johns Hopkins Turbulence Database (JHTDB) is an open turbulence laboratory that runs DNS of turbulent fluid motion and archives the high-resolution results (Kanov et al., 2015). The multi-terabyte simulation results are made available via a publicly available web server (Kanov et al., 2015). The JHTDB laboratory stores results of several turbulent flow types including, (1) forced isotropic, (2) steady-state incompressible, and (3) variable-density mixing (Kanov et al., 2015). These simulations vary in grid resolution, run time and mathematical complexity.

For our purpose, the forced isotropic turbulence data-set is used as input into the model of acoustic backscatter. From this point onward, the abbreviation JHTDB will refer specifically to the forced isotropic data-set that is applied in this study. The full data-set has  $1024^3$  nodes with a domain of  $2\pi \times 2\pi \times 2\pi$  (Wan et al., 2018; Li et al., 2008). The database is designed to allow selection of as large or as small a domain as required (Kanov et al., 2015). The JHTDB has a dimensionless time step of  $\delta t = 0.0002$  and is archived after every ten time steps ( $\delta t = 0.002$ ) (Wan et al., 2018; Li et al., 2008). The prescribed turbulence has the characteristic  $-5/3$  slope that is associated with the inertial subrange of the Kolmogorov energy spectrum (Wan et al., 2018) and the dissipation subrange which is dominated by viscous forcing. A more complete discussion of the JHTDB will be presented in Chapter 6.3 along with a description of its application in this study.

# Chapter 3

## Principles of Sonar

The application of acoustic signals in measuring oceanic properties such as turbulence requires a strong understanding of how sound propagates in water and how the devices are used to collect observations. This chapter will provide an overview of sound propagation in the ocean and will discuss the operation of basic sonar (Section 3.1) including the active sonar equation. A description of Doppler sonar and the differences between incoherent, pulse-to-pulse coherent and broadband Doppler sonar will be highlighted in Section 3.2 along with a discussion of the advantages of each system.

### 3.1 Basic Sonar Operation & Sound Propagation

There are two kinds of sonar operation, active and passive. In passive sonar, transducers called hydrophones detect acoustic signals by converting pressure differentials that constitute sound into electric voltages. This approach has applications in marine animal research, fish ecology and military submarine detection. The second category, active sonar involves the transmission and reception of an acoustic signal. This type of sonar operation is a more widely used technique for measuring physical

properties of the ocean (e.g measuring velocity) and it is the technique utilized in this study.

The fundamental concept of active sonar (Figure 3.1) is that a transducer(s), called a projector(s) will convert electric signals into pressure differentials that propagate sound into the surrounding medium (Urick, 1967). A fraction of the emitted

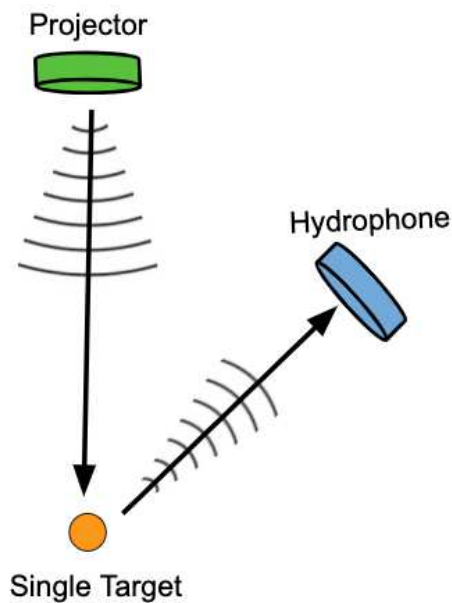


Figure 3.1: Diagram of active sonar operation in its simplest conceptual form.

sound is scattered back towards a hydrophone(s) by objects (or targets) in the medium and a portion of that sound is detected by receiving hydrophones (Urick, 1967; Zedel, 1985). Targets can be classified differently depending on the purpose of the given study, for instance; the bottom, marine organisms, ships, bubbles, or organic matter are all examples of potential acoustic scatterers.

A special case of active sonar systems rely purely on acoustic backscatter and for these systems the same transducer can be used to emit and receive signals (Urlick, 1967). The active sonar equation expresses the received sound level for point target backscatter in logarithmic space and is given as (Urlick, 1967):

$$SL - 2 TL + TS = RL + DT \quad , \quad (3.1)$$

where SL is the source level at the emitting transducer, TL is the transmission loss, TS is the target strength, RL is reverberation level, and DT is the detection threshold. All of the values in Equation 3.1 are expressed in decibels (dB).

The active sonar equation (Equation 3.1) is integrated into the model applied in this thesis by incorporating the laws of sound propagation when calculating the backscatter signal (see Chapter 5). The SL is the intensity of the acoustic signal emitted from the transducer with reference to the intensity of a plane wave at a distance of one meter from the source (Urlick, 1967), it is sometimes referred to as the projector source level and given as (Medwin and Clay, 1998):

$$SL = 10 \log_{10} \frac{I_o}{I_{\text{ref}}} \quad , \quad (3.2)$$

where  $I_o$  the sound intensity at the projector and  $I_{\text{ref}}$  is the intensity from a plane wave with a specified intensity of 1  $\mu\text{Pa}$ .

The TS is a value that describes the echo returns from targets as the ratio of reflected sound intensity to the intensity incident. TS is not the same as RL, which

is a summation of the total re-radiation of sound from the immediately surrounding water volume (Urick, 1967). The DT is the value that determines whether a signal return indicates that a target is present or absent (Urick, 1967). The value of the detection threshold will depend on the properties of the detector being employed. Lastly, TL is the decrease or weakening in signal strength over a given distance due to sound absorption, spreading and scattering (Jensen et al., 2011; Urick, 1967). TL in dB is given as (Urick, 1967):

$$\text{TL} = 10 \log_{10} \frac{I_1}{I_R} , \quad (3.3)$$

where  $I_1$  is the signal intensity at a reference distance of 1 m and  $I_R$  is the intensity at a distance  $R$  from the source. In the active sonar equation (Equation 3.1) the TL is multiplied by a factor of two, this factor accounts for the signal loss in both directions of travel. Passive sonar only has transmission loss in one direction as no sound is emitted by the device.

In the ocean, there are two main factors that influence the loss of signal strength, the geometrical processes of spreading and the absorption of sound energy by the medium. Spreading of acoustic signals is a factor that contributes to the weakening of signals as the distance from the source increases. Spreading depends on the surrounding environment available for propagation and therefore there are different categories including (1) no spreading (eg. sound in a tube), (2) cylindrical, (3) spherical and (4) hyper-spherical spreading (ie. higher dimensional geometry with a constant distance from the origin) (Urick, 1967). In relation to the simulation presented in Chapter 7 & 8, the sound sources experience spherical spreading. As an example of spherical spreading, imagine a sound source in an unbounded space when the sound

is emitted it travels outwards from the point of origin in a spherical geometry. In the sonar equation this spherical spreading loss is expressed as  $20 \log R$ .

$$\text{TL}(R) = 20 \log_{10} \frac{R_o}{R_1} , \quad (3.4)$$

where  $R_o$  is the acoustic center of the sound source and  $R$  is the range from  $R_o$ . Equation 3.4 assumes the source is omnidirectional, the environment unbounded and sound absorption in the medium is negligible. The sound intensity will decay at a rate of  $1/R^2$ .

Absorption of sound in the ocean is the process by which acoustic energy is lost and transferred into heat (Urlick, 1967). The farther the sounds travels the more acoustic energy will be lost due to absorption, similarly to the behaviour of geometrical spreading loss. This behaviour is due primarily to two causes in pure water (1) shear viscosity and (2) bulk viscosity (Liebermann, 1949; Leonard et al., 1949; Urlick, 1967; Medwin and Clay, 1998). Shear viscosity, sometimes called viscosity for short, is a ratio of the shear stress to the strain. The amount of energy lost in the sea is higher than that observed in pure water due to the chemical composition of the sea. Energy is lost to ionic relaxation referring to the chemical dissociation-reassociation process that happens to magnesium sulfate (  $\text{MgSO}_4$  ) and Boric Acid (  $\text{H}_3\text{BO}_3$  ) in the seawater as sound passes by (Leonard et al., 1949; Medwin and Clay, 1998).

Ambient noise in the ocean occurs naturally, some examples include marine mammal noise, wave action, seismic events, noise from wind and rainfall (Hodges, 2010). Anthropogenic causes such as shipping traffic can also contribute to ambient noise. Wenz (1962) published the typical sound levels of ocean background noise ranging

from low frequency seismic events (between 1 – 100 Hz) to biological background noise as high as 100 kHz. This noise categorization is commonly referred to as Wenz Curves and has application in identifying the types of ambient noise present in any given ocean environment. With so many sound sources, ambient noise is common and an important consideration for sonar operation (i.e. signal conditioning).

### 3.1.1 Signal Conditioning for a Generalized Sonar

The electrical signals corresponding to the received acoustic signal undergo signal conditioning to filter out noise and amplify the signal of interest. Figure 3.2 provides a generalized block diagram of the signal conditioning applied to sonar observations as used in the present study. The received analog signal passes through an amplifier, an anti-aliasing filter and is digitized by an A/D converter. The signal is demodulated retaining only bandwidth ( $f_o/2$ ) frequency, the signal creates complex outputs known as the in-phase,  $I(t)$ , and quadrature,  $Q(t)$ , signals, where  $C(t) = I(t) + jQ(t)$ . Section 6.2 will continue the discussion of demodulation, differentiating between analog and digital demodulation.

Correlation analysis is used to determine a rate of signal phase change ( $\Delta\phi$ ) which relates to velocity and a correlation magnitude ( $R^2$ ). The signal conditioning that happens before the correlation analysis (Figure 3.2, grey dashed box) is interchangeable between all types of sonar. Anti-aliasing removes frequencies that are in excess of the digitising frequency rate, as a consequence there is a reduction in noise and an improved the Signal to Noise Ratio (SNR). The component of signal conditioning

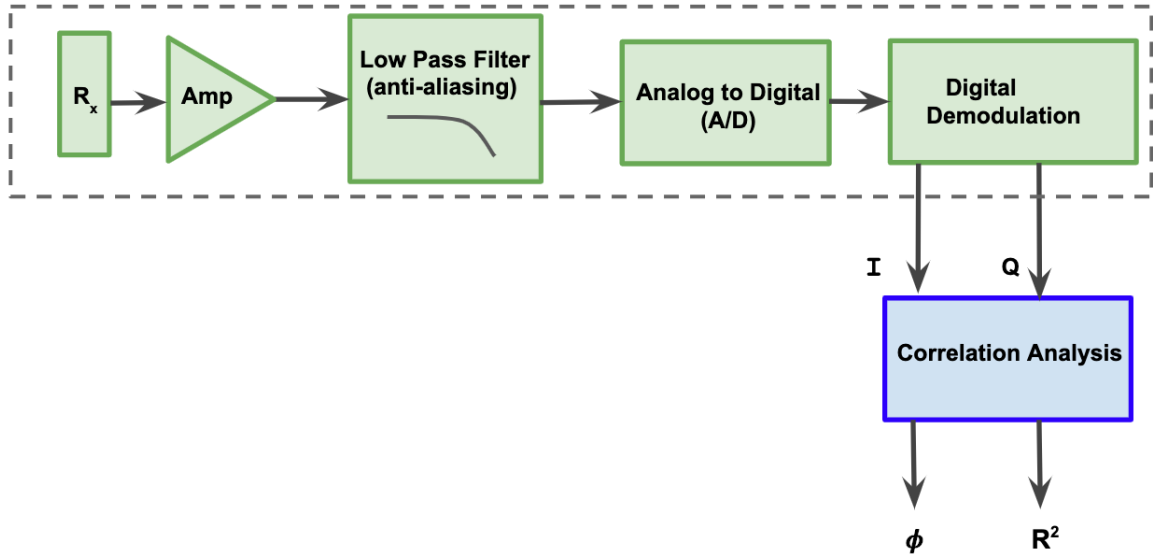


Figure 3.2: Basic sonar signal conditioning block diagram.

that will be unique to the Doppler sonar is the correlation analysis. Section 3.2 will discuss the correlation analysis for narrowband, pulse-to-pulse and broadband Doppler sonar.

## 3.2 Classifications of Doppler Sonar

Doppler sonar is a classification of sonar that uses the Doppler shift in received frequency to measure the movement of objects, this is an enhancement on basic sonar (Section 3.1) which estimates target range. There are three different types of Doppler sonar systems used in oceanography: narrowband, pulse-to-pulse coherent and broadband. These sonar systems were developed sequentially and each has operational advantages and disadvantages. Here, we will classify and differentiate between the three different device types while highlighting their utility.

Narrowband Doppler, sometimes referred to as incoherent Doppler, was the original method of Doppler sonar used for oceanographic measurements. This method uses the active sonar (Equation 3.1) sending pulses with a bandwidth of approximately 10 % the carrier frequency and records the acoustic return (Brumley et al., 1991). The method assumes that echoes from single pulse pings are uncorrelated, hence, the name incoherent. The device estimates the Doppler shift from the detected echoes by either applying a covariance method in the time domain or estimating a frequency peak in spectral space (Brumley et al., 1991). The covariance method compares (typically) sequential points in the pulse return and the phase of the (complex) autocorrelation is a measure of the signal rate of phase change (the frequency) of the returned signal time series (Miller and Rochwarger, 1972).

Narrowband Doppler is constrained by a trade off between high range resolution and high accuracy velocity measurement, it can provide fine velocity resolution but the required long transmit pulse will create poor range resolution. This trade off arises from the large bandwidth required for short acoustic pulses used for fine range resolution. Bandwidth is proportional to the inverse of the pulse length ( $BW \propto 1/t$ ) suggesting that the smaller the pulse length the larger the bandwidth and the smaller the pulse length the finer the range resolutions as it is proportional to  $Ct/2$ . However, the presence of a large range of frequencies (large bandwidth) results in poor velocity resolution, as each frequency undergoes a different Doppler shift leading to increased uncertainty. This trade off between resolution and accuracy is the biggest limit to incoherent Doppler operation and necessitates long time averages in the post processing (Brumley et al., 1991).

Pulse-to-pulse coherent Doppler, often referred to as coherent or pulse-to-pulse Doppler, transmits short pings of sound in quick succession and estimates the Doppler shift from the observed phase changes in the successive returned signal (Brumley et al., 1991; Pinkel, 2016). Coherent Doppler measures the phase difference from one return pulse ( $n$ ) to the next return pulse ( $n + 1$ ), in effect measuring how far targets are moving relative to the wavelength of sound. The measured phase shift ( $\phi$ ) is a proxy for the observed velocity. The values of phase shift can only be determined over a  $2\pi$  interval spanning from  $[-\pi, \pi]$ . Values that are outside these bounds will be folded back resulting in phase jumps or wraps. The uncertainties in phase from these jumps will translate into errors in velocity space. If targets move towards or away from the sonar in the time between pulse transmissions (ie. greater than  $\lambda/4$ ), phase wrapping and the associated uncertainty will be present.

The ambiguity velocity is a consequence associated with (or equivalent to) the occurrence of phase wrapping and it provides a range of velocities ( $[-V_{\text{amb}}, +V_{\text{amb}}]$ ) that the sonar can record. Ambiguity velocity is defined by:

$$V_{\text{amb}} = \frac{C}{4 f_c \tau_p} \quad , \quad (3.5)$$

where  $f_c$  is the sonar carrier frequency,  $\tau_p$  is the time interval between emitted pulses and  $C$  is the assumed speed of sound in the ocean (Dillon, 2011; Dillon et al., 2012). Ambiguity velocity is a characteristic of both coherent and broadband sonar. The observed velocity can be related to the ambiguity velocity (Equation 3.5) and the phase shift by:

$$v = \frac{\phi}{\pi} V_{\text{amb}} \quad , \quad (3.6)$$

where  $v$  is measured velocity and  $\phi$  is the phase shift.

There is a relationship between maximum range and maximum velocity for coherent Doppler (ie. velocity-range ambiguity) given by:

$$U_{\max} R_{\max} \leq \frac{\lambda C}{8} \quad , \quad (3.7)$$

where  $U_{\max}$  and  $R_{\max}$  are the maximum velocity and range values, respectively. As the maximum range is increased the maximum velocity must decrease in order to satisfy the condition for the velocity-range ambiguity factor. The opposite balance must also be true; to reduce the occurrences of phase wrapping and hence improve the velocity ambiguities the time between consecutive pulses can be decreased (see Equation 3.5) (Lhermitte and Lemmin, 1994; Dillon, 2011). The problem of large velocity-range ambiguity is due to the fact that this method of Doppler sonar operation requires that the amount of time separation between pulses be greater than the travel time to the maximum profiling range (Brumley et al., 1991). In short, pulse-to-pulse coherent Doppler collects precise observations but has a profiling range regulated by the velocity-range ambiguity (Equation 3.5) (Brumley et al., 1991).

The pulse-coherent method assumes a correlation between pulse pairs in the detected signal, accordingly the name coherent Doppler. Doppler shift measurements quality is estimated using the magnitude of the backscatter autocorrelation, commonly referred to as the correlation (Zedel, 2014). The backscatter autocorrelation is estimated by the sonar from a series of returned pulses and given by (Dillon et al., 2012; Zrnic, 1997):

$$\hat{R}(\tau) = \frac{1}{M} \sum_{n=1}^M z_n^* z_{n+1} \quad , \quad (3.8)$$

where  $z_n$  is the series of backscatter returns,  $*$  represents the complex conjugate and  $M$  is the number of returned pulses. This method is commonly referred to as the “pulse-pair” estimator and depends on a complex auto-covariance signal consisting of both an in-phase ( $I(t)$ ) and quadrature ( $Q(t)$ ) signal see Figure 3.1 (Lhermitte and Serafin, 1984). The resulting complex signal contains information about the spectrum width and variance (Lhermitte and Serafin, 1984). The magnitude of the autocorrelation is given by

$$\rho(\tau) = \left| \frac{R(\tau)}{R(0)} \right| \quad , \quad (3.9)$$

where  $\tau$  is the interval of time between the pulses of sound emitted from the sonar and provides a range of values between 0 and 1 (Dillon et al., 2012). If the value is less than or equal to 0.5 then the collected data will be of low quality or confidence (Zedel, 2014). The closer the correlation magnitude is to 1 the better the data quality and the more confidence can be placed on the results (Zedel, 2014). Taking this concept one step farther, the correlation ( $R^2$ ) can be related to the velocity variance by:

$$R^2 = \exp \left( - 2\pi^2 \tau_p^2 (4f_c^2 / C^2) \sigma_v^2 \right) \quad , \quad (3.10)$$

where  $\sigma_v^2$  is the velocity variance.

The development of broadband Doppler is an innovation that combines the advantages of incoherent and pulse-to-pulse coherent Doppler sonar (Brumley et al., 1991).

This approach also reduces the difficulties introduced by velocity-range ambiguity (Equation 3.7) that are seen in the coherent Doppler. Broadband sonar projects a pair of acoustic pulses and waits to detect the acoustic backscatter (Brumley et al., 1991). Broadband sonar emits a larger bandwidth of frequencies, and therefore it receives an acoustic backscatter signal with more information about the location, and/or size of the targets. The velocity-range ambiguity challenge identified for pulse-to-pulse coherent Doppler is addressed by allowing the detection of multiple returns simultaneously, this is achieved in part by decreasing the time separation between pulses of emitted sound (Brumley et al., 1991).

The signal processing approach is the same as that applied to coherent Doppler sonar, the only difference being the range of achievable correlation coefficients. The simultaneously received sounds echoes are not separated but instead a covariance method is applied to correlate the echoes within the single return. In the case of broadband Doppler sonar an average backscatter correlation of 0.5 is expected as the system receives backscatter from both of the transmitted pulses at the same time. In this case, only half of the returned signals energy is coherent. This reduced correlation contrasts with the pulse-to-pulse coherent approach where correlation coefficients can routinely approach 1.

Each of the Doppler sonar instrument classifications discussed here (narrowband, coherent, and broadband) have operational advantages and limitations. Conventionally, these instruments are used for measuring ocean currents, however, Doppler sonar has been used for fish or mammal monitoring and for observing smaller scale ocean dynamics. Narrowband Doppler has particular applications in studies where long ranges are required and a loss of velocity accuracy can be managed by greater averaging.

Coherent Doppler sonar has application when high resolution velocity measurements are needed for example: measuring ocean currents (Hackett et al., 1987), sediment transport (Williams et al., 2003; Hare and Hay, 2018) and turbulence (Hay et al., 2012). Coherent Doppler is the basis of operation for all point measurement Acoustic Doppler Velocimeters (ADV). This study will simulate the performance of two types of broadband Doppler sonar in measuring turbulent velocities. Section 4.3 will discuss various applications of Doppler sonar including the measurement of turbulent velocities.

# Chapter 4

## Measuring Ocean Turbulence

Oceanic turbulence can be measured using a variety of techniques, including; Optical Turbulence Sensors (OTS) (Bogucki et al., 2007), electromagnetic current meters (Elliott, 1984), temperature & salinity probes, hot wire anemometers, shear probes (Fer and Paskyabi, 2014), velocimeters, and Doppler sonars (McMillan et al., 2016; Shcherbina et al., 2018). This chapter will focus on the performance of three techniques used for measuring oceanic turbulence (1) shear probes, (2) velocimeters, and (3) Doppler sonars (Section 4.1 to 4.3, respectively). Other techniques are less prevalent in current day oceanography. For instance, optical measurements of turbulence such as LiDAR (Light Detection and Ranging) systems are frequently used in atmospheric research. However, due to the high rate of light attenuation in seawater, optical sensing is not commonly used by oceanographers (Knauss, 1987). Similarly, hot wire anemometers are a proven technique used for observing turbulence in the atmosphere (Sibert et al., 2006), however; the application of hot-wire anemometers is more challenging in the ocean (Patterson, 1958). In water, hot-wire anemometers tend to develop a film which affects the calibration or sensitivity of the instrument and, hence; the quality of the turbulent observations (Patterson, 1958; Stewart and Grant, 1999).

## 4.1 Shear Probes

In-situ instruments, such as shear probes, are a standard method of collecting turbulent velocity data in the ocean, they record measurements by tracking the deflection of the physical probe (Osborn and Crawford, 1980). These instruments collect high-accuracy small scale velocity information within a compact volume. Shear probes have been widely applied to oceanographic studies and are considered a proven method (McMillan et al., 2016; Fer and Paskyabi, 2014; Lueck et al., 1997).

The first applications of shear probes in measuring velocity microstructure occurred in the early to mid-1970s. The pioneers of this advancement include Simpson (1972), Osborn (1974) and Oakey (1982). The design of a prototype shear probe is given by Simpson (1972) along with results from an experimental trial conducted in Loch Ness (a freshwater lake), Scotland. Results found that 50 % of the experimental shear probes produced an acceptable quality of velocity profiles. The shear probe design used in Osborn (1974) is partly based on Simpson (1972) but technical advancements allowed for higher resolution data and direct estimates of energy dissipation.

In later years, shear probes have been used in deployments alongside other instruments that collect complimentary data. Lueck et al. (1997) collected autonomous time series data of turbulence in the dissipation subrange using a moored microstructure instrument. The moored instrument is called the Tethered Autonomous Microstructure Instrument (TAMI) and consists of four shear probes, thermistors and conductivity, temperature and depth (CTD) sensor (Lueck et al., 1997). The instrument was deployed in Satellite Channel which connects the Georgia Strait to the Pacific Ocean for a period of 59 hours. The study observations verified the performance of the in-

strument in estimating rates of energy dissipation by comparing results to theoretical expectations given by the Nasmyth universal spectrum (Lueck et al., 1997).

Fer and Paskyabi (2014) build off previous studies including Lueck et al. (1997) and presents the Moored Autonomous Turbulent System (MATS) which has longer data collection capabilities compared to the TAMI system presented by Lueck et al. (1997). The MATS instrument includes two shear probes, an acoustic Doppler velocimeter (ADV), two thermistors, a pressure transducer and an inclinometer. The instrument was deployed off the coast of Norway in the Vestfjorden for a period of four days at a depth of 12 meters below the surface (Fer and Paskyabi, 2014). The study demonstrated the instrument can collect a times series of the dissipation rate but that the quality of the data is constrained in the wave-affected layer.

Shear probes are proved methods for collecting accurate velocity observations in the ocean. Fer and Paskyabi (2014) and Lueck et al. (1997) provide examples of the application of shear probes in observing oceanic turbulence while demonstrating the performance and success of these devices. Shear probes are known to be highly accurate and are considered a gold standard in observing ocean velocity.

## 4.2 Acoustic Doppler Velocimeters

Acoustic Doppler Velocimeters (ADV) are another instrument applied to a wide range of oceanic studies and are capable of collecting reliable three-component velocity measurements. These devices are acoustic and use a converging beam geometry to collect high-resolution data in small volumes of water near the device. ADVs are consider in-situ instruments. Tschegg and Hays (1959), a pioneer study, used

a transistorized acoustic velocimeter to measure the speed of sound in the Mediterranean, North Atlantic and the Tongue of the Ocean (Bahamas) over a three month deployment. The results were found to be correct within 1 / 10,000 parts proving the instruments ability to collect accurate velocity observations.

ADVs are different from Laser Doppler Velocimeters (LDV) that use light to collected observations. ADVs are more versatile and have comparable accuracy to LDVs but they have lower spatial and temporal resolution (Lohrmann et al., 1994). Lohrmann et al. (1994) provides an assessment of ADV performance in a laboratory setting concluding that the devices ability to collect three-dimensional velocity observations is beneficial. The devices considered has a sub-centimetre resolution and a sample volume less than 1 cm<sup>3</sup>. The sample volume is determined by the device design, specifically the length of the transmit pulse, the acoustic beam pattern and the receiver window width (Lohrmann et al., 1994).

Voulgaris and Trowbridge (1996) build on the work Lohrmann et al. (1994) and provides a detailed evaluation of the performance of ADVs in measuring turbulence in a laboratory flume setting. The study concludes that ADVs are capable of measuring mean flow and Reynold Stress values to within a 1 % of the expected value. The study concludes that the ADV along beam noise variance is due to the device electronics and high flow rates (Voulgaris and Trowbridge, 1996)

A more recent study by Sulaiman et al. (2013) can serve as an example of the application of ADVs. Sulaiman et al. (2013) used ADVs to collect near-bed turbulence measurements at two locations in Hulu Besut drainage basin which has sediment composed of mainly coarse sand and small cobble. The application of ADVs successfully

measured the field flows in the near bed environment and concluded that the Turbulent Kinetic Energy (TKE) from local shear estimates can be calculated (Sulaiman et al., 2013). ADVs, similarly to shear probes are a proven method of collecting turbulent observations as is demonstrated by the examples of ADV application described above.

### 4.3 Doppler Sonar

The techniques presented in Sections 4.1 and 4.2 are challenging in our research application as tidal channels have high mean current speeds and moored instrumentation are difficult to position in these regions. Doppler sonar is an alternative approach that allows for profiling and remote sampling. Lhermitte and Lemmin (1994) consider the ability of 1 MHz pulse-to-pulse coherent Doppler sonar to measure turbulence micro-structure was tested. This experiment was completed in a 17 x 0.6 x 0.6 m flume filled with highly turbulent water flow and used two downward facing sonar beams. It was demonstrated that the instrument is able to collect encouraging measurements of turbulent micro-structure.

Lemmin and Rolland (1997) took this approach one step farther and considered the capabilities of a pulse-to-pulse coherent, high frequency, single beam Acoustic Doppler Velocity Profiler (ADVP) in measuring turbulence. The ADVP was tested in an open-channel laboratory flow before conducting field experiments in a small river and in the lake of Geneva (Lemmin and Rolland, 1997). The study concluded that ADVPs are a useful tool for measuring the characteristics of turbulence and can produce instantaneous velocity profiles setting the method apart from conventional in-situ devices. One factor setting the ADVP apart is its tolerance of high concen-

trations of suspended particles in the water.

The acoustic sampling involved in Doppler sonar limits sample accuracy, Hurther and Lemmin (2001) present a correction method that can address some of the accuracy limitations. Hurther and Lemmin (2001) proposed a variance correction method for turbulent data collected with ADVs that reduces noise contributions. The correction method is free of assumptions about the water flow and is based on cross spectral analysis of simultaneous vertical velocity measurements. Results demonstrate that the raw data does not have the characteristic  $-5/3$  Kolmogorov slope in the inertial subrange but that variance corrected data recovers this characteristic of turbulence (Hurther and Lemmin, 2001).

A more recent study, out of the University of Washington, considers the capability of a Lagrangian float mounted Nortek Signature 1000 AD2CP in resolving fine-scale velocity structure in the ocean (Shcherbina et al., 2018). The paper focuses on the application of a Multi Correlation Pulse-Coherent (MCPC) Extended Velocity Range (EVR) signal processing method to the problem of uncertainty in Doppler sonar turbulence measurements (Shcherbina et al., 2018). The MCPC EVR method accounts for decorrelation that arises as the location of the correlation peak shifts with increasing velocity. It does this by computing multiple velocity estimates, selecting the solution with the highest correlation, and then adjusts the final velocity estimate to match that result. The study concludes that the application of MCPC EVR during the processing of the AD2CP signals can increase the range, and accuracy of turbulent velocity measurements (Shcherbina et al., 2018).

McMillan et al. (2016) presents the results of field trials conducted in the North-

ern end of the Grand Passage, Nova Scotia Canada, where turbulent velocities are measured using three different acoustic instruments and the relative performance is compared. The three instruments considered in the McMillan et al. (2016) field experiment are (1) Nortek acoustic Doppler velocimeter (ADV), (2) Nortek 1 MHz Signature AD2CP, and (3) 600 kHz Teledyne RD Instruments Workhorse ADCP. The ADV was used to measure the mean water flow. Table 4.1 displays McMillan et al. (2016) operation parameters.

**Signature AD2CP**

Carrier Frequency	1	MHz
Sample Rate	8	Hz
Collection Time	5	min
Time Between Collections	15	min

Time between Pings	0.125	s
Pings per Ensemble	1	
Averaged Range Bin Size	1.5	m
Range Bin Size	12.5	cm

**Workhorse ADCP**

Carrier Frequency	600	kHz
Sample Rate	1.49	Hz
Collection Time	7	min
Time Between Collections	15	min

Time between Pings	0.69	s
Pings per Ensemble	2	
Averaged Range Bin Size	1.5	m
Range Bin Size	0.5	m

Table 4.1: Acoustic parameters used by the AD2CP & ADCP McMillan et al. (2016) field experiment. The AD2CP parameters are specific to the vertical beam.

The results of McMillan et al. (2016) demonstrate that both the AD2CP and the ADCP are able to resolve the characteristic Kolmogorov  $-5/3$  slope in the inertial subrange (mid-frequency range) but at higher frequencies, the spectrum developed into a noise floor (McMillan et al., 2016). By successfully resolving the Kolmogorov  $-5/3$  slope the rate of energy dissipation can be estimated. The study concluded that 600 kHz ADCP data can make remote estimates of turbulence but, that high levels of noise limit the accuracy of the device in estimating energy dissipation rates (McMillan et al., 2016). This thesis will make comparisons between numerical model simulations and the McMillan et al. (2016) field experiments.

Guerra and Thomson (2017) build off of McMillan et al. (2016) and related studies to improve estimates of the TKE budget. Two Nortek Signature AD2CPs and a Teledyne RDI Sentinel V50 were deployed in two tidal regions, Admiralty Inlet and Rich Passage in Puget Sound, Washington. For the purpose of validation, ADVs were deployed and simultaneous measurements of turbulence were collected. The five beam capability of the AD2CP allows for five out of six of the Reynold Stresses to be calculated which improves estimates of TKE production and dissipation rates. Guerra and Thomson (2017) found that the measured AD2CP spectrums compared well with the ADV observations.

# Chapter 5

## Model of Acoustic Backscatter

Theoretical models of Doppler sonar, sound reverberation and acoustic backscatter have been developed to better simulate the processes and limits of Doppler systems. This section will provide an overview of sonar models developed over the last twenty years. Section 5.2 will provide a complete description of the model used to simulate the measurement of turbulence in this study.

### 5.1 Introduction to Sonar Models

Doppler sonar is a tool used in both oceanography and in medicine. In the field of medicine, Doppler sonar typically called ultrasound and is based on the same fundamental concepts that are used in oceanography. Mo and Cobbold (1992) developed a model of acoustic backscatter for medical ultrasound by combining the approaches of particle modelling and continuous modelling of blood flow. Their model calculates Doppler backscatter for a fixed number,  $N$ , of blood volumes, called voxels and sums the individual contributions together to determine the overall system backscatter. With the voxel modelling method, the red blood cells can be distributed in the

model so that the scattering is partially coherent, fully coherent or fully incoherent. The model of ultrasound backscatter is used to consider the relationship between the backscatter coefficient and the amount of red blood cells in the total blood (Mo and Cobbold, 1992).

Zedel (2008) developed a model of acoustic backscatter that was used to simulate pulse-to-pulse coherent Doppler sonar. The model supported a bistatic beam geometry, consisting of one active transducer and one passive sonar (Zedel, 2008). The three-dimensional rectangular model domain is filled with multiple scatterers, each scatterer or target has a random discrete position within the model boundaries and that location is updated using an imposed velocity field as time evolves within the model. The study found the model is able to reproduce statistical backscatter expectations and laboratory results (Zedel, 2008, 2015).

In a subsequent study, the acoustic backscatter model is used to simulate a bistatic Doppler system called the Vectron, which is intended for resolving turbulence and results from a Nortek Vectrino Profiler simulation. Zedel (2008) demonstrates that the model is useful when designing new acoustics instruments such as the Vectron. Zedel (2008) also demonstrates the utility of the model in considering the performance or effects of instruments. The model developed by Zedel (2008) and presented again in Zedel (2015), is the foundation for this thesis, and it will be described fully in Section 5.2.

In parallel evolution with the models of volume acoustic backscatter, models of echo reverberation have been developed. Murray (2014) developed a statistical model of active sonar reverberation, which is specific to reverberation in shallow water and

assumes that acoustic reverberation is made-up of echoes from individual targets. The model uses planar bistatic geometries and assumes a motionless medium with a uniform sound speed. Murray (2014) discusses the importance of Doppler time dilation in the modelling of sonar reverberation, and the effects of propagation loss on backscatter signals. They acknowledge that the model is limited by the planar approximation but conclude that the model could provide scientific insight into the structure of reverberation in shallow waters (Murray, 2014).

An alternative approach to simulating the performance of Doppler sonar is to carefully subsample the model domain instead of directly modelling the operational parameters of the sonar. Crossley et al. (2017) introduces a Virtual Doppler Current Profiler (VDCP) to consider the limits of acoustic measurements in tidal flows (Crossley et al., 2017). A simulated tidal flow consisting of mean flow, shear, wave, and turbulent velocities is sub-sampled using a two beam geometry. Their model does not simulate the acoustic operation of the ADCP but instead simulates the sampling characteristic of the four diverging beams in a turbulent environment. The results demonstrate that VDCP sampled turbulent intensities, and turbulent length scales depend on the models input wave, and current conditions (Crossley et al., 2017). In model simulations with a low input wave condition the turbulent intensities were found to vary between 0.2 and 1.5 times the expected values of turbulence (Crossley et al., 2017).

## 5.2 Model of Acoustic Backscatter: Description

This study builds on the backscatter model used to simulate Doppler sonar measurements described by Zedel (2008, 2015) and discussed briefly in Section 5.1.

The model allows for various transducer orientations and beam geometries, including control of the transducer angle relative to the vertical. The configuration parameters also allow changes to the transducer size and resulting beam width, which will be considered in Section 7.3.1. Other configuration parameters include pulse length, sample rate, carrier frequency, bandwidth and length of data collection. Control over these parameters leads to a large scope of Doppler devices that can be simulated. In this thesis, the model has been used to simulate turbulence measurements in flows similar to those that occur in tidal channels using broadband Doppler sonars.

The model uses a three-dimensional rectangular domain that has periodic boundary limits. Initially, the domain is populated with a fixed number of randomly placed discrete targets that are used to calculate the accumulative acoustic backscatter signal. The number of targets in the model can be adjusted but often a large number of targets is required to ensure that each sample volume defined by the acoustic transducers has at least one target at all times. Typically 5 scatterers are required per sample volume (Dillon et al., 2011). Without enough targets per sample volume the models statistics will be effected, which may result in data aliasing. The location of these targets evolves in time based on the models prescribed fluid properties (eg. how much time has evolved and what is the velocity of the fluid at that location). If a target is advected outside of the domain then the particle gets wrapped about the axis and randomly moved in the other two dimensions (Zedel, 2015). The process of randomizing positions in the model is essential in ensuring uniform spatial sampling in resulting time averages (Zedel, 2015). This process also ensures that the quantity of targets in the domain is fixed for the entire simulation.

A schematic of the model domain initialized with discrete targets is shown in Fig-

Figure 5.1 (a). The colours represent the velocity of these targets at an instantaneous moment in time. Warm colours indicate fast movement of targets while the cool

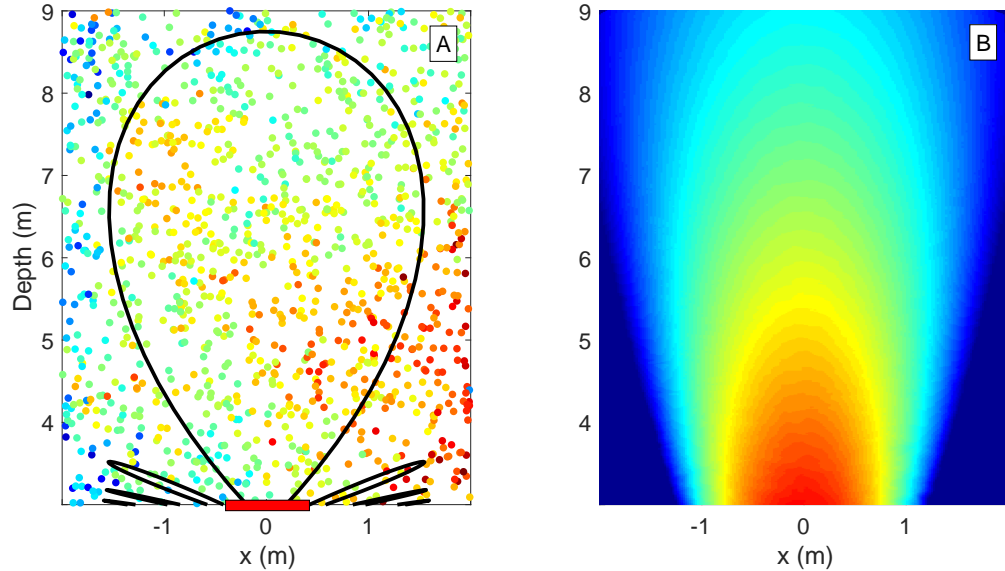


Figure 5.1: Acoustic backscatter model domain, colours represent the speed of the targets at a fixed time, warm (cool) colours represent fast (slow) movement (a). A beam pattern generated by the model, warm (cool) colours represent regions with high (low) scatter contributions (b).

colours mark the slower instantaneous velocities. The model allows the location, orientation, and operation parameters of the acoustic transducers to be specified. Figure 5.1 (a), includes a schematic of an acoustic transducer (orange cylinder) located on the bottom of the model domain. The model creates a realistic transducer beam pattern (black line), which indicates that some regions of the model will make a high contribution to the total estimated backscatter signal. In the case of a single transducer placed at the bottom on the model domain looking upwards, a beam pattern

such as the one seen in Figure 5.1 (b) is generated.

The total sonar backscatter calculated in the model is based on the summation of individual backscatter amplitudes from each discrete target in the domain. The total Doppler sonar backscatter  $S(t)$  is given by (Zedel, 2015):

$$S(t) = \sum_i^n a_i s\left(t - \frac{(r_{si} + r_{ri})}{C}\right) , \quad (5.1)$$

where  $r_{si}$ , and  $r_{ri}$  are the distances between source transducer to the  $i^{th}$  target, and  $i^{th}$  target to the receiver, respectively. The target amplitudes of an  $i^{th}$  target is represented as  $a_i$ , and  $s(t)$  denotes a copy of the transmit pulse (Zedel, 2015). Equation 5.1 is applied in the model each time the sonar pings in order to calculate the detected signal. A completed model simulation will return backscatter amplitude, Doppler phase shift and the “pulse-pair” correlations, as will be used in data analysis (Chapter 7 & 8).

The models targets are advected through the acoustic domain in time. The displacement of individual targets depends on the evolution of time as well as, both a horizontal mean velocity ( $\overline{u_i}$ ) and a turbulent velocity ( $u'_i, u'_j, u'_k$ ) component. This is in fact an application of Reynolds Decomposition (Equation 2.4). The acoustic backscatter model developed by Zedel (2008) used synthetic turbulence (described in Section 2.2) to advect the targets through the model domain. The addition of turbulent velocity fluctuations using synthetic turbulence allows the motion of the targets to statistically reproduce the energy spectrum of turbulence but the motion does not retain the hydrodynamic characteristics of turbulence. In other words, the method of synthetic turbulence does not incorporate, or allow for adequate spatial

correlations. A more complete description of turbulence is therefore, required in order to simulate the measurement of turbulence with broadband sonar and to consider the device performance. A full description of the new turbulence framework that will replace synthetic turbulence is presented in Section 6.3, the new framework involves integrating output from a DNS of forced isotropic turbulence into our model. The forced isotropic turbulence data will be used to determine a turbulent velocity fluctuations  $(u'_i, u'_j, u'_k)$  needed to update the locations of the individual targets in time.

Additional model developments were necessary to meet the study requirements of simulating broadband Doppler sonars. Time dilation and the resulting phase changes are a critical capability for accurately modelling broadband and/or narrowband systems. Therefore, a validation of the time dilation algorithm was completed and is presented in Section 6.1.

Recovering phase and frequency information from the acoustic backscatter signal depends on the signal processing procedures. One of the more common signal processing techniques is the covariance or “pulse-pair” method (Lhermitte and Serafin, 1984) see Section 3.1. Developments to the signal processing technique were of importance as the model presented in Zedel (2008) utilized an analog processing method to be consistent with the latest generation of Doppler sonar processing this needed to be replaced with a digital demodulation.

# Chapter 6

## Model Developments

For the study of turbulent measurements, three major developments to the model presented by Zedel (2008, 2015) were required: (1) validation of the models time dilation algorithm (2) upgrade to the signal processing technique to incorporate digital demodulation and (3) replacement of synthetic turbulence with forced isotropic turbulence data. Model developments (1) and (2) are specific to the modelled acoustic device and will be discussed in Section 6.1 and Section 6.2, respectively. Modifications to turbulence and the corresponding time-evolving target movement will be presented in Section 6.3.

### 6.1 Time Dilation & Doppler Shift

The model of acoustic backscatter was designed to simulate a variety of Doppler sonar systems including narrowband, pulse-to-pulse coherent and broadband sonar systems. Section 3.2 describes the differences, advantages, and disadvantages of these systems. The accuracy of our acoustic backscatter model depends on the proper representation of time, which is a non-trivial task, as the model includes a number of

unique time steps and time dependent variables. In particular, time dilation and the resulting Doppler frequency shift is critical for simulating broadband processing, such as the acoustic simulations considered in Chapter 7 and Chapter 8.

Time dilation is the source of the Doppler shift in frequency and it arises when the motion of a target shifts the frequency content of the scattered sound; this corresponds to a dilation (or contraction) in the time domain. In the model, this can be mathematically expressed as follows (Zedel, 2015);

$$t' = t \left( 1 - \frac{2V_r}{C} \right) , \quad (6.1)$$

where  $t'$  is the dilated time and  $V_r$  is the radial velocity measured from the acoustic backscatter relative to a transducer. The time and associated scattered signal for each individual acoustic target in the model is scaled according to Equation 6.1. A Doppler shift can be estimated in spectral space by selecting a frequency peak or in the time domain using an autocorrelation method (see Chapter 3). Our model of acoustic backscatter applies the autocorrelation approach and in the case of the broadband simulations presented here, this approach involves considering the correlation between returned pulses.

Doppler shift is defined as the difference between perceived frequency when an object is at rest compared to when it is in motion (Gordon, 1996). For instance, imagine a ship mounted sonar is measuring horizontal water movement, when the ship is moving against (with) the net current the sonar will record a lower (higher) frequency than when the ship is at rest. Doppler shift is the product of time dilation resulting from sound scattered off moving targets. In the case of Doppler sonar, the

Doppler shift is denoted as the difference between the frequency emitted from the transducer and the frequency received after interacting with scatterers;

$$\Delta f = f_R - f_T \quad , \quad (6.2)$$

where  $\Delta f$  is the change in frequency,  $f_T$  is the frequency of sound emitted, and  $f_R$  is the frequency detected. An estimate of the scatterer velocity from the Doppler shift can be given as:

$$V_r = \frac{C}{2} \frac{\Delta f}{f_T} \quad , \quad (6.3)$$

Equation 6.3 is derived by substituting Equation 6.2 into Equation 6.1 and applying the rule that frequency is inversely proportional to time. A little manipulation is required and the assumption that  $1 \gg 2V_r/C$  is applied in order to achieve the scatter velocity equation (Equation 6.3). Doppler shift will only occur if sound interacts with moving targets. If all the scatterers in the medium were stationary a frequency shift would not be observed. In this study, the movement of the targets will be controlled by a forced isotropic turbulence dataset.

### 6.1.1 Validating the Time Dilation Algorithm

An experiment was designed to validate time dilation in the model. The transducer geometry was set to be a single transducer fixed at the bottom of the model domain and vertically measuring backscatter from a single target. The experiment geometry shown in Figure 6.1 includes a single backscatter target (green circle) that was placed in the center of the model domain, the target was fixed in the horizon-

tal direction but forced to move in the vertical. The targets vertical position was randomised throughout the experiment as was the prescribed velocity. This set-up differs from the conventional model parametrization as the domain is not populated with a large number of randomly placed targets (see Chapter 5 for more). The simple

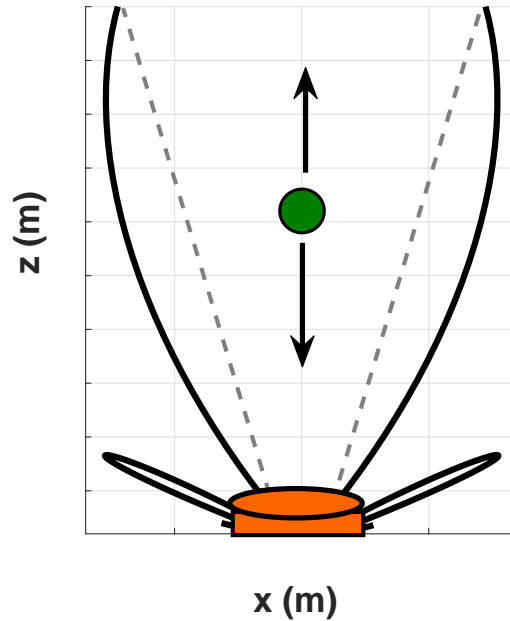


Figure 6.1: Schematic of the acoustic model domain for the time dilation experiment, including a transducer (orange cylinder), target (green circle), 3 dB width (black dotted lines) and beam pattern (solid black line).

model configuration was selected so that the expected Doppler shift was known and could be directly compared to the experimental result. Acoustic backscatter data was generated for a known radial velocity of the target and then the Doppler shift was determined using a frequency fitting method. A Fast Fourier Transforms (FFT) approach was not applied as a precise frequency value was more advantageous than a spectrum of frequencies. The frequency fitting approach is given by:

$$\sigma = \sum \left| S(t) - \left( A \sin(\omega t + \phi_s) + \delta \right) \right|^2, \quad (6.4)$$

where  $\sigma$  is the fitting parameter,  $S(t)$  is the returned sound signal calculated from the model and the second term on the right hand side is the expected returned signal based on the known input velocity. In the second term,  $A$  is the amplitude of the signal,  $\omega$  is the known angular frequency,  $\phi_s$  is the signal phase and  $\delta$ , an overall offset from zero. The frequency fitting method works by taking initial estimates for the parameters in the second term of Equation 6.4 and jiggles them until an optimal frequency fit was achieved. The experiment aims to demonstrate that the frequency of our backscatter signal ( $\omega$ ) matches the expected Doppler shifted frequency of the transmit pulse thereby demonstrating the time dilation is implemented and operating as expected.

Five thousand experiment iterations were completed with the vertical target position updating each time while the horizontal position remained fixed. The results were considered in the form of normalized error ( $E_n$ ):

$$E_n = \frac{(f_d - \omega/2\pi)}{f_d}, \quad (6.5)$$

where the expected Doppler shifted frequency is represented by  $f_d$ . It was found that the normalized error gives approximately a Gaussian distribution centred at zero, this result was shown in Figure 6.2. The mean normalized error is  $-0.0065$  and the median is  $-0.0050$ , suggesting that the anomalies between the expected and calculated Doppler shifted frequencies are close to the expected value of zero.

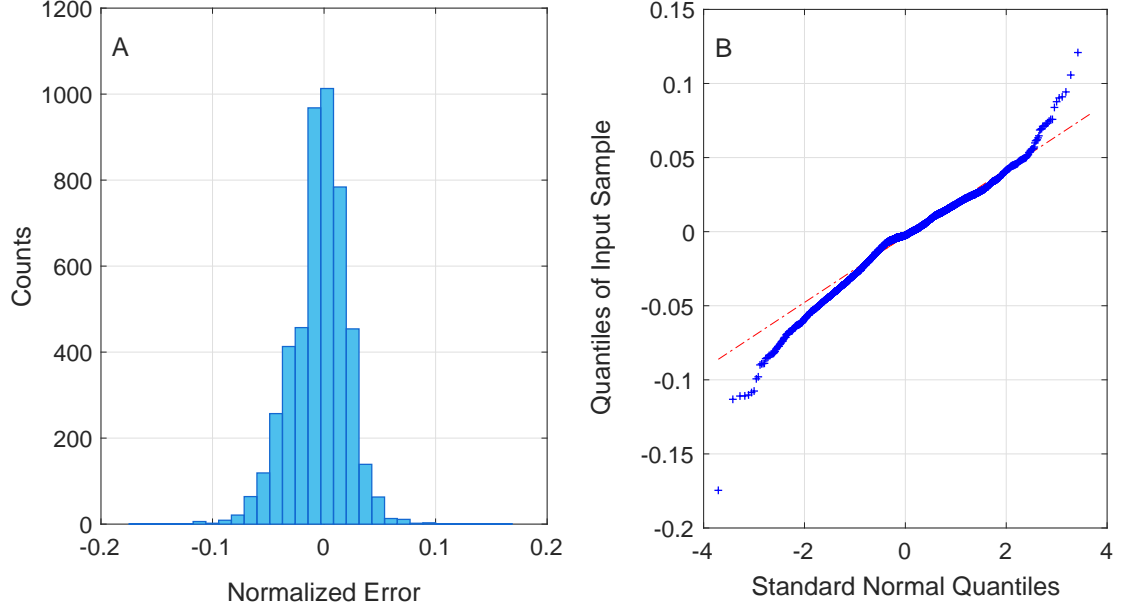


Figure 6.2: Histogram of normalized error ( $E_n$ ) for five thousand occurrences of the time dilation experiment (a) and a QQ-plot of the distribution (b).

To demonstrate normality in the distribution of error, a quartile-quartile plot is generated, see Figure 6.2 (b). The estimation of Doppler shift was performed with a frequency fitting method that attempts to best calculate the value based on priors and is dependent on the dispersal of data ( $S(t)$ ). If there are regions of data that are sparse, the frequency fit algorithm might over or underestimate the real value of the function and thereby, introduce anomalies. Therefore, this approach can lead to unavoidable irregularities in the estimates calculated for then Doppler frequency and explains the deviations at larger quartiles in Figure 6.2 (b). To further support our conclusion of normality, a skewness test was performed and found the distribution has skewness of  $-0.39$ . Since, the value of skewness found is between  $-0.5$  and  $+0.5$ , it can be concluded that the distribution approximates a normal distribution.

## 6.2 Signal Processing

Signal processing is a critical component in the development of Doppler devices and it is therefore, an important consideration when modelling acoustic backscatter. Older generations of Doppler sonar systems use an analog demodulation to process the acoustic return signals. Figure 6.3 is a block diagram of analog demodulation showing the process that separates a modulated acoustic signal,  $C(t)$ , into two separate signals; an in-phase,  $I(t)$ , and a quadrature,  $Q(t)$ , signal (Lyons, 2011; Lhermitte and Serafin, 1984). Analog signal processing involves the use of signal mixers and low pass filters (LPF), a signal with a frequency approximately equal to the carrier frequency enters the circuit and a signal with a mean frequency of zero exits the circuit.

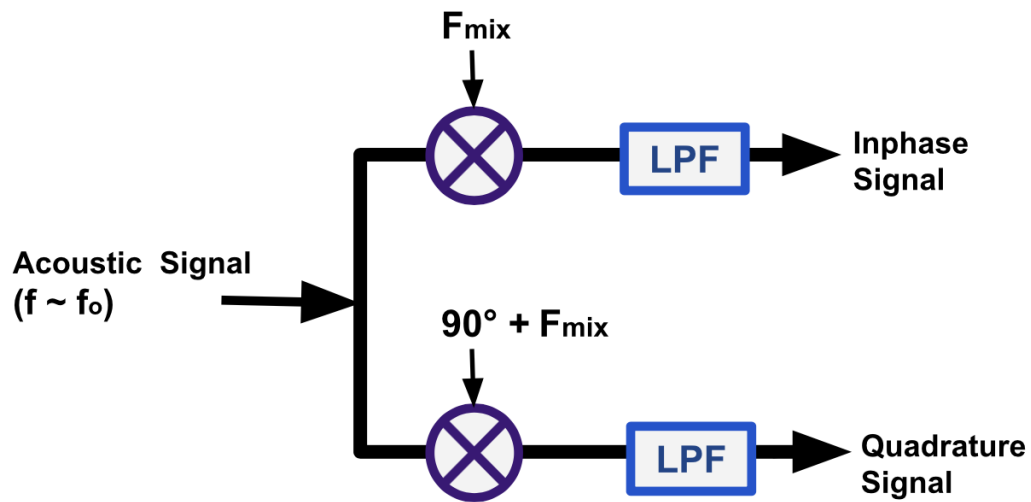


Figure 6.3: A block diagram of analog demodulation circuit, showing the separation of an acoustic backscatter signal into an in-phase signal and a quadrature signal.

Development in high-speed digitizing and computation has allowed much of the

analog signal conditioning in Doppler sonars to be replaced by digital systems. The model presented by Zedel (2008) simulated an analog demodulation approach; which is replaced by a digital demodulation scheme in this study. Digital demodulation is based on the quadrature sampling approach (Lyons, 2011) and careful manipulation of signal aliasing in the resultant samples. The basic method of digital demodulation are re-sampled data at a rate of four times the carrier frequency (Lyons, 2011):

$$f_s = \frac{4 f_c}{2 \mathcal{K}_d - 1}, \quad \text{where, } \mathcal{K}_d = 1, 2, 3, .. \quad (6.6)$$

where  $f_s$  is the re-sampling frequency,  $f_c$  is the carrier frequency, and  $\mathcal{K}_d$  is a sub-sampling parameter that can be any negative or positive integer (Lyons, 2011). Setting  $\mathcal{K}_d$  to 1 the re-sampling method collapses back to quadrature sampling. If  $\mathcal{K}_d$  is greater than 1, the sampled points of a sine wave will be indistinguishable from a sine wave of  $f_c + \mathcal{K}_d f_s$ . This means that there is a frequency ambiguity and an infinite number of possible sine waves that fit the sample points (Lyons, 2011). Figure 6.4 is a diagram demonstrating the frequency ambiguity in points sampled from a sine wave. The figure shows multiple possible sinusoidal waves that fit sampled data points (black dots) from an actual distribution (black line). It is possible to fit a lower frequency sinusoidal wave (green dashed line) or a high frequency wave (blue dashed line), however, since the signal bandwidth is limited, it puts a bound on the range of possible frequencies and it is possible to choose  $\mathcal{K}_d$  greater than 1 (reducing the required sample rate) but still resolving the necessary signal bandwidth.

The sampling frequency ( $f_s$ ) calculated using Equation 6.6 is used in the model to determine the time step at which to re-sample the backscatter signal. The model architecture introduces a constraint on the re-sampling by requiring that the rate

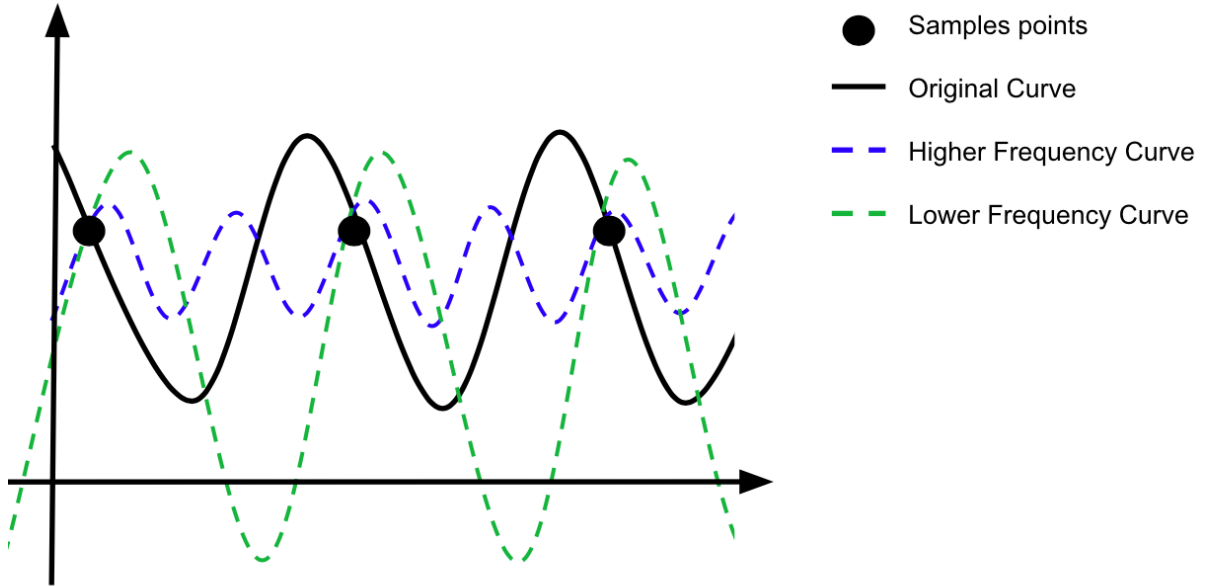


Figure 6.4: Diagram of sampling sinusoidal waves, showing that multiple functions can be fitted to the data.

of decimation is an integer value which presents limitations on value of the carrier frequency allowed. This constraint become important when simulating the Workhorse ADCP in Chapter 8.

A simple experiment was performed to test that the implemented digital demodulation method produces the same results as the previously implemented and proven analog method. The demodulation comparison experiment places a single upwards looking transducer on the bottom of the model domain which for our purpose is analogous to place the transducer on the ocean floor. However, instead of populating the model domain with a large number of randomly placed targets, this experiment uses

a single target with a fixed location at the center of the model domain. This experimental configuration is similar to that used when validating time dilation (Section 6.1), except that target is not free to move in the vertical direction instead it is forced in a static position. Fixing a single backscatter target at the center of the domain will allow for a straightforward comparison between the analog and digital approaches as it will reduce the complexity of the backscatter signal.

Identical model data was processed using both the analog demodulation approach and the digital demodulation approach the results are shown in Figure 6.5. The top panel presents the in-phase signal calculated with the analog method (red dashes

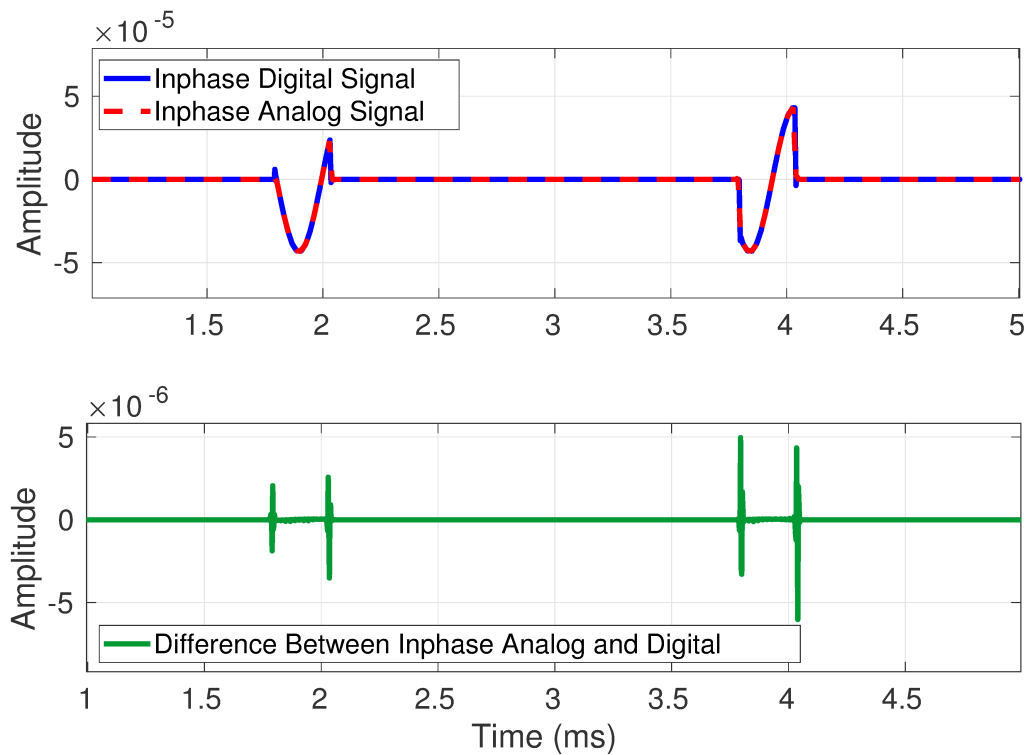


Figure 6.5: Comparison of analog and digital signal processing techniques. The lower panel shows the difference between the results

line) and the same variable calculated with the digital method (blue line). The lower panel highlights anomalies in the results by taking the difference between the analog and digital in-phase calculations. The difference between the two demodulation techniques is an order of magnitude smaller than signal amplitude everywhere except for at the edge of the return pulse. The effect seen at the edge of the pulse return is caused by the low pass filtering in the analog demodulation method. The filtering techniques used in the analog approach are absent in the digital approach, and hence, the anomaly seen at the pulse edge is expected. In summary, this experiment has used a simple model geometry to demonstrate that the newly implemented method of digital demodulation is working as expected, and produces the same result as the analog method used in earlier versions of the model.

### 6.3 Integration of Turbulence Database

Synthetic turbulence is a velocity times series that has a characteristic Kolmogorov spectrum (see Section 2.1) and it is commonly used as an initial boundary condition or model input for computational fluid dynamic (CFD) models (Jarrin, 2008). Synthetic turbulence can be generated from the Kolmogorov energy spectrum by applying an inverse Fourier transform technique. The acoustic backscatter model that Zedel (2008, 2015) presents uses synthetic turbulence to generate the time evolving locations of the acoustic targets; however, this method does not reproduce the three-dimensional spatial correlations that must exist between particles in a fluid. This study aims to simulate turbulence measurements using broadband Doppler sonar which requires correct spatial correlations in all directions and therefore, the method of synthetic turbulence is not adequate to represent the required collective motion of the particles. To address this problem, a turbulent data-set generated from a direct

numerical simulation (DNS) will replace synthetic turbulence in the acoustic model. This Chapter describes the turbulence data-set and its integration into the acoustic backscatter model.

### 6.3.1 Johns Hopkins Turbulence Database

The open numerical turbulence laboratory based at Johns Hopkins University has developed a DNS mode of forced isotropic turbulence and made the resulting 27 TB dataset publicly available. (Lia et al., 2008; Burns et al., 2018). Johns Hopkins Turbulence database (JHTDB) is periodic in three-dimensions (  $X, Y, Z$  ) and has  $1024^3$  nodes (Lia et al., 2008). The dataset includes the three components of velocity (  $U, V, W$  ) and evolves in time (  $T$  ). This study requires that the turbulent input is periodic in only one dimension, therefore, the full JHTDB is not required for the acoustic simulations presented in Chapter 7 and 8. An advantage to only requiring one periodic direction is a reduction in the amount of storage required. The subset of the database has dimensions:  $1024 \times 200 \times 512$  and spans from 0 to a final time  $T_f$ . In this thesis, the 3 TB of downloaded JHTDB data will be referred to as the Reference Turbulence.

The Reference Turbulence is dimensionless (Wan et al., 2018), Figure 6.6 (a) shows a two dimensional slice of unscaled  $U$  component of velocity at a fixed time. A turbulent energy spectrum generated from the dataset is shown in Figure 6.6 (b), for a detailed explanation of calculating energy spectrums see Appendix 9.2. The spectrum demonstrates that the reference data has the characteristic  $-5/3$  Kolmogorov slope and shows the transition to dissipation scales from the inertial subrange. The presence

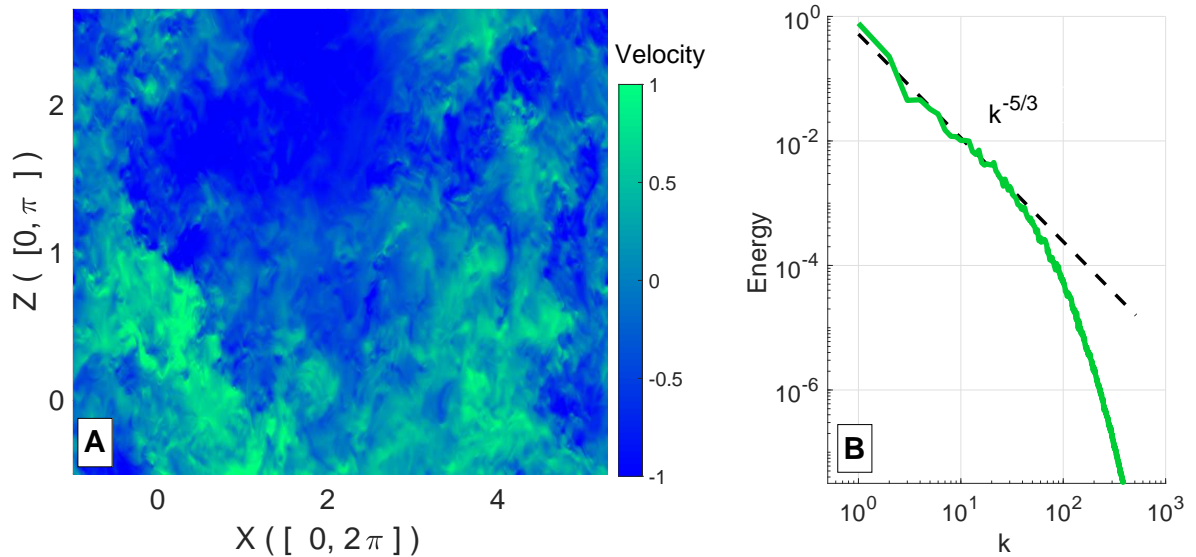


Figure 6.6: Two dimensional unscaled slice of  $U$  from the Reference Turbulence (a) and the turbulent energy spectrum (b).

of the Kolmogorov slope indicates the rate of energy dissipation ( $\epsilon$ ) can be calculated from the Reference Turbulence and therefore, should be recoverable from the simulated measurements of velocity.

### 6.3.2 Scaling the Reference Turbulence

Careful consideration must be taken when scaling the Reference Turbulence as all of the variables and dataset properties are interconnected. When scaling the dataset it is important to keep the laws of kinematics (ie. velocity = distance / time) in the forefront of thinking and to ensure that the properties of turbulence are physically reasonable after scaling. Included in the model configuration are parameters that will scale the time and velocity components of the Reference Turbulence which will force

a scaling factor on the distance. The time and velocity scaling factors are determined by kinematics as the implied distance scaling must be consistent with the intended simulations. Figure 6.7 (a) shows a two dimensional slice of the Reference Turbulence after dimensionalizing and scaling the data at a fixed time.

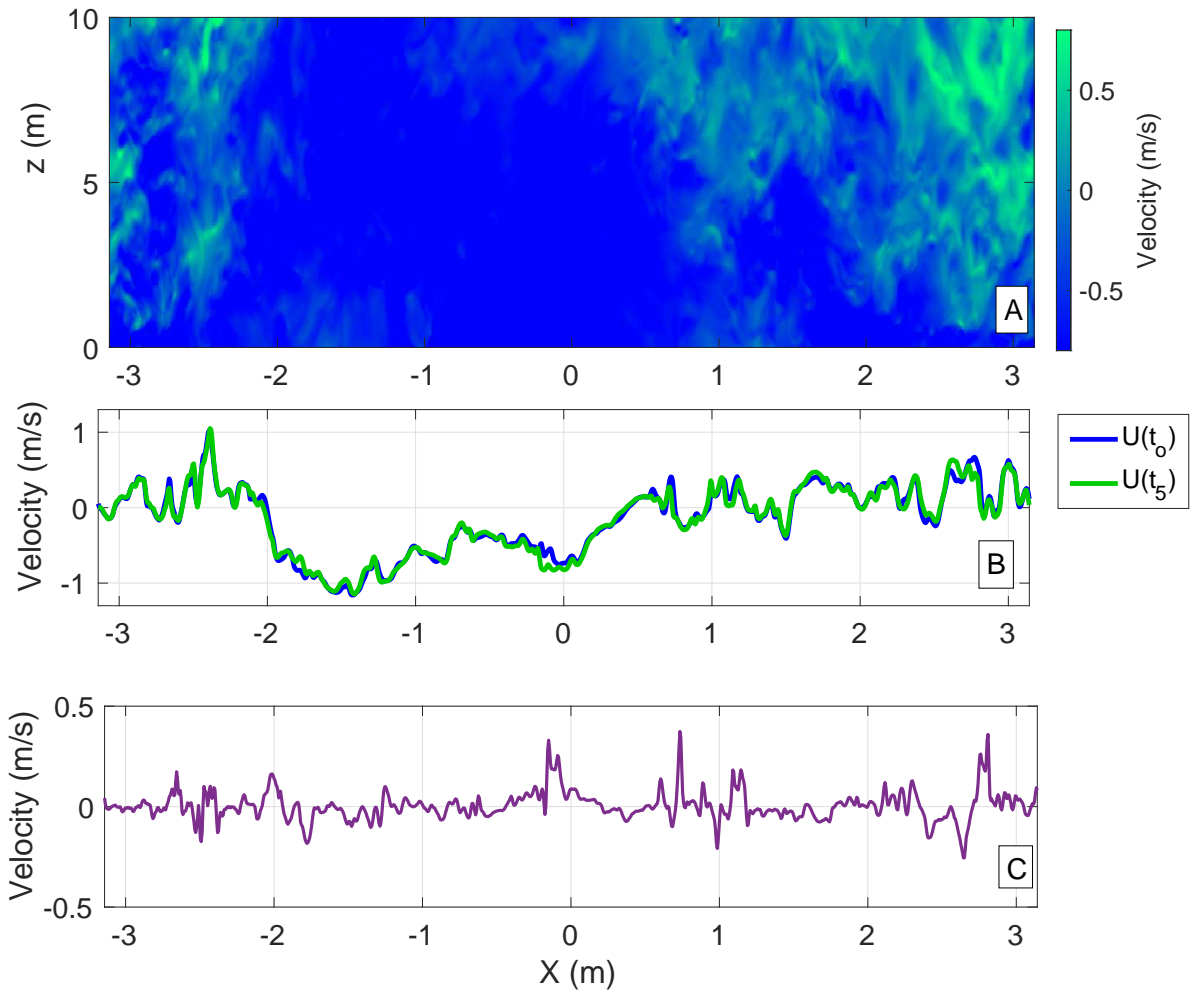


Figure 6.7: Scaled Reference Turbulence (a) and time evolving velocities (b) at a fixed y and z position at an initial time. Figure (c) shows The difference between the velocity profiles  $U(t_0)$  and  $U(t_5)$

The acoustic model confirms the scaling of the Reference Turbulence is physically reasonable for the planned simulation by checking that the boundary limits of the model are less than or equal to those of the scaled turbulence. For example, the maximum depth associated with the Reference Turbulence must be greater than or equal to the acoustic models vertical boundary limit to ensure sufficient spatial resolution. Additionally, the acoustic model checks that the planned simulated collection time is achievable after applying the temporal scaling factor to the turbulence. These checks confirm the Reference Turbulence has adequate spatial and temporal resolution for the acoustic model run. Figure 6.7 (b) shows velocity along the periodic direction ( X ) at an initial time (shown in blue) and compared to velocity data at the same place but at a different time (shown in green). Comparison between velocity series demonstrated the evolution of time in the dataset. Figure 6.7 (c) shows the difference between the velocity profiles and highlights the change in velocity between time steps.

It is important to note that the model allows for some turbulent properties such as kinematic viscosity to be scaled to artificially large values. The kinematic viscosity :

$$\nu = \frac{\mu}{\rho} \quad , \quad (6.7)$$

is directly related to the dynamic viscosity (  $\mu$  ) and the density. The kinematic viscosity is therefore indirectly related to the spatial scaling of the Reference Turbulence through the density ( $\rho = \text{mass} / \text{volume}$ ), for instance, increasing the spatial extend of turbulence will result in a decrease in kinematic viscosity. This indirect scaling of viscosity to artificially large values is a consequence of guaranteeing adequate data resolution and will be considered when interpretation acoustic simulation results

### 6.3.3 Evolving Turbulence Domain with Time

The model of acoustic backscatter is populated with randomly positioned discrete targets that must collectively move and represent the motion of turbulence, Figure 5.1 provides a schematic of the model. The acoustic backscatter of the system is calculated from the moving targets and depends on their movement in time and the frequency content (see Section 5). The Reference Turbulence was integrated into the acoustic backscatter model after being dimensionalized and scaled to simulate a velocity field consistent with the expected observations. There are two items that must be considered for the integration of turbulence data into the model of acoustic backscatter. The first consideration is the Reynolds decomposition (Equation 2.4), where the turbulent velocity input represents the turbulent fluctuations ( $u'_i, u'_j, u'_k$ ) and a mean velocity ( $\bar{u}_i$ ) in the horizontal direction must be added to the input turbulence. The mean velocity has been chosen to contribute the net mean velocity characteristic of tidal flows.

Updating the position of the discrete acoustic targets using the turbulent velocity ( $u'_i, u'_j, u'_k$ ) from the Reference Turbulence is the second important consideration. The acoustic targets are Lagrangian while the Reference Turbulence is Eulerian, meaning that the turbulence does not have velocity values for the exact locations of the particles. Acoustic target velocities are assigned by minimizing the difference between the position of the targets ( $X_{\text{ith}}, Y_{\text{ith}}, Z_{\text{ith}}$ ) and the positions of the turbulent input data ( $X_{\text{JH}}, Y_{\text{JH}}, Z_{\text{JH}}$ ), this is an application of nearest neighbours. A schematic of how the location of the acoustic targets is updated in time is shown in Figure 6.8.

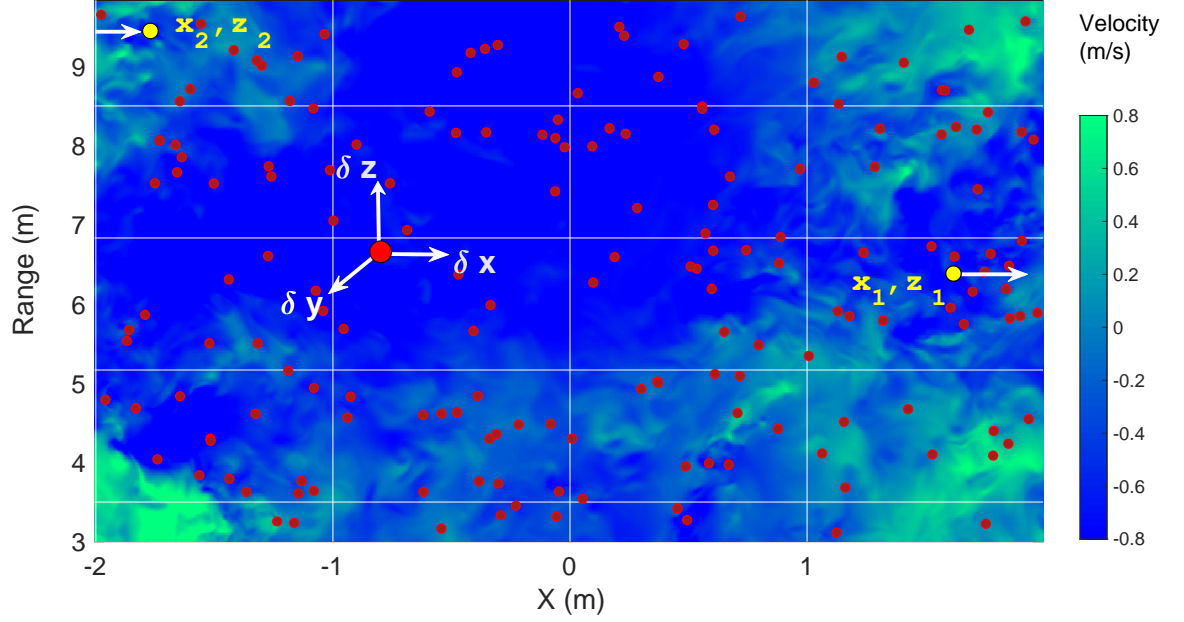


Figure 6.8: Locations of the acoustic targets (red dots) are updated with prescribed references turbulence (shades of blue / green). Particles (yellow dot) that move outside the model boundaries are wrapped back into the opposite side of the domain

The position of each  $i^{th}$  target is updated by a factor of  $\delta x_i, \delta y_i, \delta z_i$  as time evolves:

$$\delta x_i = \left( u'_i + \overline{u}_i \right) \delta t , \quad (6.8a)$$

$$\delta y_i = \left( u'_j + \overline{u}_j \right) \delta t \quad \text{where } \overline{u}_j = 0 , \quad (6.8b)$$

$$\delta z_i = \left( u'_k + \overline{u}_k \right) \delta t \quad \text{where } \overline{u}_k = 0 , \quad (6.8c)$$

The acoustic model updates the target location at the same frequency as the simulated sonar transmit sound. The bounds of the turbulence dataset have to be larger than the bounds of the acoustic model domain. This boundary requirement arises as turbulent data is needed anywhere the simulated acoustic beam is measuring. If an acoustic target is advected outside the model domain, it is wrapped around the horizontal  $x$  axis and randomized in the other two dimensions, the yellow dots on Figure 6.8 provide an example.

To confirm that the process of advecting Reference Turbulence through the sonar model preserved the required turbulence characteristics an Eulerian fluid flow experiment was conducted. A conceptual chain or mesh box shown in Figure 6.9 (a)

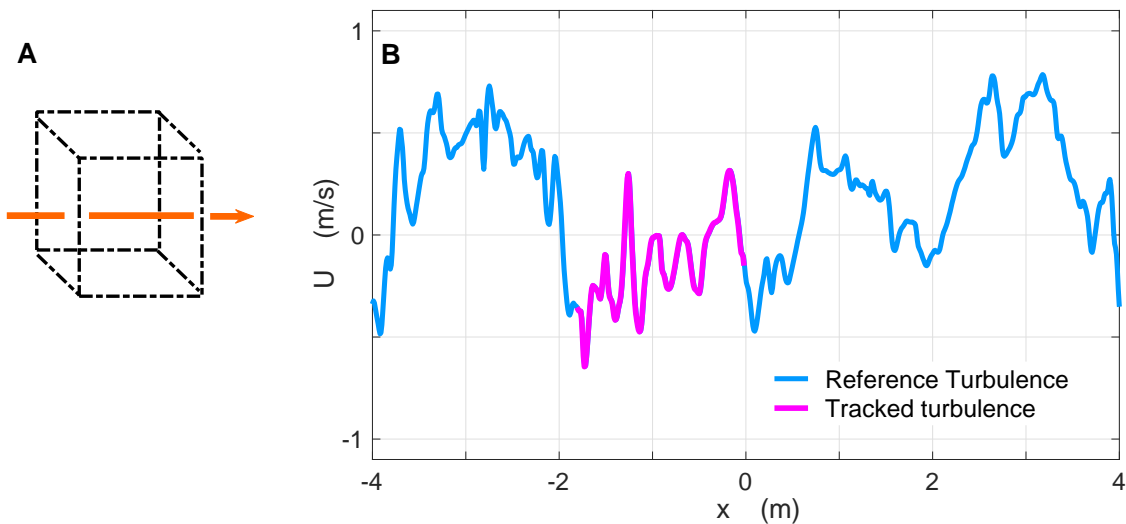


Figure 6.9: Schematic the mesh box placed in the model domain for the Eulerian fluid experiment (a). Experiment results including the tracked velocity compared the expected result, the Reference Turbulence (b).

was placed in the middle of the acoustic model domain and then the flow into / out of the mesh box was observed. The conceptual mesh box was fixed in position for the duration of the experiment. The velocities that passed through the mesh box were recorded and then compared to expected velocities based on the known turbulent input. The observed turbulent velocities recorded passing through the Eulerian mesh box (Figure 6.9 (b), pink line) match the expected results (blue line). This high similarity between expected turbulence and observed confirms the Reference Turbulence is advected through the acoustic model as expected and demonstrates that the integration of our turbulence into the acoustic model has been successful.

# Chapter 7

## Nortek AD2CP Simulations

### 7.1 Device Configuration

The Nortek Signature 1000 AD2CP is a 1 MHz Doppler current profiler that can operate as a broadband or fully coherent sonar. This device was chosen for simulation as its application to measuring turbulence has been considered in various field studies. In particular, it has been used to collect experimental measurements of turbulence in high flow regions where in-stream tidal turbines could be deployed (McMillan et al., 2016; Horwitz and Hay, 2017; Guerra and Thomson, 2017). AD2CPs have also been used to collect turbulent velocity measurements in near-shore environments and in the surface boundary layer (Shcherbina et al., 2018). A discussion measuring turbulence with Doppler sonar and specific examples utilizing AD2CPs can be found in Section 4.2.

The AD2CP has five beams, one that is vertically orientated and four of which are angled at  $25^\circ$  relative the vertical (Nortek, 2018). Figure 7.1 (a) shows a top-down schematic of the Nortek AD2CP transducer locations, the fifth transducer located at the device center is the vertically oriented beam. In a field application of the instru-

ment, data from the four tilted beams are used together to estimate vertical and horizontal velocities. The fifth vertical beam can independently collect vertical velocity estimates. This study considers observations of vertical velocity and therefore, only the fifth transducer is simulated as the vertical beam is intended for turbulence measurements. By only simulating the vertical transducer the need to convert from beam coordinates to Earth coordinates is eliminated, this also simplifies the post-processing data multiplication.

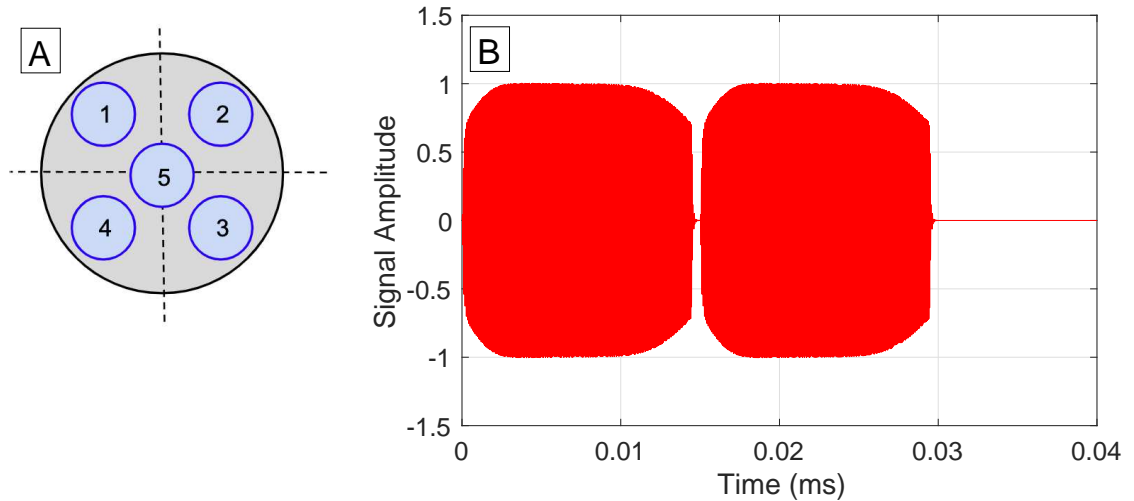


Figure 7.1: A schematic of the Nortek AD2CP transducer locations (a) and the simulated transmit pulse (b) are presented. The simulated instrument was parameterized to match a broadband configuration in McMillan et al. (2016).

The simulated transmit pulse shown in Figure 7.1 (b) corresponds to a broadband signal. A short time delay between pulse pairs is selected to simulate broadband sonar, the time lag between the pulses leading edges is 0.26 ms compared to the pulse length of 0.25 ms. A short time lag is critical for simulating broadband sonar where

a larger time lag is used for a pulse-to-pulse coherent configuration (see Chapter 3.2). The pulses have a frequency chirped going from 750 kHz to 1.25 MHz, corresponding to the carrier frequency plus or minus half the bandwidth, ( $f_o \pm f_{BW}/2$ ). The chirped pulses allows for a wider range of frequency to be transmitted.

The simulated AD2CP operated at a carrier frequency of 1 MHz with a 500 kHz bandwidth and had a transducer radius of 0.015 m. Additional acoustic configuration parameters are listed in Table 7.1 including the sample rate, the sampling frequency, the length of collection and the resulting ambiguity velocity. The definition and importance of these parameters are provided in Chapter 3. This parameterization is based off the McMillan et al. (2016) field experiments (see Table 4.1). The largest anomaly between the model parameterization and McMillan et al. (2016), is a 1.3 Hz difference in the sample rate. Section 7.3.2 will consider the significance of sample rate on the model results.

Carrier Frequency	1 MHz	Bandwidth	500 kHz
Time between Pings	0.15 s	Sample Rate	6.7 Hz
Collection Period	4.5 mins	Ambiguity Velocity	1.47 m/s
Pings per Ensemble	1	Averaged Range Bin Size	0.2 m

Table 7.1: Shows acoustic parameters used in the AD2CP model simulation.

The physical model domain is rectangular and has a volume of  $56 \text{ m}^3$  and is populated with 200,000 independent backscatter targets. The domain spans from  $-2$  to  $2$  m in the x-direction,  $-1$  to  $1$  m in the y-direction and  $3$  to  $10$  m in the z-direction.

The AD2CP is located at the model origin,  $x = 0$ ,  $y = 0$ ,  $z = 0$ . The mean velocity is set to 0.5 m/s in the horizontal x-direction. See Chapter 6.3 for a detailed description of the input turbulence and the model domain.

## 7.2 Simulation Results

The AD2CP model parameterization produced the beam pattern presented in Figure 7.2. The x's on Figure 7.2 show the mid-point sampling positions of the model bins. In this model configuration the mid-point sampling positions appear as a straight vertical line highlighting the beam directivity. The simulated transducer is

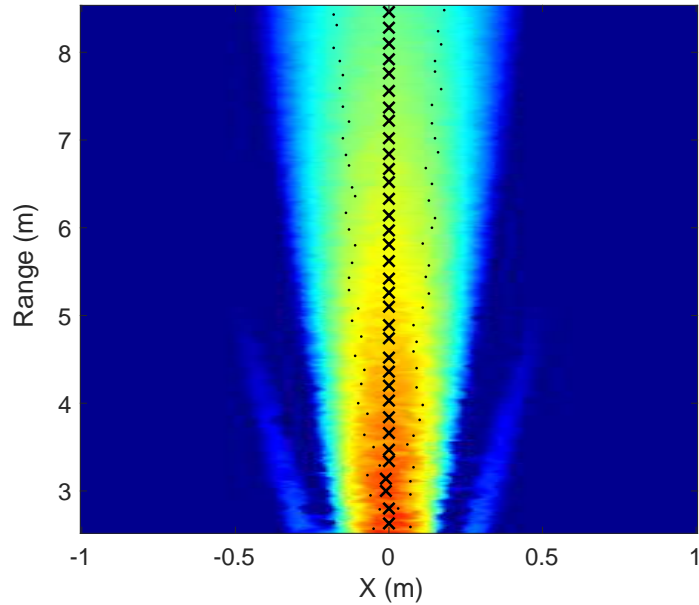


Figure 7.2: AD2CP simulated beam pattern. The warm (cool) colors represent the regions of high (low) scattering. The x's show the midpoints and the black dots show the 3 dB beam width.

located 3 m below the bottom of the model domain at the coordinate systems origin and the device is collecting data within a 7 m range. In-stream tidal generating industry is interested in the turbulent velocity at the turbine hub height ( $\approx 7$  m) motivating the selected vertical model domains limits. In Figure 7.2 the dotted lines on either side of the mid-point sampling location show the 3 dB width of the beam.

The model simulation yields the backscatter amplitude, the phase shift between pulse-pairs and the pulse-pair correlations (see Chapter 3). From these parameters, the values of turbulent velocity can be calculated using Equation 3.6. The simulated acoustic backscatter amplitude is shown in Figure 7.3 (a) and the simulated Doppler

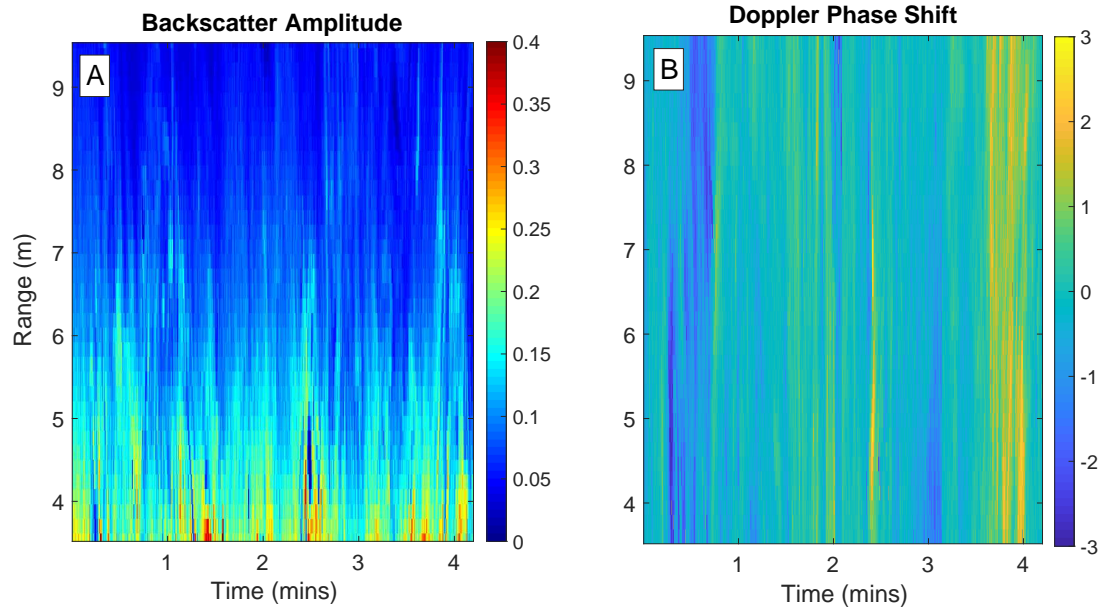


Figure 7.3: The simulated acoustic backscatter amplitude of the AD2CP is shown in (a) warm (cool) colors represent regions with high (low) backscatter contributions. The simulated Doppler phase shift is shown in (b).

phase shift between pulse-pairs is presented in Figure 7.3 (b). The backscatter amplitude is highest close to the transducer highlighting the regions of highest scatter contribution. This result is an expected outcome as sounds will spread spherically as the models volume backscatter is uniform with depth. The data shown in Figure 7.3 (a) and (b) are raw model output and have not undergone post-processing or range bin averaging as is required to achieve velocity estimates.

Phase wrapping is a potential source of error in pulse-to-pulse coherent and broadband sonar operation (see Chapter 3). It was concluded that the effects of wrapping were minimal as jumps were infrequent, occurring less than 0.033 % of the time. Therefore, the AD2CP data presented here has not been corrected for phase wrapping. However, it is acknowledged that in future studies the effects of wrapping should be reconsidered as they may not be negligible in all cases. For instance, if the flow velocities are outside the bounds of the ambiguity velocity (Equation 3.5) then a high percentage of the Doppler sonar data will be effected by phase wrapping.

The expected turbulence measurement is an input into the model simulation and is thereby a known velocity field. These known velocities allow for a direct comparison between the true, Figure 7.4 (a) and measured, Figure 7.4 (b) velocities. The simulated velocities have been range bin and ping averaged to match the specifications given in Table 7.1. The measured result shows broad agreement with the Reference Turbulent data however, the simulation does not resolve the finer details. The Reference Turbulent data was range bin averaged to match that of the simulated measurement and the difference between the two velocity fields is shown in Figure 7.4 (c). The mean velocity difference is  $-0.11 \text{ m/s} \pm 0.26 \text{ m/s}$ , the large standard deviation highlights the variability in the turbulent data.

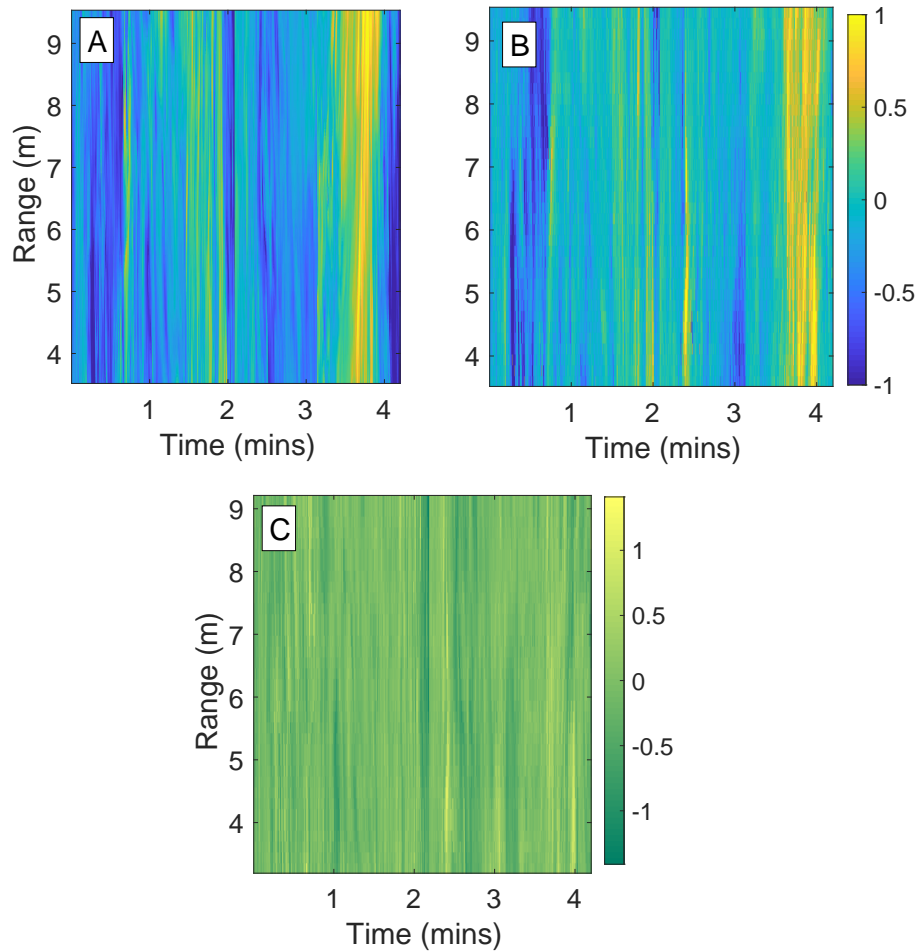


Figure 7.4: The Reference Turbulence (a) and the simulated AD2CP turbulence measurement (b) compared with the difference between true and measured velocity (c). The occurrence where the finer turbulence structures are unresolved by the simulation are highlighted in (c) by shades of dark green and bright yellow.

The broadband correlation can be used as an indicator of the quality of the collected data. The value will be between 0 and 1 and should have a maximum average value of 0.5 (see Chapter 3). Figure 7.5 (a) shows the broadband correlation measured

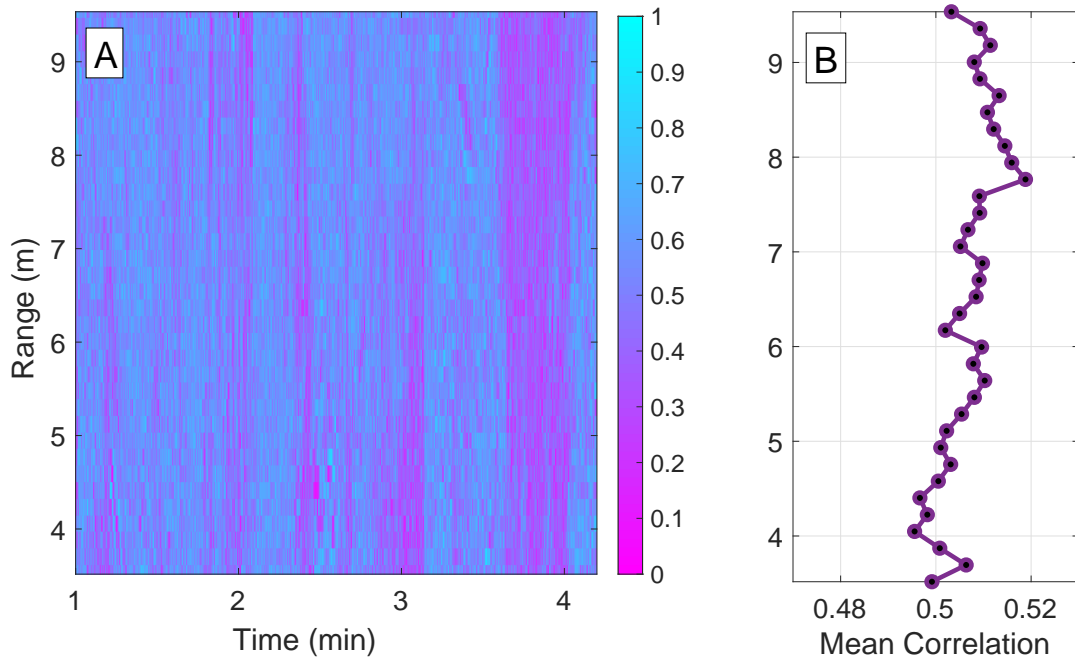


Figure 7.5: Correlation from the simulate AD2CP data

by the AD2CP simulation. Figure 7.5 (b) shows that depth dependant mean correlation value is between 0.50 and 0.52 over depth. This result aligns with the expectation that broadband sonar will produce a correlation value of approximately 0.5, further demonstrating the models ability to reproduce results that are expected in field experiments.

### 7.2.1 Spectral Analysis

A spectral analysis was performed to confirm that the velocity measurements resolve the characteristic properties of the Reference Turbulence. Taylor's Frozen Field Hypothesis was applied to interpret the velocity data. Energy spectra were calculated for each interval of range and the resulting variation in spectral density is

shown in Figure 7.6 (light blue stars). The resulting turbulence spectrums calculated for each range were averaged together to give an overall energy spectrum (Figure 7.6, solid

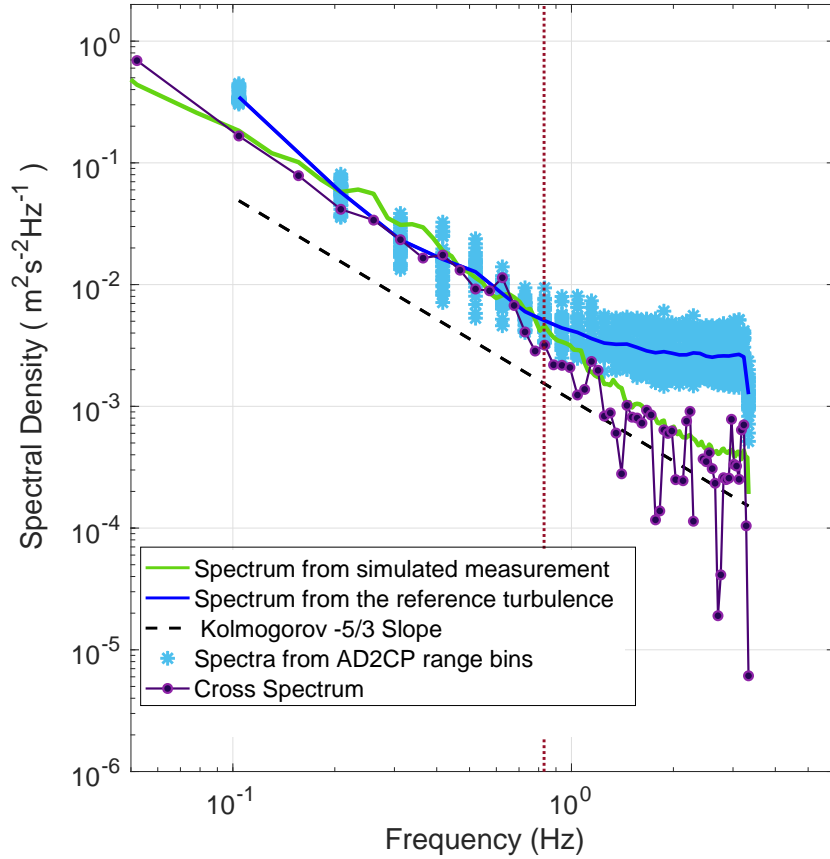


Figure 7.6: Turbulent energy spectrum for the Nortek AD2CP simulations, the turbulent spectrum for each range bin of measured velocity is shown by the light blue stars.

dark blue line). The overall turbulent energy spectrum demonstrates that the AD2CP is able to resolve the turbulent structure at frequencies below 0.83 Hz (red line on

Figure 7.6), corresponding to the inertial subrange. However, at frequencies above 0.83 Hz the measured spectrum flattens into a noise floor, indicating the AD2CP cannot resolve velocity above this cut-off and into the dissipation subrange.

The Reference Turbulence was dimensionalized and scaled to meet the spatial and temporal requirements of the simulation. The transition from inertial subrange to dissipation range in the Reference Turbulence occurs at 1.1 Hz, a consequence of the artificially large kinematic viscosity. The scaled kinematic viscosity used in the AD2CP simulation was  $1.98 \times 10^{-5} \text{ ms}^{-2}$ , which is ten times larger than true kinematic viscosity for water  $\approx 1.85 \times 10^{-6} \text{ ms}^{-2}$ . If the value of viscosity wasn't artificially large, the dissipation range would be absent in the sonar observations as the AD2CP sampling configuration should not be able to observe velocity in the dissipation subrange.

Parseval's Theorem states that the energy density measured in the frequency domain is the same as the energy measured in the time domain. The theorem provides a way to relate the spectral noise floor to the sample variance of the measurements. The location of the noise floor in spectral space,  $S^2$ , has the same units as the scaled variance:

$$S^2 \left[ \frac{m^2}{s^2} \ s \right] = 2 \frac{1}{f_s} \sigma_v^2 \left[ \frac{m^2}{s^2} \ s \right] \quad (7.1)$$

where,  $1/f_s$  is the difference in sample time. In order to preserve power in time as in frequency space the two expressions of Parseval's Theorem must be equal to each-other. Equation 7.1 can be rearranged for the signal variance in term of  $S^2$  and expressed as:

$$\sigma_v^2 = \frac{1}{2} S^2 f_s = S^2 \frac{1}{2\Delta t} \quad \text{where, } \Delta t = \frac{1}{f_s} \quad , \quad (7.2)$$

The Nyquist frequency (  $f_s/2$  ) of the measured turbulence spectrum is equal to 3.3 Hz and the location of the spectral noise floor (  $S^2$  ) is equal to  $2.5 \times 10^{-3} \text{ m}^2\text{s}^{-1} \text{ Hz}^{-1}$ , suggesting a Standard Deviation of  $\approx 0.091 \text{ ms}^{-1}$ . The characteristics of this noise floor were compared to the McMillan et al. (2016) field observations. McMillan et al. (2016) found the AD2CP noise floor to be located at approximately  $2.6 \times 10^{-3} \text{ m}^2\text{s}^{-1}\text{Hz}^{-1}$  and with a 3 Hz Nyquist giving a standard deviation of  $\approx 0.088 \text{ ms}^{-1}$ . The comparison to McMillan et al. (2016) demonstrated the degree to which the model reproduces the limitations of the actual instrument.

The characteristic  $-5/3$  slope (Figure 7.6) determined by Equation 2.8 characterizes the Kolmogorov Energy Spectrum. From the characteristic slope it can be concluded that the true and simulated measurement of turbulence have an energy dissipation rate  $\mathcal{O}(10^{-3}) \text{ Wkg}^{-1}$ . The noise floor in the turbulence spectrum hides a portion of the turbulent information, this can be addressed to some extent by using the cross correlation spectral technique. Applying the cross correlation technique to the AD2CP simulation results will reduce the range resolution. Cross correlation is a measure of the similarity between two continuous adjacent time series and is given by:

$$(F \star G) = \int_{-\infty}^{+\infty} \overline{F(t)} G(t + \Delta t) dt \quad , \quad (7.3)$$

where  $F(t)$  and  $G(t + \Delta t)$  are adjacent time series and  $(F \star G)$  is the cross correlation as a function of time. Figure 7.6 displays the cross-spectrum between two adjacent

range bins in the simulated turbulence data. The resulting spectrum follows the trends of the turbulence spectrum at frequencies below 0.83 Hz demonstrating that at lower frequencies the adjacent spectrums are similar. At higher frequencies the cross spectrum shows a decreased spectral noise floor as the adjacent range bins of measured turbulence data are dissimilar.

## 7.3 Investigating Data Quality

Previous sections of Chapter 7 have discussed attempts to duplicate AD2CP field observations from McMillan et al. (2016) using an acoustic backscatter model. Here, ways to improve data quality will be explored. Section 7.3.1 and Section 7.3.2 will discuss the significance of beam width and sample rate on data quality, respectively.

### 7.3.1 Beam Width Significance

The width of an acoustic beam pattern is controlled by the size of the transducers. The two parameters are inversely related by the following expression:

$$\theta_{3dB} \propto \frac{\lambda}{D} \quad , \quad (7.4)$$

where  $\theta_{3dB}$  is the 3 dB nominal beam width,  $\lambda$  is the wavelength, and  $D$  is the transducer diameter. As the transducer diameter is reduced the width of the acoustic beam will increase. Two additional simulations that differ only from the base AD2CP

case (described in Section 7.1) by the transducer size were completed.

For the narrow beam case, the transducer radius was increased to 30 cm compared to the original 15 cm. The resulting narrow beam pattern can be seen in the bottom right hand corner of Figure 7.7. Decreasing the beam width had no significant

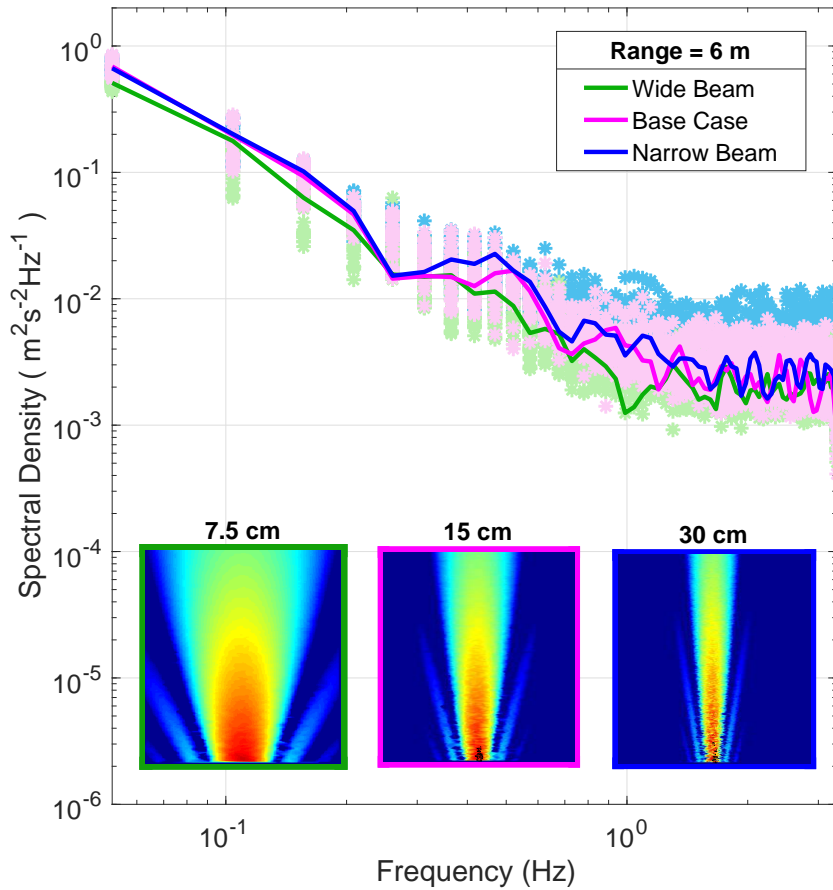


Figure 7.7: Significance of nominal beam width on AD2CP performance. Asterisks represent the energy spectrum for each range bin while solid lines represent the spectrum over range of 6 m.

affect on the turbulent spectra at frequencies below 0.62 Hz. The result suggests that narrowing the acoustic beam offers no advantage in measuring vertical turbulent velocities for the tested turbulent domain.

A comparison of the measured velocity fields from the three simulations (presented in Figure 7.8) suggests that the narrow beam AD2CP is able to observe finer scales

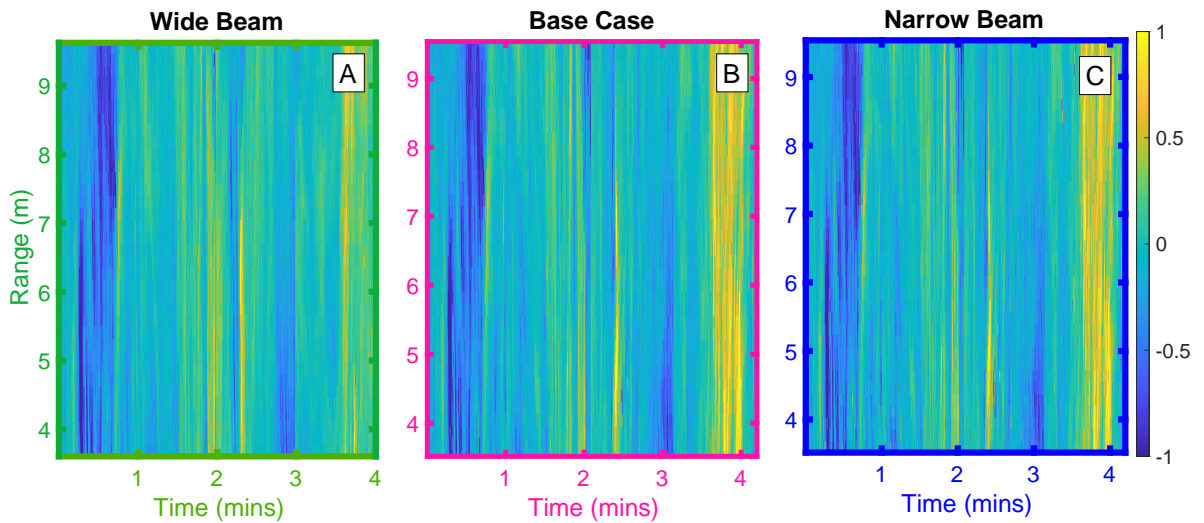


Figure 7.8: Measured velocity for AD2CP simulations for various beam patterns, (a) wide, (b) base and (c) narrow beam

of turbulence. The velocity measurement produced by the wide beam pattern has a smoothing of velocities when compared to either the base or narrow beam pattern. The wide beam pattern produced by reducing the transducer radius to 0.75 cm results in smoothing of turbulence information and produced a spectrum closely match the base case but on average a lower spectral density (Figure 7.7). A decrease in spectral density is observed and indicating less energy in this region this suggesting

a smoothing of important velocity structure. The noise floor starts  $\approx 0.62$  Hz, the same as the narrow beam width simulation. In summary, decreasing the transducer size will not significantly improve the devices ability to resolve turbulence at high frequencies but increasing the transducer size might lead to loss of spatial resolution. The noise floor is shifted by the change in beam pattern.

The velocity measurements can be compared to the Reference Turbulence by considering the difference between the velocities fields, Figure 7.9 shows the anomalies between the simulated measurement and the Reference Turbulence for the wide beam

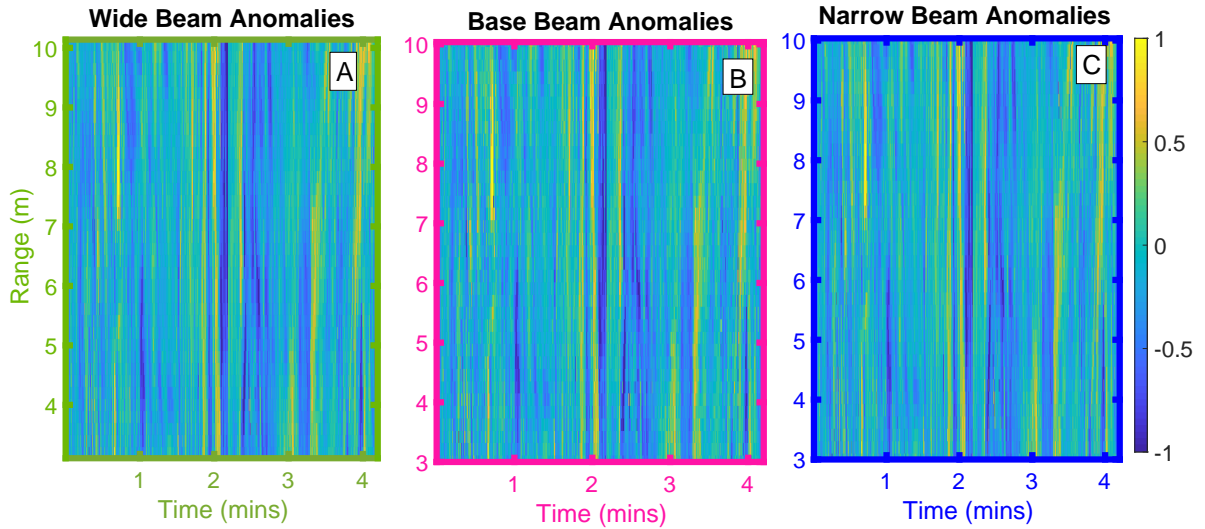


Figure 7.9: Difference between the measured velocity from AD2CP simulations and the Reference Turbulence for various beam patterns, (a) wide, (b) base and (c) narrow beam

(a), base beam (b) and narrow beam (c). The anomalies in all three case are similar, which supports the conclusion that narrowing the beam width may not improve the measurement accuracy.

### 7.3.2 Sample Rate Significance

The instrument sample rate is another potentially important factor in determining sonar performance and considering ways to improve data quality. The sample rate and the time between pulse transmissions are inversely proportional,  $f_{sr} \propto 1/t_p$ . It is hypothesised that the higher the instrument sample rate, the more velocity information collected and the more turbulent structure can be resolved. Here, the sample rate has been considered with respect to the instruments performance in measuring turbulence velocities in high Reynolds number flows. Four additional simulations were completed and compared to the AD2CP base case (Section 7.1) which transmitted pings at a rate of 6.7 Hz.

The turbulent spectra of the four independent simulations are compare in Figure 7.10. The sample rates of these simulations are 3.0 Hz, 4.7 Hz, 6.7 Hz, and 11 Hz. The configurations of these simulations are identical aside from the rate of which the sonar samples. the Nyquist frequency ( $f_s/2$ ) increases as the sample rate increases. A more interesting observation, is that the location of the noise floor qualitatively appears to be related to the sample rate; suggesting that the higher the sample rate the lower the spectral noise floor. This shift in noise floor with increased sample rate could reduced aliasing of high frequency velocities in the data. Increasing the rate of sample should theoretically reduce the noise by allowing for more averaging during the post-processing. In this experiment, the reference turbulence has frequency information that is outside the Nyquist frequency of our simulated sonar and therefore, cannot be resolved.

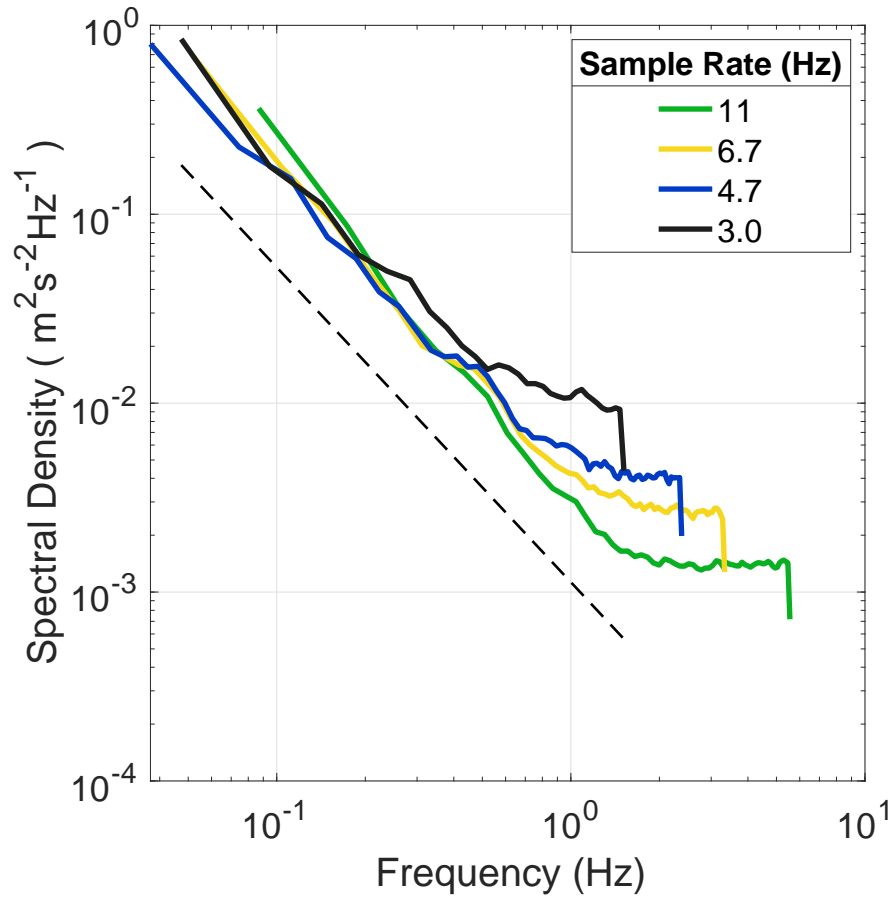


Figure 7.10: The significance of the sample rate is considered by comparing four simulations with different sample rates. The grey dashed line is the  $-5/3$  Kolmogorov slope.

The Nyquist frequencies and spectral noise floor locations with associated uncertainties can be determined from Figure 7.10 using Equation 7.2. Table 7.2 shows that as the sample rate increases the locations of the spectral noise floor decreases, however; the Nyquist frequency increases. Therefore, the resulting standard deviation in vertical velocity is not heavily influenced by the change in sample rate, a slight increase in velocity variance with decreased sample rate is observed.

<b>Sample Rate (Hz)</b>	<b>Noise Floor (<math>\text{m}^2\text{s}^{-1}\text{Hz}^{-1}</math>)</b>	<b>Nyquist Frequency (Hz)</b>	<b>Standard Deviation (<math>\text{ms}^{-1}</math>)</b>
11	0.0014	5.6	0.089
6.7	0.0025	3.3	0.091
4.7	0.0042	2.4	0.10
3.0	0.011	1.5	0.13

Table 7.2: Table of spectral noise floors and Nyquist frequencies for sample rate simulations.

The largest anomaly between the AD2CP model configuration described in Section 7.1 and McMillan et al. (2016) is a 1.3 Hz difference in the sample rate. Based on the influence of sample rate on sonar performance described above, it is predicted that the 8 Hz sample rate used by McMillan et al. (2016) will fall in between the first two entries of Table 7.2. From the McMillan et al. (2016) field study a velocity standard deviation 0.088 m/s was estimated (see Section 7.2) which closely matches are prediction.

# Chapter 8

## Workhorse ADCP Simulation

### 8.1 Device Configuration

Simulation results from an acoustic model configuration that represents the Workhorse 600 kHz ADCP are presented in this Chapter. The model configuration parameters (see Table 8.1) were chosen to replicate those used in McMillan et al. (2016). The modelled sonar operated at a carrier frequency of 500 kHz with a 250 kHz bandwidth. The 100 kHz difference between the carrier frequency of the physical

Carrier Frequency	500 kHz	Bandwidth	250 kHz
Time between Pings	0.69 s	Sample Rate	1.45 Hz
Collection Period	7.5 mins	Ambiguity Velocity	1.94 m/s
Pings per Ensemble	1	Averaged Range Bin Size	0.25 m

Table 8.1: Simulated ADCP acoustic model configuration.

device used in McMillan et al. (2016) and model configuration is due to the limits in the signal processing subroutines implemented in the model. The digital demodulation method (see Chapter 6), requires that the rate of decimation is an integer value. The integer requirement could only be achieved by reducing the carrier frequency to 500 kHz, as the rate of decimation is related to the re-sampling frequency and therefore also by the instruments carrier frequency (see Equation 6.6).

The physical instrument has four beams in a convex geometry with each beam at an angle of  $20^\circ$  relative to the vertical (RDI, 2013). Figure 8.1 (a) shows the transducer geometry. The instrument has been modelled as a single vertical transducer to

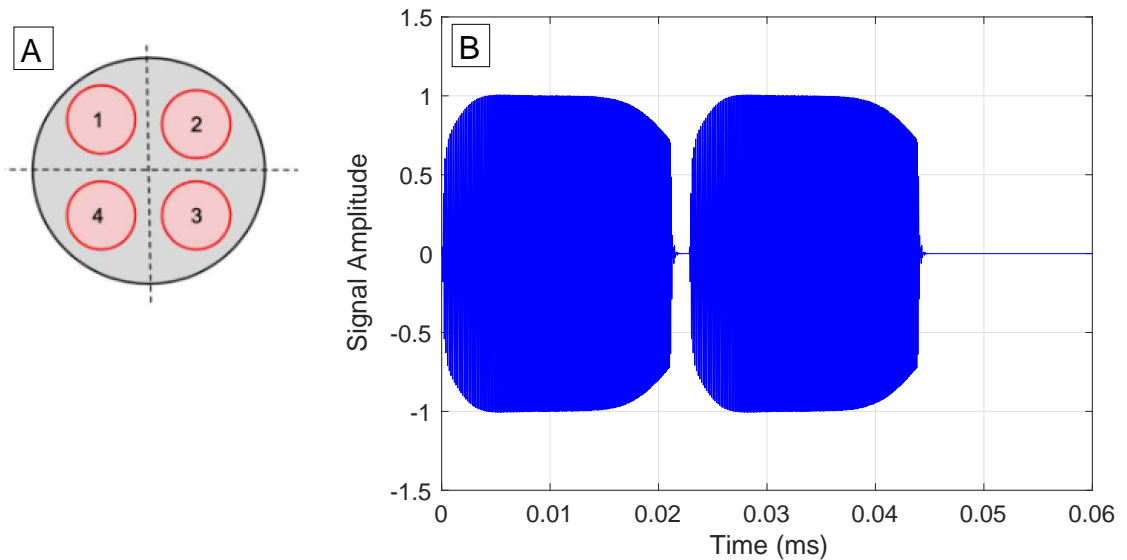


Figure 8.1: Schematic of Workhorse ADCP transducer geometry (a) and the simulated transmit pulse (b).

avoid multiple beam velocity conversions during post-processing, this is permissible

as only one component of velocity is being simulated. This simplification to the simulation is the same as was applied to the AD2CP simulation as described in Section 7.1. The simulated ADCP is a broadband Doppler sonar (see Section 3.2 for details) that has been configured to emit a pulse-pair with an equivalent pulse length of 0.35 ms every 0.69 s and has a pulse-pair at a lag of 0.38 ms. The transmit pulse is shown in Figure 8.1 (b) and has a frequency sweep from 250 kHz to 750 kHz.

The physical model domain has a volume of 56 m<sup>3</sup> and is populated with 100,000 independent backscatter targets. The simulated transducer is positioned 3 m below the model domain at the model origin, ( $x = 0$ ,  $y = 0$ ,  $z = 0$ ) looking upwards and measuring vertical velocities. The simulation profiles approximately 7 m range to a maximum range of 10 m from the transducer. The experiment aims to consider vertical velocity measurements in regions where the flow is highly dynamic, as did the AD2CP simulations described in Chapter 7. The simulation has a mean flow of 0.5 m/s in the horizontal x-direction.

## 8.2 Simulation Results

The Doppler sonar, as previously stated, is positioned 3 m below the model domain at the center of the horizontal coordinate axis and orientated vertically. The simulated transducers had a radius of 2.5 cm, the resulting beam pattern is shown in Figure 8.2, the regions of highest scattering are within the 3 dB beam width and the midpoints of the simulated beam form a vertical line at the horizontal origin.

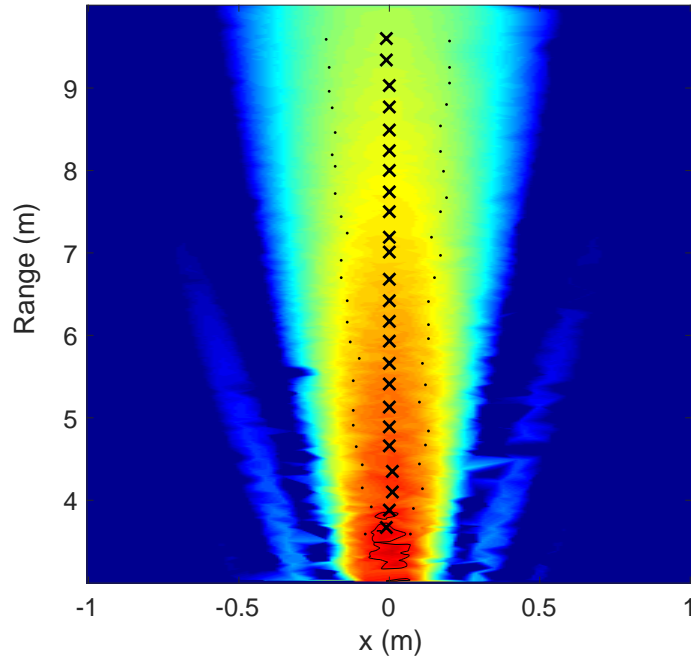


Figure 8.2: ADCP Workhorse simulated beam pattern, warmer (cool) colors show the regions of high (low) scattered concentration. Black x's represent the location of the midpoints and the black dots represent the 3 dB beam width.

As in the AD2CP case (Chapter 7), the simulation produces a measurement of the signal amplitude, Doppler phase shift and pulse-pair correlations. In regions close to the transducer higher values of acoustic backscatter were recorded while the backscatter contributions decreases with increased distance from the transducer, see Figure 8.3 (a). The measured Doppler phase shift is shown in Figure 8.3 (b), recall phase shift is a proxy of velocity (Equation 3.6). The phase wraps or jumps were shown to be minimal, occurring in less than 0.11 % of the data. Phase wrapping is not corrected for in the simulated data due to its low percentage of occurrences.

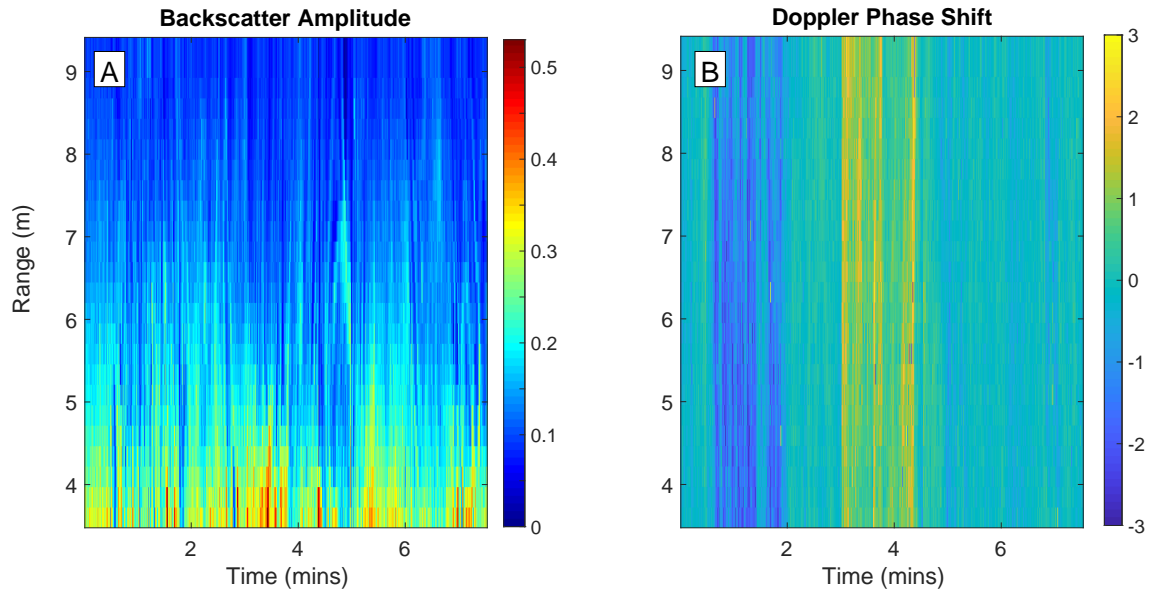


Figure 8.3: The simulated ADCP signal amplitude (a) and the measured Doppler phase shift (b).

The Reference Turbulence and the simulated ADCP measurement of turbulent velocity is given in Figure 8.4 (a) and (b), respectively. The measured vertical turbulence has 0.25 m range bin to resemble the configuration used in McMillan et al. (2016). A comparison between Figures (a) and (b) suggests that the simulated velocity measurements are in broad agreement with the expectation as both Figures have same structural pattern. This broad agreement between the simulation results and expectation (ie. Reference Turbulence) suggest that the ADCP is able to resolve the vertical turbulent velocities. Figure 8.4 (c) highlights the velocity anomalies between the true and measured results. The mean velocity difference is 0.046 m/s and standard deviation of 0.37 m/s, the large standard deviations from the mean indicate the data has a level of variability. A comparison between Figure 7.4 and Figure 8.4 suggests that the ADCP does not perform as well as the AD2CP instrument in re-

solving turbulent structure.

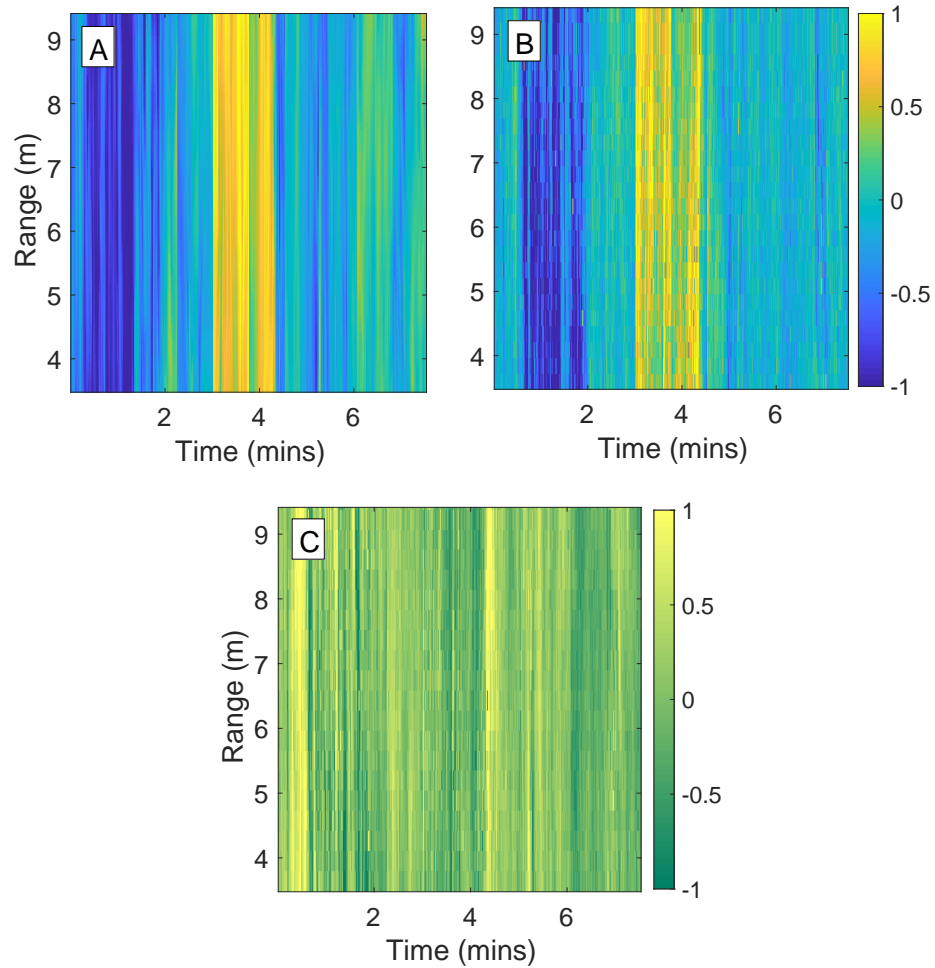


Figure 8.4: Comparison between the Reference Turbulent velocity field (a) and the simulated ADCP vertical velocities observations (b). Figure (c) shows the anomalies between Reference Turbulence and measured velocity.

As in Chapter 7, the correlation can be used to assess the quality of measured turbulence using Doppler sonar (Zedel, 2014). The ADCP pulse-pair correlation shown in Figure 8.5 (a) is an indicator of the quality of the collected data. The correlation

averaged over time per range bin is shown in Figure 8.5 (b). Recall, that

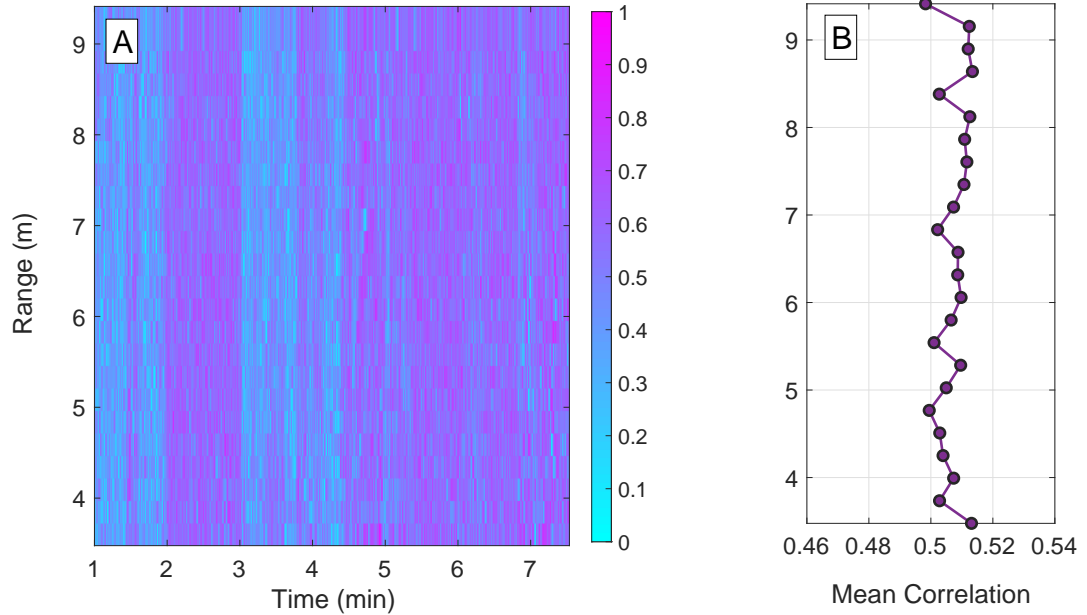


Figure 8.5: ADCP Correlation over time is presented in (a), shades of pink (blue) represent strong (weak) correlation, (b) shows the correlation for each range averaged over time.

values will be between 0 and 1, where the closer the value is to 1 the higher the quality of the data (Chapter 3). The mean value of correlation for the range bins see Figure 8.5 (b)) are between 0.50 and 0.51, while the expected correlation for a broadband configuration is 0.5 which supports that the simulation is performing as expected.

### 8.2.1 Spectral Analysis

The accuracy of the simulation is evaluated using spectral estimations and compared compared to the McMillan et al. (2016) experimental studies. A turbulence spectrum (Figure 8.6) for the ADCP model results is calculated by applying the Taylor’s frozen field hypothesis. The spectrum shows that the measured velocities have the characteristic Kolmogorov slope which is indicative of turbulence energies within the inertial sub-range. The energy spectrum calculated from the forced isotropic turbulence input is indicated by the green line in Figure 8.6. The true and measurement turbulence (blue line) have an energy dissipation rate  $\mathcal{O}(10^{-3}) \text{ Wkg}^{-1}$  based on Equation 2.8 and the characteristic slope grey dashed line in Figure 8.6).

The true or input turbulence spectrum starts to transition from inertial subrange to dissipation subrange as indicated by the slope increasing below that of the  $-5/3$  inertial subrange. This transition is not capture by the ADCP simulation as a consequence of the an artificially large kinematic viscosity. The scaled kinematic viscosity used in the AD2CP simulation was  $9.12 \times 10^{-5} \text{ ms}^{-2}$ , which is fifty times larger that the unscaled kinematic value  $\approx 1.85 \times 10^{-6} \text{ ms}^{-2}$ . At frequencies below 0.25 Hz (red line on Figure 8.6) the simulation is able to resolve turbulent characteristics, however; above the 0.25 Hz cut-off, the turbulent spectrum flattens into a noise floor. Applying the cross correlation technique to the simulation results will reduce the range resolution. The averaged cross-spectrum of the measured ADCP turbulence (purple line) is presented in Figure 8.6. The cross-spectrum suggests that at lower frequencies the adjacent range bins are similar and indicates that the range bins are dissimilar at high frequencies.

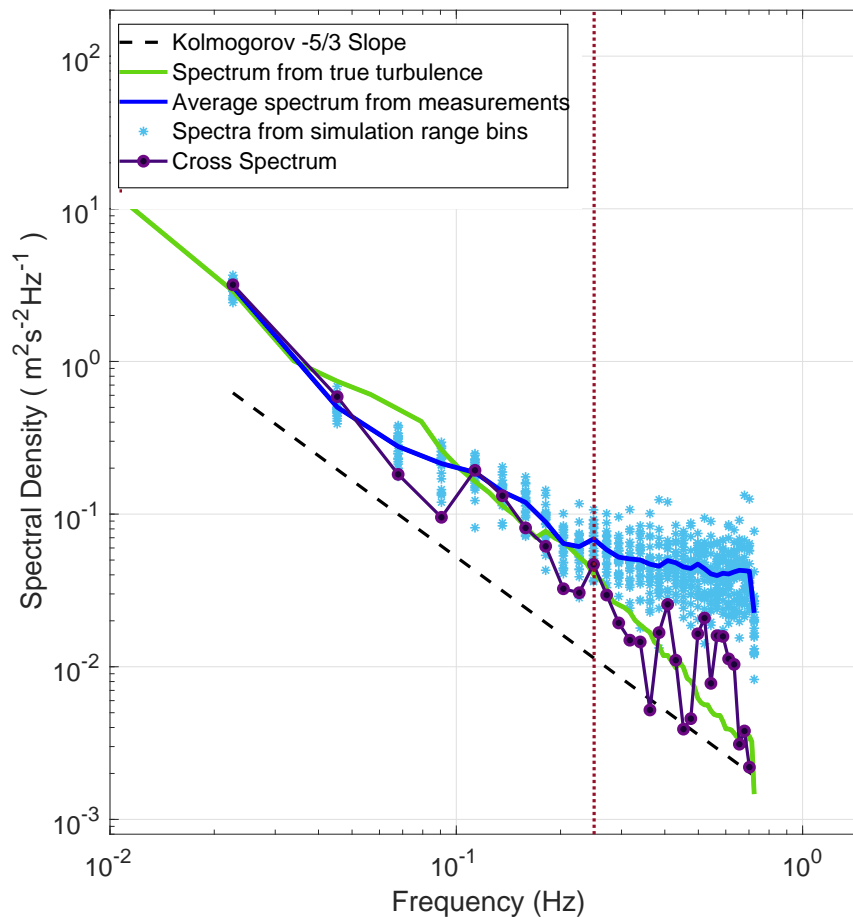


Figure 8.6: Displays the energy spectrum calculated from each ADCP range bin (light blue stars), the energy spectrum averaged over the range bins (dark blue line) and the spectrum from the turbulence input field (green line).

The energy spectrum calculated from the simulated measurement (dark blue line) has a noise floor and demonstrates that the ADCP is unable to resolve turbulence at high frequencies. The noise floor seen in Figure 8.6 is located at approximately  $0.0039 \text{ m}^2\text{s}^{-2}\text{Hz}^{-1}$  and the Nyquist frequency of the system is 0.72 Hz. Applying these

numbers to Parseval's Theorem (Equation 7.2) yields the standard deviation of the time series velocity to be 0.053 m/s. The ADCP observations McMillan et al. (2016) collected had a velocity standard deviation of 0.047 m/s (McMillan et al., 2016).

# Chapter 9

## Summary of Results

An understanding of hydrodynamical flows is essential for a range of ocean applications. The accurate measurement of turbulence in dynamic flows is a topic of particular interest to the tidal industry. In-stream tidal turbines are a reliable source for energy generation that have been used across the globe (Cho et al., 2012; Merlin et al., 1982; Probert, 2011), efforts to implement these systems are ongoing in the Bay of Fundy, Canada. Measurements of turbulence are needed when establishing loading forces on marine structures and estimating the potential for energy generation in a given area. Regions of ocean where in-stream tidal turbines are deployed are turbulent and have high current speeds, these properties present challenges for collecting turbulent observation. The high current speeds make the positioning of in-situ instruments used for turbulence measurements such as velocimeters and shear probes difficult (see Chapter 4). An attractive alternative to in-situ instruments are ADCPs, these devices can collect data remotely and therefore can be positioned with greater ease. Section 4.3 provides a discussion of the application of ADCPs in measuring turbulence.

The application of ADCPs in measuring turbulence in tidal regions has been tested

in the field; however, we lack a way to directly validate the accuracy of these field measurements. This knowledge gap or difficulty is addressed in this thesis through the use of a 3-dimensional numerical model of acoustic backscatter. The model allows for various Doppler sonar configurations (see Chapter 5) and is governed by Equation 5.1. The model has a three-dimensional rectangular domain that is initialized with randomly placed discrete backscatter targets. The target locations will update according to input flow conditions while maintaining a randomized distribution, see Chapter 6.3 for a detailed description.

## 9.1 Doppler Sonar Performance

This study reports on two broadband Doppler sonar systems, the 1 MHz Nortek AD2CP and the Workhorse 600 kHz ADCP. The ability of these devices to collect accurate velocity measurements in regions of high current speeds such as areas where in-stream tidal turbines are deployed is considered. For the present turbulence study, the model presented by Zedel (2008, 2015) has been modified to (1) include a forced isotropic turbulence dataset (ie. Reference Turbulence), (2) an upgraded signal processing technique and (3) the time dilation needed to simulate Doppler shifts of scattered signals has been validated. A complete description of these model developments is presented in Chapters 6 and 6.3. These modifications to the model allow for broadband Doppler Sonar simulations in flow condition similar to those observed in tidal channels.

The Doppler sonars simulated in this thesis were selected and configured to be consistent with the McMillan et al. (2016) field study, see Table 4.1. A comparison between the McMillan et al. (2016) configurations with the AD2CP and ADCP

simulation (Table 7.1 and 8.1, respectively) highlights the similarities and differences between simulations and actual instruments. The AD2CP simulation operates with the same carrier frequency and bandwidth, however, the simulation sample rate is 1.3 Hz lower than was used in McMillan et al. (2016). The ADCP simulation was configured with a carrier frequency 100 kHz lower than the 600 kHz Workhorse used in the McMillan et al. (2016), the sample rate used in the simulation is different from the field study by a minimal 0.04 Hz. A detailed description of the AD2CP and ADCP simulation configurations can be found in Section 7.1 and Section 8.1, respectively.

The simulation results found that the AD2CP produces higher accuracy measurements compared to the ADCP sonar (Section 7.2 and Section 8.2). The AD2CP operates at a higher carrier frequency and with a larger bandwidth than the ADCP. The higher frequency instrument also pings or samples the model domain at a much higher rate, over four times the sample rate of the ADCP. These AD2CP properties namely the high carrier frequency, larger bandwidth and faster sample rate allow the device to collect higher resolution information compared to the ADCP. This effect can be seen by comparing the resolution of velocity measurements in Figure 8.4 with Figure 7.4.

The Doppler sonars ability to measure turbulent velocities can be considered using spectral analysis. Kolmogorov (1941) theory predicts that turbulent velocities in spectral space will exhibit a characteristic slope of  $-5/3$ . Converting from physical space to spectral space can be achieved by performing a Fourier decomposition. The AD2CP turbulence spectrum is given in Figure 7.6 and shows that the AD2CP is able to resolve turbulence and exhibits the expected Kolmogorov slope in the inertial

sub-range. Figure 7.6 also shows that at high frequencies the AD2CP is unable to resolve turbulent velocities and a noise floor is present.

McMillan et al. (2016) used an AD2CP to experimentally collect turbulence measurements in tidal regions. The McMillan et al. (2016) yields similar results to our simulation, they observed that the AD2CP was able to resolve turbulence at low frequency. An application of Parseval's theorem (as explained in Chapter 7) to the results of McMillan et al. (2016) yields a velocity standard deviations similar to the values achieved in this study, McMillan et al. (2016) calculates an AD2CP velocity standard deviation of 0.088 m/s and the simulations yield a standard deviation of 0.091 m/s. The comparison to McMillan et al. (2016) allows us to conclude that our model simulations compare well with experimentally achieved results which validate both the sets of experimental and theoretical experiments.

The simulated ADCP results can also be considered in spectral space and are given in Figure 8.6. The Figure shows evidence that the ADCP is able to resolve turbulence at low frequencies and exhibits the expected Kolmogorov slope in the inertial sub-range. It also shows that regions of high frequency are unresolvable. The ADCP, as discussed above, yields lower resolution results compared to the AD2CP. These lower resolutions results also effect the turbulent spectrum making the noise floor more pronounced than for the high resolution device providing further evidence to suggest that the AD2CP is a better tool for resolving turbulent velocities.

The experimental study conducted by McMillan et al. (2016) tests the performance of the Workhorse 600 kHz ADCP in a tidal channel off the coast of Nova Scotia. The achieved results align well with our simulations results. Both their experimental re-

sults and our theoretical results concluded that ADCP was able to resolve turbulence at lower frequencies but failed to measure higher frequency turbulence. A comparison of standard deviation between the experimental study and the model results provides evidence for this statement, an ADCP velocity standard deviation of 0.047 m/s can be estimated from McMillan et al. (2016) while our simulations yield a standard deviation of 0.053 m/s.

Chapter 7.3.1 and 7.3.2 consider the significance of beam width and sample rate, respectively on the AD2CP's ability to resolve turbulence. These data quality tests were conducted for the AD2CP as previous tests suggest it performs better than the lower frequency ADCP. It was concluded that the radius of the transducer and the corresponding acoustic beam width have no visible effect on the location of the spectral noise floor. Four independent simulations consider the significance of the sample rate on the AD2CP performance. The experiment results concluded that the Nyquist frequency and the location of the noise floor were both influenced by the variations in sample rate. As the sample rate increases the Nyquist frequency increases and the noise floor decreases resulting in minimal effect on the standard deviation of velocity measurements.

The main results from this research include:

- (1) The AD2CP has a higher carrier frequency and profile sample rate which allows the device to collect high resolution turbulence measurements compared to the ADCP.
- (2) Simulations produced results consistent with field research, both simulations had velocity standard deviations that closely matched that observed in McMillan et al.

(2016). The AD2CP simulation produced standard deviations with  $\pm 0.003$  m/s of that McMillan et al. (2016) while the ADCP simulation found standard deviations with  $\pm 0.006$  m/s.

(3) Adjusting the beam width has no effect on the spectral noise floor but increasing the beam width may lead to a smoothing of turbulence at low frequencies.

(4) Increasing the sample rate will lead to a decrease in the location of the spectral noise floor, however, there will be a minimal influence on the velocity standard deviations as the Nyquist frequency will increase.

## 9.2 Current & Future Research

The effect of phase wrapping on the velocity measurements and the application of post-processing correction methods were not considered in this thesis but could be investigated in future work. This extension to the study would build on the work of Shcherbina et al. (2018) and would consider methods such as the Multi-correlation Pulse Coherent Extended Velocity Range (MCPC EVR) method in reducing Doppler noise of turbulent measurements. A description of Shcherbina et al. (2018) is given in Section 4.3. This extension to the study would include a comparison of the phase wrapping correction method on simulated results with the corrected experimental data. The effect of incorporating multiple beams in the correct beam orientation could also be considered.

Another avenue of research could be estimating the energy dissipation rate directly using techniques such as structure function estimators. This research initiative

would build off of McMillan and Hay (2017) who compared techniques for directly estimated the rates of turbulent energy dissipation in high flow tidal channels. Both simulated Doppler data and experimental data would be used to consider (1) the ability of various sonar configurations in estimating the energy dissipation rate directly and (2) to consider the estimation methods best applied to turbulent observations collected with Doppler sonar.

To achieve higher quality simulation results and a wider range of analysis options the model could be further developed to use a fluid dynamics model that includes factors such as ebb and flow of tides or tidal channel geometry. A fluid dynamics model developed to represent tidal regions would allow for the kinematic viscosity to be representative of water while maintaining adequate spatial and temporal resolution, as scaling of the input turbulence would not be required (see Chapter 6.3). These model developments would allow for more advanced studies and more involved comparisons with field results. It is also predicted that using turbulent data from a tidal model will improve the comparisons between simulations and Reference Turbulence.

Considering the effects of turbulent measurements using the higher resolution AD2CP in tidal channels where in-stream tidal turbines are operating is another planned research initiative. This study will be achieved by integrating data from a model of water flow in a tidal channel with an operating turbine into the model of acoustic backscatter. This research avenue has application for the tidal industry, as the flow with and without turbines can be considered and thereby, the turbulence generated by the turbine can be considered.

# Appendix

## A.1: Turbulent Energy Spectrum

An example of generating an energy spectrum from time dependent turbulent data is provided to build on the description and application of Kolmogorov theory used in this study. Turbulent velocity data can be converted from physical space into spectral space using a Fourier decomposition technique, known as the Welch method. The Welch method (Equation 9.1) subdivides data into overlapping segments and estimates the power spectral density level (Welch, 1967):

$$\hat{P}(f_N) = \frac{1}{K} \sum_{k=1}^k I_k(f_N) \quad , \quad (9.1)$$

where,  $\hat{P}$  is spectral density estimate,  $K$  number of segments,  $I_k$  segment modified periodograms,  $L$  is length of segment overlap.

$$f_N = \frac{N}{L} \quad \text{where} \quad N = 0, \dots, L/2 \quad (9.2)$$

Segments can overlapping upto 50 % of the segments length.

Consider a subset of the Johns Hopkins Force Isotropic Turbulence Dataset (Lia et al., 2008) that consist of horizontal velocity ( $U$ ) measured a fixed location on the  $Y$  and  $Z$  axis over time ( see Figure 9.1 a). This physical velocity data can be considered

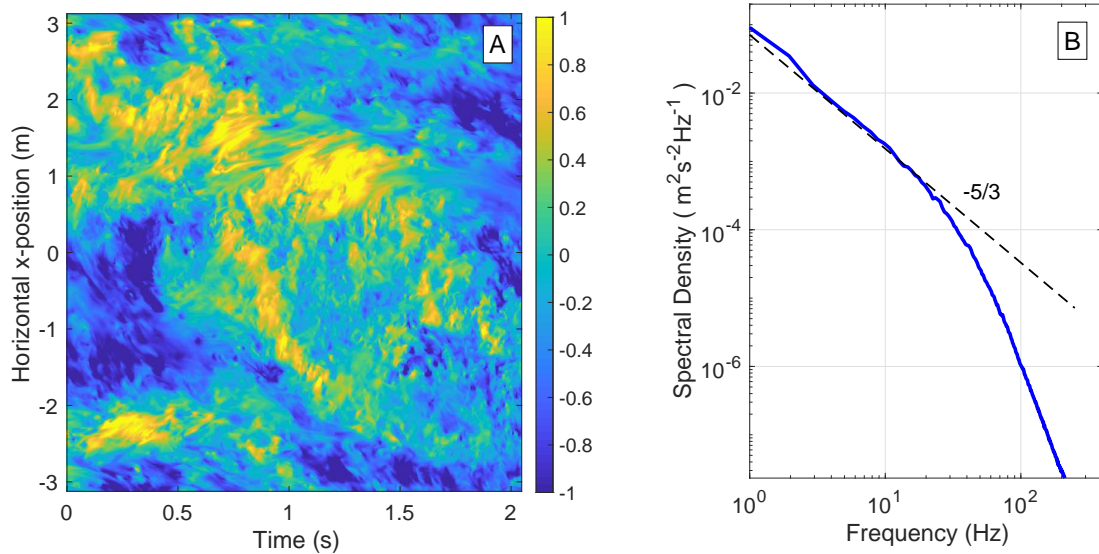


Figure 9.1: Time evolving turbulent velocity data (a) and the corresponding energy spectrum (b).

in spectral space by applying Equation 9.1 to each horizontal range bin of the velocity data. The resulting turbulence spectrums can be averaged together to produce the spectrum in Figure 9.1 (b).

# Bibliography

- A. Baran and D. Infield. Simulating atmospheric turbulence by synthetic realization of time series in relation to power spectra. *Journal of Sound and Vibration*, 180(4): 627–635, December 1995.
- T. Blackmore, L. Myers, and A. Bahaj. Effects of turbulence on tidal turbines: Implications to performance, blade loads, and condition monitoring. *International Journal of Marine Energy*, 14:1–26, 2016.
- D. Bogucki, J. Domaradzki, C. Anderson, H. Wijesekera, J. Zaneveld, and C. Moore. Optical measurement of rate of dissipation of temperature variance due to oceanic turbulence. *Optical Society of America*, 15(12):7224–7230, June 2007.
- B. Brumley, R. Cabrera, K. Deines, and E. Terray. Performance of a broad-band acoustic doppler current profiler. *IEEE Journal of Oceanic Engineering*, 16(4): 402–407, October 1991.
- R Burns, G Eyink, C Meneveau, A Szalay, T Zaki, E Vishiac, R Ravoori, B Devincantis, Zhao Wu, G Lemson, S Chen, M Lee, N Malya, R. D Moser, Pulido J, D Livescu, and Yeung P. K. Johns hopkins turbulence database, July 2018. URL <http://turbulence.pha.jhu.edu>.
- H. Castro, R. Paz, J. Mroginski, and M. Strori. Evaluation of the proper coher-

- ence representation in random flow generator based methods. *Journal of Wind Engineering and Industrial Aerodynamics*, 168:211–227, June 2017.
- R. Charlier and C. Finkl. *Ocean Energy: Tide and Tidal Power*. Springer-Verlag Berlin Heidelberg, av. du Congo 2 1050 Bruxelles Belgium, 2009.
- Y. Cho, J. Lee, and W. Jeong. The construction of a tidal power plant at sihwa lake, korea. *Energy Sources, Part A: Recovery, Utilization and Environmental Effect*, 34(14):1280–1287, May 2012.
- G. Crossley, A. Alexandre, S. Parkinson, A. Day, H. Smith, and D. Ingram. Quantifying uncertainty in acoustic measurements of tidal flows using a 'virtual' doppler current profiler. *Ocean Engineering*, 137:404–416, March 2017.
- J. Dillon. *Maximum A Posteriori Velocity Estimation of Multi-Frequency Coherent Doppler Sonar*. PhD thesis, Memorial University of Newfoundland, St. John's Newfoundland, August 2011.
- J. Dillon, L Zedel, and A Hay. Asymptotic properties of an autocorrelation coefficient for coherent doppler sonar. *Journal of Atmospheric and Oceanic Technology*, 28(7):966–973, July 2011.
- J. Dillon, L. Zedel, and A. Hay. Simultaneous velocity ambiguity resolution and noise suppression for multifrequency coherent doppler sonar. *Journal of Atmospheric and Oceanic Technology*, 29:450 – 463, 2012.
- G. Egbert and R. Ray. Semi-diurnal and diurnal tidal dissipation from topex/poseidon altimetry. *Geophysical Research Letters*, 30(17):9.1–9.4, September 2003.
- A. Elliott. Measurements of turbulence in an abyssal boundary layer. *American Meteorological Society*, 14(11):1779 – 1786, November 1984.

- I. Fer and M. Paskyabi. Autonomous ocean turbulence measurements using shear probes on a moored instrument. *Journal of Atmospheric and Oceanic Technology*, 31(12):474 – 490, 2014.
- L. Gordon. *Acoustics Doppler Current Profiler, Principles of Operation A Practical Primer*. RD Instruments, 9855 Businesspark Ave San Diego, California USA, 2 edition, January 1996.
- M Guerra and J Thomson. Turbulence measurements from five-beam acoustic doppler current profilers. *Journal of Atmospheric and Oceanic Technology*, 34(6):1267–1284, June 2017.
- B Hackett, A Lohrmann, and L. Roed. Bottom current measured with a pulse-to-pulse coherent sonar. *IEEE OCEANS*, 4(87):83–88, 1987.
- J Hare and A. E Hay. Observations of the vertical structure of turbulent oscillatory boundary layers above fixed roughness beds using a prototype wideband coherent doppler profiler: 1. the oscillatory component of the flow. *Journal of Acoustical Society of America*, 143(5):2744–2755, 2018.
- A. . Hay, L. Zedel, S. Nylund, R. Craig, and J. Culina. The vectron: A pulse coherent acoustic doppler system for remote turbulence resolving velocity measurements. In *IEEE/OEC Eleventh Current Waves and Turbulence Measurements Workshop*. St. Petersburg, FL, 2015.
- A. Hay, L Zedel, R Cheel, and J Dillon. Observations of the vertical structure of turbulent oscillatory boundary layers above fixed roughness beds using a prototype wideband coherent doppler profiler: 1. the oscillatory component of the flow. *Journal of Geophysical Research: Oceans*, 117(3):1–20, 2012.

- R. Hodges. *Ambient Noise in Underwater Acoustics*. Number (pp. 127-141). John Wiley and Sons., Chichester, UK, 2010.
- R. Horwitz and A. Hay. Turbulence dissipation rates from horizontal velocity profiles at mid- depth in fast tidal flows. *Renewable Energy*, 114(PA):283–296, 2017.
- S. Huang, Q. Li, and J. W. A general inflow turbulence generator for large eddy simulation. *Journal of Wind Engineering and Industiral Aerodynamics*, 98(10): 600–617, June 2010.
- D. Hurther and U. Lemmin. A correction method for turbulence measurements with a 3d acoustic doppler velocity profiler. *Journal of Atompsheric and Oceanic Technology*, 18(3):446 –458, June 2001.
- N. Jarrin. *Synthetic inflow boundary conditions for the numerical simulations of turbulence*. PhD thesis, University of Manchester, Manchester M60 1QD, United Kingdom, 2008.
- F. Jensen, W. Kuperman, M. Porter, and H. Schmidt. *Computational Ocean Acousitcs*. Springer Science and Business Media Modern Acoustics and Signal Processing, 2 edition, 2011.
- K. Kanov, R. Burns, C. Lalescu, and G. Eyink. The john’s hopkins turbulence database: An open simulation laboratory for turbulence research. *Computing in Science and Engineering*, 17(5):10–17, September 2015.
- R. Karsten. An assessment of the potential of tidal power from minas passage bay of fundy, using three-dimensional models. In *AMSE 2011 30th International Conference on Ocean, Offshore and Artic Engineering*, pages 1–8, Rotterdam, The Netherlands, June 2011. Offshore and Arctic Engineering.

- S. Kioroglou, E. Tragou, and V. Zervakis. Assessing shelf mixing using ctd, adcp and free falling shear probe turbulence data. *Continental Shel Research*, 69:73–87, October 2013.
- J. Knauss. *Introduction to Physical Oceanography*. Englewood Cliffs, N.J. : Prentice-Hall, 1987.
- A. Kolmogorov. The local structure of turbulence in incompressible viscous fluid for very large reynolds numbers. *Proceedings: Mathematical and Physical Sciences*, 434(1890):9–13, September 1941.
- P. Kundu. *Fluid Mechanics*. Academic Press, 525 B Streetm Suite 1900, San Diego, California, 4 edition, 1990.
- U. Lemmin and T. Rolland. Acoustic velocity profiler for laboratory and field studies. *Journal of Hydraulic Engineering*, 123(12):1089–1098, December 1997.
- R. Leonard, P. Combs, and L. Skidmore. Attenuation of sounds in synethtic sea water. *The Journal of the Acoustical Society of America*, 21(1):63, 1949.
- R. Lhermitte and U. Lemmin. Open-channel flow and turbulence measurement by high-resolution doppler sonar. *American Meteorological Society Journal of Atmospheric and Oceanic Technology*, 11(15):1295–1308, October 1994.
- R Lhermitte and R Serafin. Pulse-to-pulse coherent doppler sonar signal processing techniques. *Journal of Atomspheric and Oceanic Technology*, 1(4):293–308, December 1984.
- Y. Li, E. Perlman, M. Wan, Y. Yang, C. Meneveau, R. Bruce, S. Chen, A. Szalay, and G. Eyink. A public turbulence database cluster and applications to study lagrangian evolution of velocity increments in turbulence. *Journal of Turbulence*, 9(9):31, 2008.

- Y. Lia, E. Perlmanb, M. Wana, Y. Yanga, C. Meneveaua, R. B. S. Chena, A. Szalayc, and G. Eyinkd. A public turbulence database cluster and applications to study lagrangian evolution of velocity increments in turbulence. *Journal of Turbulence*, 9(31):1–29, 2008.
- L. Liebermann. Sound propagation in chemically active media. *Physical Review*, 76(10):1520–1524, 1949.
- P. Liu and B. Veitch. Design and optimization for strength and integrity of tidal turbine rotor blades. *Energy*, 46(1):393–404, 2012.
- A. Lohrmann, R. Cabrera, C. Kraus, and M. ASCE. Acoustic-doppler velocimeter (adv) for laboratory use. *Fundamentals and Advancements in Hydraulic Measurements and Experimentation*, (351-365), August 1994.
- A. Lorke and A. Wuest. Application of coherent adcp for turbulence measurements in the bottom boundary layer. *Journal of Atmospheric and Oceanic Technology*, 22:1821 – 1828, November 2005.
- R. Lueck, D. Huang, D. Newman, and J. Box. Turbulence measurement with a moored instrument. *Journal of Atmospheric and Oceanic Technology*, 14(1):143–161, 1997.
- R. Lyons. *Understanding Digital Signal Processing*. Prentice Hall, 3 edition, 2011.
- J. McMillan and A. Hay. Spectral and structure function estimates of turbulence dissipation rates in a high-flow tidal channel using broadband adcps. *Journal of Atmospheric and Oceanic Technology*, 34(1):5 – 20, January 2017.
- J. McMillan, A. Hay, R. Lueck, and F. Wolk. Rates of dissipation of turbulent kinetic energy in a high reynolds number tidal channel. *Journal of Atmospheric and Oceanic Technology*, 33(4):817 – 837, April 2016.

- J. M. McMillan, M. J. Lickley, R. Karsten, and R. Haynes. The potential of tidal power from the bay of fundy. *Society for Industrial and Applied Mathematics*, pages 20–37, January 2018.
- H. Medwin and C. Clay. *Fundamentals of Acoustical Oceanography*. Academic Press, 525 B Street, Suite 1900, San Diego, CA 92101-4495, USA, 1998.
- A. Merlin, P. Sandrin, P. Gres, and M. Hilairet. Arga, the new operation model for the "la rance" tidal power plant. *Power Apparatus and Systems, IEEE Transactions on*, PAS- 101(2):290–204, 1982.
- K. Miller and M. Rochwarger. A covariance approach to spectral moment estimation. *IEEE Transactions on Information Theory*, 18(5):588–596, September 1972.
- L. Mo and R. Cobbold. A unified approach to modeling the backscattered doppler ultrasound from blood. *Biomedical Engineering, IEEE Transactions*, 39(5):450–61, 1992.
- P. Moin and K. Mahesh. Direct numerical simulation: A tool in turbulence research. *Annual Review of Fluid Mechanics*, 30(1):539–578., 1998.
- J. Murray. A theoretical model of linearly filtered reverberation for pulsed active sonar in shallow water. *Journal of Acoustical Society of America*, 136(5):2523–2531, November 2014.
- Nortek. Current profiler signature 1000, 2018. URL [www.nortekgroup.com/export/pdf/Signature1000.pdf](http://www.nortekgroup.com/export/pdf/Signature1000.pdf).
- NS. Nova scotia marine renewable energy strategy. In *DesLibris Documents Collections*. Canadian Electronic Library and Nova Scotia Department of Energy, Halifax, Ns: Nova Scotia Dept of Energy, 2012.

- N. Oakey. Determination of rate of dissipation of turbulent energy from simulations temperature and velocity shear microstructure measurements. *Journal of Physical Oceanography*, 12(3):256–271, 1982.
- T. Osborn. Vertical profiling of velocity microstructure. *Journal of Physical Oceanography*, 4:107–115, 1974.
- T. Osborn and C. Crawford. An airfoil probe for measuring turbulent velocity fluctuations in water. In *Dobson F., Hasse L., Davis R. (eds) Air-Sea Interaction*. Springer, Boston, MA, 1980.
- M. Palodichuk, B. Polagye, and J. Thomson. Resource mapping at tidal energy sites. *IEEE Journal of Oceanic Engineering*, 38(3):433–446, July 2013.
- A. Patterson. Turbulence spectrum studies in the sea with hot wires. *Limnology and Oceanography*, 3(2):161–180, 1958.
- J. Pedlosky. *Geophysical Fluid Dynamics*. New York: Springer Verlag, 1979.
- E. Perlman, R. Burns, Y. Li, and C. Meneveau. Data exploration of turbulence simulations using a database cluster. In *Proceedings of the 2007 ACM/IEEE Conference on Supercomputing*,, number 1-11, 2007.
- R. Pinkel. A brief review of doppler sonar development at scripps. *Methods in Oceanography*, 17:252–263, 2016.
- S. Pope. *Turbulent Flows*, pages 10–24, 83–96. Cambridge University Press, New York, 2000.
- T. Probert. Orkney tidal power: A hotbed on the seabed. *Power Engineering International*, 19(1):18–22, January 2011.

- Teledyne RDI. *Teledyne RD Instruments Workhorse Sentinel Self Contained 1200m 600, 300 kHz ADCP*. Teledyne RD Instruments, 14020 Stowe Drive, Poway, CA 92064 USA, August 2013.
- O. Reynolds. On the dynamical theory of incompressible viscous fluids and the determination of the criterion. *Proceedings of the Royal Society: Mathematical and Physical Sciences*, 451(1941):5–47, 1895.
- A. Shcherbina, E. D’Asaro, and S. Nylund. Observing fine-scale oceanic velocity structure with an autonomous nortek acoustic doppler current profiler. *Journal of Atmospheric and Oceanic Technology*, 35(2):411–427, 2018.
- H. Sibert, K. Lehmann, and R. A. Shaw. On the use of hot-wire anemometers for turbulence measurements in clouds. *Journal of Atmospheric and Oceanic Technology*, 24(6):980–993, 2006.
- J. Simpson. A free fall probe for the measurement of velocity microstructure. *Deep-Sea Research and Oceanographic Abstracts*, 19(4):331–336, 1972.
- R. H. Stewart. *Introduction to Physical Oceanography*, pages 107–120. Texas A and M University, 2004.
- R. H. Stewart and H. Grant. Early measurements of turbulence in the ocean: motives and techniques. *Journal of Atmospheric and Oceanic Technology*, 16(11):1467–1473, 1999.
- M. Sulaiman, S. Sinnakaudan, and M. Shukor. Near bed turbulence measurements with acoustic doppler velocimeters (adv). *KSCE Journal of Civil Engineering*, 17(6):1551–1528, 2013.
- G. Tabor and M. Baba-Ahmadi. Inlet conditions for large eddy simulations: a review. *Computers and Fluids*, 39(4):553–567, October 2009.

- E. Tahuchi, D. Stammer, and W. Zahel. Inferring deep ocean tidal energy dissipation from the global high-resolution data-assimilative hamtide model. *Journal of Geophysical Research: Oceans*, 119(7):4573–4592, December 2014.
- H. Tennekes and J.L. Lumley. *A First Course in Turbulence*. MIT Press Design Department, Cambridge, Massachusetts, 1972.
- K. Thomson, B. Polagye, V. Durgesh, and M. Richmond. Measurements of turbulence at two tidal energy sites in puget sound, wa. *IEEE Journal of Oceanic Engineering*, 37(3):363–373, July 2012.
- S. Thorpe. *The Turbulent Ocean*. Cambridge University Press, Cambridge, 2005.
- C. Tschegg and E. Hays. Transistorized velocimeter for measuring the speed of sound in the sea. *The journal of the acoustical society of america*, 31(7):1038–1039, 1959.
- R. Urick. *Principles of Underwater Sound*, pages 147–197, 237–287. Peninsular Publishing, 26666 Birch Hill Way Los Altos Hills, California, 3 edition, 1967.
- R. Verstappen and A. Veldman. Direct numerical simulation of turbulence at lower costs. *Journal of Engineering Mathematics*, 32(2):142–159, February 1997.
- G. Voulgaris and J.H. Trowbridge. Evaluation of the acoustic doppler velocimeter (adv) for turbulence measurements. *Journal of Atmospheric and Oceanic Technology*, 15(272-289), 1996.
- R. Walters, M. Tarbotton, and C. Hiles. Estimation of tidal power potential. *Renewable Energy*, 51:255–262, 2013.
- M. Wan, S. Chen, G. Eyink, C. Meneveau, E. Perlam, R. Burns, Y. Li, A. Szalay, P. Johnson, and S. Hamilto. Johns hopkins university databases (jhtdb) forced isotropic turbulence data set (extended), June 2018.

- X. Wang, E. Perlman, Burns R, T. Malik, T. Budava, C. Meneveau, and A. Szalay. Jaws: Job-aware workload scheduling for the exploration of turbulence simulations. In *ACM/IEEE International Conference for High Performance Computing, Networking, Storage and Analysis*, pages 1–11. IEEE, 2010.
- P. Welch. The use of fast fourier transform for the estimation of power spectra: A method based on time averaging over short, modified periodograms. *IEEE Transactions and Audio and Electroacoustics*, 15(2):70–73, June 1967.
- G. Wenz. Acoustic ambient noise in the ocean: Spectra and sources. *The journal of the acoustical society of america*, 34(12):1936–1956, December 1962.
- J. Williams, P Bell, J. Humphery, P. Hardcastle, and P. Thorne. New approach to measurement of sediment processes in a tidal inlet. *Continental Shel Research*, 23(14):1239–1254, 2003.
- K. Wilson. *Turbulence models and synthesis of random fields for acousitc wave propagation calculations*. Army Research Laboratory, July 1998.
- L. Zedel. Evaluation of an acousitc doppler profiler with application to stratified flow in a fjord. Masters thesis, University of Victoria, January 1985.
- L. Zedel. Modeling pulse-to-pulse coherent doppler sonar. *Journal of Atompsheric and Oceanic Technology*, 25(10):1824–1844, Januaryn 2008.
- L. Zedel. Noise in coherent doppler sonar velocity measurements: Where does it come from and what can you do about it? In *2014 Oceans - St John's*, pages 1–5, 2014.
- L. Zedel. Modelling doppler sonar backscatter. In *2015 IEEE/OES Eleventh Current, Waves and Turbulence Measurement (CWTM)*, pages 1–5, March 2015.

D.S Zrnic. Spectral moment estimates from correlated pulse pairs. *IEEE Transactions on Aerospace and Electronic Systems*, 13(4):344–354, July 1977.